technische universität
dortmund

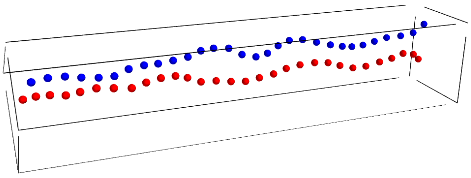

# Hydrodynamic Interactions between Polymers in a Mesoscopic Simulation

Masterarbeit
zur Erlangung des akademischen Grades
Master of Science

vorgelegt von
Jens Winkelmann
geboren in Essen

Lehrstuhl für Theoretische Physik I
Fakultät Physik
Technische Universität Dortmund
2015

1. Gutachter: Prof. Dr. Jan Kierfeld
2. Gutachter: Priv.-Doz. Dr. Ute Löw

Datum des Einreichens der Arbeit: 30.09.2015

“In theory there is no difference between theory and practice; in practice there is.” [1]

*(Albert Einstein)*

---

[1] `https://www.youtube.com/watch?v=ypSJCrr0ONE`

## Abstract

We investigate correlations due to hydrodynamic interaction between two confined polymers in a mesoscopic solvent model. A particle based simulation, called Multiparticle Collision Dynamics (MPCD) is used for the solvent, whereas the polymer is simulated by a simple Molecular Dynamics (MD) simulation. The forces in this MD simulation are based on a worm-like chain model. [1] For the confinement optical traps for every monomer and a channel with a rectangular cross section is used. Invariant energy no-slip boundary conditions are proposed for the polmyer in the channel. The polymers are investigated by cross- and autocorrelating the positions of two opposing monomers. With an optical trap confinement, correlations are visible in the cross-correlation function for different trap strength and fit very well to the theoretical prediction. In an infinite system with finite-size, oscillations in the correlation functions occur due to hydrodynamic self-interaction. The two polymers in the channel do not show correlations in the used correlation function. Thus, experimental results for the same setup cannot be confirmed.

## Zusammenfassung

Untersucht werden Korrelation aufgrund von hydrodynamischer Wechselwirkung zwischen zwei eingeschränkten Polymeren in einer Flüssigkeitssimulation auf mesoskopischer Skala. Das Fluid wird dazu mithilfe der teilchenbasierten Methode, Multiparticle Collision Dynamics (MPCD), simuliert. Für das Polymer, dem das Modell der wurmartige Kette zugrunde liegt, wird eine simple Molekular Dynamik (MD) Simulation verwendet. [1] Das Polymer wird zum einen mithilfe von optischen Fallen festgehalten und zum anderen in einem Kanal mit einer rechteckigen Querschnittsfläche eingesperrt. Energieerhaltende Randbedingungen mit Reibung werden für das Polymer im Kanal vorgestellt. Mit einer Auto- und einer Kross-Korrelationsfunktionen werden dann die Korrelationen für die zwei Aufbauten untersucht. Die Korrelationen zwischen den Polymeren wird beim Festhalten mit den optischen Fallen in der Kross-Korrelation sichtbar. Diese treten bei unterschiedlichen Kraftkonstanten auf und passen gut zu theoretischen Vorhersagen. In einem unendlichen System, das mit periodischen Randbedingungen simuliert wird, kann man Oszillationen aufgrund von hydrodynamischer Selbstwechselwirkung beobachten. Die zwei Polymere im Kanal zeigen dagegen keine Korrelationen in der untersuchten Korrelationsfunktion. Daher können experimentellen Ergebnisse zu dem gleichen Aufbau nicht bestätigt werden.

---

[1] The source code of the used simulation program is available in the supplementary material or online: `https://bitbucket.org/jWinman/masterarbeit`

# Acronyms

**ACF** Autocorrelation Function.

**AT** Anderson Thermostat.

**CCF** Cross-Correlation Function.

**DNA** Deoxyribonucleic Acid.

**DPD** Dissipative Particle Dynamics.

**F-actin** Actin Filaments.

**HI** Hydrodynamic Interaction.

**IENS** Invariant Energy No-Slip.

**LB** Lattice Boltzmann.

**LJ** Lennard–Jones.

**MC** Monte Carlo.

**MCW** Metachronal Wave.

**MD** Molecular Dynamics.

**MPC** Multi Particle Collision.

**ODE** Ordinary Differential Equations.

**PDE** Partial Differential Equation.

**SRD** Stochastic Rotation Dynamics.

**TCF** Tangential Correlation Function.

**VACF** Velocity Autocorrelation Function.

**WLC** Worm-Like Chain.

# Glossary

| **Notation** | **Description** |
|---|---|
| $D$ | Diffusion constant. |
| $K$ | Confinement strength. |
| $L_{\mathrm{C}}$ | Contour length. |
| $L_{\mathrm{P}}$ | Persistence length. |
| $M$ | Mass of a solute particle. |
| $N^m$ | Number of solute particle. |
| $N^s$ | Number of solvent particle. |
| $R_H$ | Hydrodynamic radius. |
| $\alpha$ | Rotation angle. |
| $\langle ... \rangle$ | Ensemble average. |
| $\varepsilon$ | LJ energy. |
| $\eta$ | Viscosity. |
| $\mathfrak{R}$ | Stochastic rotation matrix. |
| $\gamma$ | Strength of hydrodynamic coupling. |
| $\kappa$ | Rigidity. |
| $\lambda$ | Deflection length. |
| $\mathcal{H}$ | Hamiltonian. |
| $\lceil ... \rceil$ | Ceiling function. |
| $\lfloor ... \rfloor$ | Floor function. |
| $\Delta h$ | Penetration time step for the MPC simulation. |
| $\Delta h_{\mathrm{MD}}$ | Penetration time step for the MD simulation. |
| $\sigma$ | LJ length. |
| $\tau$ | Relaxation time. |
| $\boldsymbol{H}$ | Oseen tensor. |
| $\boldsymbol{b}$ | Bond vector. |
| $\boldsymbol{r}$ | Position. |
| $\boldsymbol{t}$ | Tangential vector. |
| $\boldsymbol{v}$ | Velocity. |
| $\xi$ | Friction coefficient. |
| $a$ | Cell size. |
| $h$ | Time step for the MPC simulation. |
| $h_{\mathrm{MD}}$ | Time step for the MD simulation. |
| $k_p$ | Spring constant between monomers. |
| $k_{\mathrm{B}}T$ | Thermal energy. |
| $l$ | Spring rest length between monomers. |
| $m$ | Mass of a solvent particle. |
| $p$ | Pressure. |

# Contents

# 1 Introduction

## 1.1 Hydrodynamics

Interactions in colloidal suspensions, sychronization of flagella motion, synchronizing collective behavior of micro swimmer, and Zimm dynamics of polymers show that Hydrodynamic Interactions (HIs) play a major role in different contexts of biophysics and soft matter physics. Despite its complexity, HI between two macroscopic particles in a solvent is well understood but the interactions become complicated when looking at many-particle systems, such as polymers. The hydrodynamic force acting on two point particles was already calculated in the limit of low Reynolds numbers around ninety years ago [37]. Superimposing this complex two-particle interaction makes it difficult to predict the behavior of a many-particle system. Thus, it remains not well investigated.

This thesis takes a closer look at the dynamic properties of semiflexible polymers solved in a liquid at equilibrium. Due to HI the dynamics of the polymer become more complex and new phenomena occur that cannot be described by non-hydrodynamic models. For one polymer, this dynamics can be described within the Zimm model, which extends the Rouse model to HI. Within this model, one monomer can notices the flow field that is caused by the movement of another monomer. The same holds true for a system of two polymers, but the overall interactions between both polymers and the effects on the dynamics remain unclear. This thesis tries to spot some light on these questions.

In the well-understood, two point particles system, the random Brownian movement of one particle creates a flow field in the liquid, that affects the movement of the other particle. On a microscopic level, the particle executing random Brownian motion transfers momentum to the fluid and leaves a gap behind it, which is filled by fluid particles. This flow disturbance is then carried throughout the fluid and reaches the other particle, that experiences this momentum change as a force. This way information of one particle's movement is carried through a field to the other particle and correlations can be seen.

More abstractly, the velocity $\boldsymbol{v}_k$ of one particle $k$ is influenced by the force field $\boldsymbol{f}_l$ of the other particle $l$. Extended to an $N^m$ system of solute point particle, it can be written as

$$\boldsymbol{v}_k = \sum_{l \neq k}^{N^m} \boldsymbol{H}(\boldsymbol{R}_{lk}) \boldsymbol{f}_l \quad \text{with} \quad \boldsymbol{H}(\boldsymbol{R}_{lk}) = \frac{1}{8\pi\eta R_{lk}} \left( \mathbb{1} + \frac{\boldsymbol{R}_{lk} \otimes \boldsymbol{R}_{lk}}{R_{lk}^2} \right), \tag{1.1}$$

where $\boldsymbol{H}(\boldsymbol{R}_{kl})$ is the Oseen tensor that depends on the distance $\boldsymbol{R}_{kl}$ between the two particles. The Oseen tensor is the Green's function of the Stokes equation

$$\frac{1}{\rho}\nabla p - \frac{\eta}{\rho}\nabla^2 \boldsymbol{v} = \boldsymbol{f}_{\text{ext}}, \tag{1.2}$$

which is the overdamped limit of the Navier–Stokes equation. It describes formally the coupling of the two particles. Thus HI are long-ranged since the Oseen tensor decays with $^1/_{R_{lk}}$.

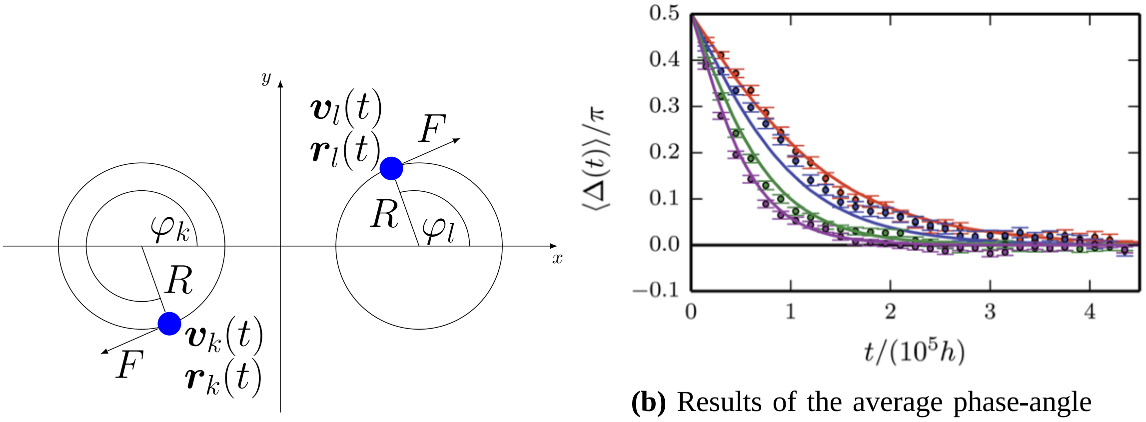

**(a)** Two particles with position $\boldsymbol{r}$ and velocity $\boldsymbol{v}$ are propelled on a circular trajectory with a constant force $F$. The two particles are just coupled by HI since they are in the same solvent.

**(b)** Results of the average phase-angle difference $\Delta(t) = \varphi_k(t) - \varphi_l(t)$ for different Péclet numbers $Pe = 120, 140, 160$ and $180$ (top to bottom). The $Pe$ describes the ratio of advection to diffusion. The symbols represent simulation results and the solid lines analytical calculations [39].

**Figure 1.1:** Investigation of hydrodynamic interactions (HI) in an active two-particle system. The particles move independently in a fluid on a circular trajectory and are just coupled by HI (figure 1.1(a)). For all $Pe$ one can see a sychronization of the two phase-angles since the average phase-angle difference $\langle\Delta(t)\rangle$ vanishes (figure 1.1(b)).

Many investigations concerning the consequences of HI for biological and soft matter physic systems were done in the recent years [11, 24, 35, 39]. Most of them are active systems where synchronization play a crucial role. I.e., in [39] the synchronization of two propelled particles due to HI were investigated in a computer simulation. These two particles, $k$ and $l$, as depicted in figure 1.1(a) are both propelled with a constant force $F$ tangential to the circle. They move along a fixed circular trajectory with a certain angular velocity $\dot{\varphi}_k$ and $\dot{\varphi}_l$, respectively. Since they both rotate independently, they just interact via HI. Nevertheless, a synchronization of the two phase-angles $\varphi_k$ and $\varphi_l$ was observed as seen in figure 1.1(b). This effect plays a major role in similar, but more complicated, active systems in biophysics such as the flagella motion of *E.coli* or the beating of cilia on swimming cells such as *paramecium*. For those systems similar effects were observed [11, 24, 35].

**Figure 1.2:** A paramecium cell that is completely covered with short cilia. These are hair-like organelles on the surface of the cell. The cell is propelled by the beating of the cilia which are synchronized due to hydrodynamic interactions (HI) [28].

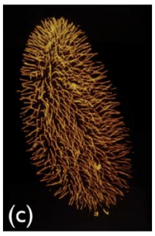

The surface of the paramecium cell (fig. 1.2) is completely covered with short cilia. Cilia are hair-like organelles that the cell uses in order to swim through the fluid. Each cilium is an independent part of the cell and the beating is therefore asynchronously. This would certainly not lead to a propelled motion because the total momentum transfers onto the cell

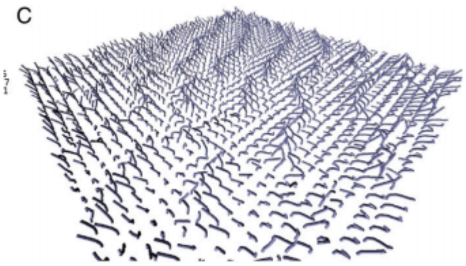

**Figure 1.3:** Snapshot from a simulation of an array of cilia on a plane surface. Every cilium is propelled independently. So the beating period are asynchronous at the beginning. Due to HI they start to synchronize and form metachronal waves (MCWs) throughout the array [11].

by the beating would cancel out. Moreover, a completely synchronized movement of the cilia would not lead to a swimming organism due to the Purcell's scallop theorem [34]. This states that the motion at low Reynolds numbers has to be invariant under time-reversal in order to propel the organism. Therefore a motion of the different beats that is neither random nor completely synchronous, is needed.

J. Elgeti and G. Gompper showed that the cilia synchronize only by HI in form of a Metachronal Wave (MCW) [11]. In this large-scale computer simulation a 2D cilia array in a 3D fluid medium was investigated. The snapshot in 1.3 already reveals those waves and therefore the correct synchronization throughout the array for a propulsion. While every cilium is beating in a reciprocal, but circular motion, the MCWs move only in one direction over the surface. This causes a transport of the fluid above the array, which ultimately leads to a propulsion. Since this simulation consists of only two different components, independent cilia and the fluid, it is convincing that HI was sufficient for the emergence of MCWs.

Recent experiments at the University of Basel [38] claimed to observe similar synchronization in polymer physics due to HI. Snapshots from the experiments, published in a master thesis, can be seen in figure 1.4 [38]. The experiments were done with microfluidic devices where the polymers were confined in a quasi-two dimensional narrow channel. Therefore, the height of the channel ($z = 0.5\,\mu\mathrm{m}$) was a lot smaller than the width of the channel ($d = 2$-$4\,\mu\mathrm{m}$).

With this setup, the experimenters claimed to observe several phenomena that they deduced to be caused by HI. For two interacting polymers a reduced translational diffusion, entanglement and correlated oscillating motion and were measured. It was argued that the two polymers in the channel get entangled due to HI and then start to diffuse as one. But it is unknown if all other interactions such as van-der-Waals or Coulomb interactions were turned off to a reasonable amount. During the time of entanglement, the autocorrelation function of the distance perpendicular to the channel direction was measured. This revealed a synchronous oscillating behavior of both polymers.

These experimental results lead to the fundamental motivation for this thesis. While the true nature of those phenomena remains unclear, a mesoscopic, hydrodynamic computer simulation of such systems can shed more light on this issue. Since particle interactions such as van-der-Waals, Coulomb, or also hydrodynamic interactions, can be turned on and off very easily, a reproduction of those phenomena is attempted throughout this thesis. By creating the same setup in the simulation, similar results should be gained. Otherwise HI can be excluded as a cause.

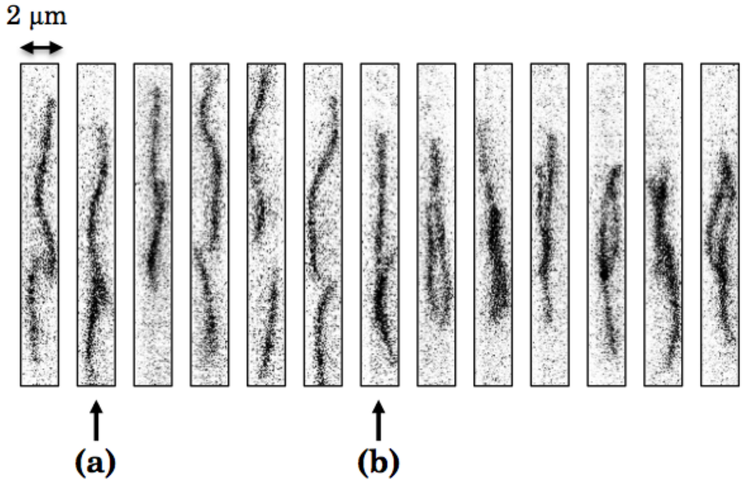

**Figure 1.4:** In the experiment at the University of Basel, the dynamics of two polymers were observed. While at position (a) the polymers slightly overlap, but are still separated, the polymers entangle at position (b). From then on, they synchronize and diffuse together for a prolonged period of time. The cause was claimed, but not proven to be hydrodynamic interactions (HIs) [38].

## 1.2 Semiflexible Polymers

Polymers are thin stringlike molecules with diameters $L_d$ on the nanometer scale. They consist of repeating atoms or molecules that are denoted as monomers. A certain number of monomers make up a polymer.

Today, polymers play a major role in industry and daily life. Plastic materials such as rubbers, silicone, styrofoam, polyester or carbon nanotubes and biological materials such as proteins, Deoxyribonucleic Acid (DNA) or microtubules are just some examples of synthetic and biopolymers. Some of the examples are listed in figure 1.5.

They occur in different forms, i.e. rings, coils, or branches, however, this thesis will focus on simple polymers that are just filamentous. Filamentous polymers can be seen as molecules that are made up of small rods, so-called bonds. They can further be classified by their rigidity and persistence length $L_\mathrm{P}$, respectively. Both quantities describe the stiffness of the polymer. For a polymer the persistence length quantifies the rigidity of the polymer given a thermal energy of $1\,k_\mathrm{B}T$ where $k_\mathrm{B}$ is the Boltzmann constant and $T$ room temperature.

The polymers with a small persistence length can bend easily and are therefore called flexible polymers. Their persistence length is smaller than the length of one bond, so that they can easily form coils. On the other hand, polymers that can hardly be bent are referred to stiff polymers. The topic of investigation in this thesis will be semiflexible polymers. Their persistence length is of the order of their contour length. Hence, they act like flexible rods and are slightly bendable.

In the experiments [38], Actin Filaments (F-actin) with a typical contour length of $20$-$50\,\mu\mathrm{m}$ were used. Since the persistence length is $17\,\mu\mathrm{m}$, they can be considered as semiflexible polymers. F-actin is a component of the cell cytoskeleton where they are involved in transport processes. They especially play a major role in muscle contraction. The cyclical in-

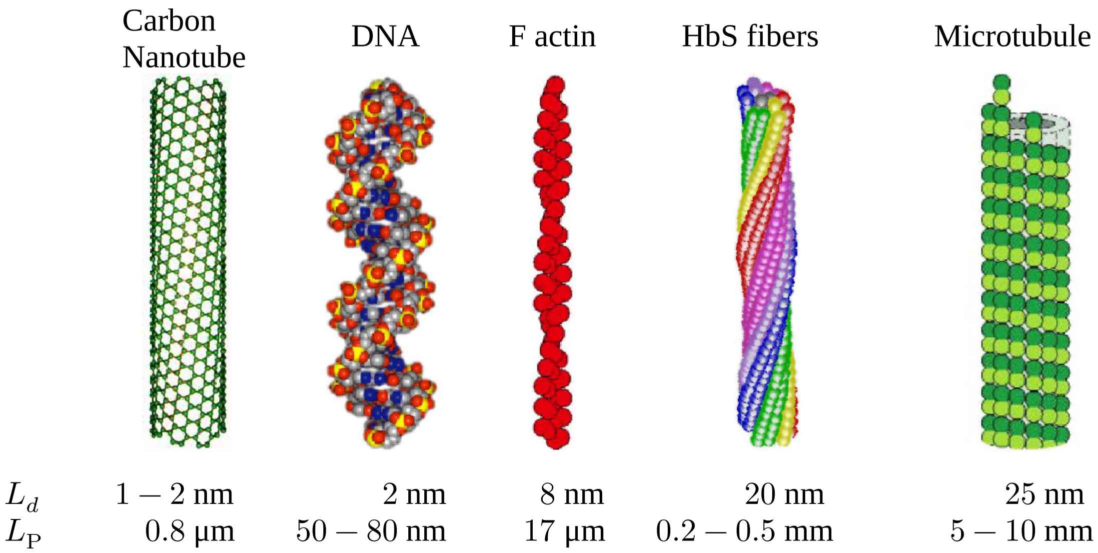

**Figure 1.5:** Examples of various polymers with typical diameters $L_d$ and persistence lengths $L_\mathrm{P}$ [22, translated]. In the mentioned experiments F-Actin was used [38].

teraction between myosin is often organized in filaments, of which the major component is F-actin [18].

The structure of F-actin has been determined by electron microscopy [10]. It is helical with 13 actin molecules per 6 left-handed turns and a repeat of about $360$ Å. As the rotation per molecule is $166°$, the actin helix morphologically appears as two right-handed steep helices which twine slowly around each other [18].

F-actin is a polar polymer with two dynamically different ends, the so-called barbed and pointed ends. Since the filament grows faster at the barbed end than it decreases at the other end, the polymer can quickly elongate to cell size length [38]. Thus, they represent a typical semiflexible polymer and are suitable for experimental investigations concerning HI.

## 1.3 Mesoscopic Simulations

In order to investigate the behavior of F-actin in a liquid solution, a mesoscopic simulation technique called Multi Particle Collision (MPC) Dynamics was chosen for the solvent. It is an off-lattice, point-particle based method with coarse graining the described fluid and therefore solves the Navier–Stokes equation. So one MPC particle does not describe the dynamics of one atom or molecule in the fluid. Instead one MPC particle corresponds to a group of fluid atoms or molecules which means that the degrees of freedom of the fluid are reduced and particle interaction is done by a phenomenological rule which cannot necessarily be traced from a microscopic theory. In that way MPC can simulate the temporal development of the liquid much faster than microscopic methods because it does not simulate the fluid in all details. But since it still describes the thermodynamic and hydrodynamic properties of a liquid it is ideal for investigating fluctuations of polymers.

In figure 1.6(a) the time and length scale of different simulation methods is shown. All these methods have in common that they solve the Navier–Stokes equation for the fluid dynamics numerically. They just differ by the method of solving it and the scale, on which they

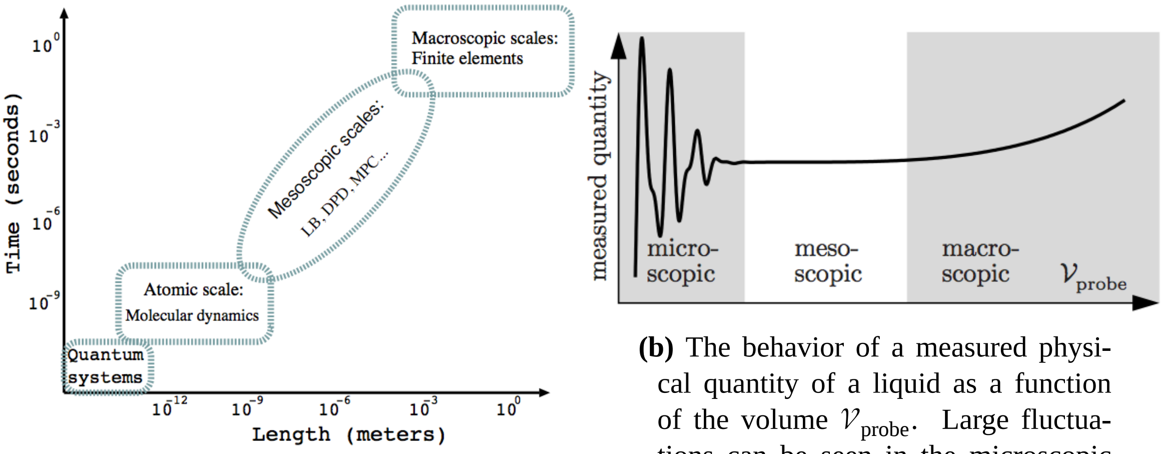

**(a)** The time and length scale of different simulation methods. The length and time scale for mesoscopic simulation techniques vary from $10^{-3}\,\mathrm{s}$ to $10^{-6}\,\mathrm{s}$ and from $10^{-8}\,\mathrm{m}$ to $10^{-3}\,\mathrm{m}$, respectively [8].

**(b)** The behavior of a measured physical quantity of a liquid as a function of the volume $\mathcal{V}_{\text{probe}}$. Large fluctuations can be seen in the microscopic probes, while the observed quantity shows a well-defined behavior in the mesoscopic. For the macroscopic scale the fluid shows small variations due to external forces. [6]

**Figure 1.6:** Simulation techniques and physical quantities on different scales.

solve it. Besides MPC, there exist many other simulation methods on the mesoscopic scale, such as Lattice Boltzmann (LB) or Dissipative Particle Dynamics (DPD). While LB is a lattice based method, where the fluid moves on a lattice, DPD is also a particle based method in the canonical ensemble. There dissipative, random and conservative forces between the particles are used. They all operate in-between the microscopic and the macroscopic scale and this way gain the advantages of both regimes.

While macroscopic methods like finite elements are fast, they do not contain much detailed information like thermodynamic fluctuations. Mesoscopic methods, however, can also capture thermodynamic fluctuations besides being rather fast. On the other side of the scale, molecular dynamics describe the fluid in all detail but the time scale of $10^{-9}\,\mathrm{s}$ makes it difficult to compare simulation results with experiments. Since we are not interested in all the details on the atomic level of the fluid, it is not necessary to go beyond the length scale of mesoscopic scales and comparing simulation results is difficult but still possible. As pictured in figure 1.6(b) the microscopic scale shows all the thermodynamic fluctuations of a physical quantity. In the mesoscopic regime these fluctuations are reduced to a minimum, so that a well-defined value of the measured quantity can be observed. Response of a measured quantity to an external force, however, are best observed in the macroscopic scale, since the observable does not contain much noise due to thermal fluctuations.

The first MPC simulation was published by Malevanets and Kapral in 1999 [29]. Since then it developed quickly into a popular simulation method for investigating complex systems in the field of soft matter because of its simplicity and short run time compared to other methods. Important development for this method was done by Gompper et al. in Jülich over the last decade. Their research is reviewed in [8, 12, 14, 17]. Fundamental information for chapter 2.1.1 are taken from these reviews and will not be cited explicitly, if information are redundant mentioned in several reviews.

I.e. they proposed several cell-level canonical thermostats for the MPC algorithm [8, 12, 14, 15, 17, 19], which are based on rescaling the velocities of the fluid particles and they successfully applied this method to problems in the field of soft matter and biophysics. The one from [15] will be described in chapter 2.1.3, since it was used in this project.

MPC is well suited for biophysical problems because in this field a simple, macroscopic continuum description of the liquid is often not sufficient and more detailed information of the system are wished. On the other hand solving biophysical problems in full detail with microscopic simulations would require a lot of computational power and resource which is not accessible for the majority of researchers. Additionally, biological systems are often driven out of equilibrium by varying local forces, so that it would be difficult to see the systems' response on the microscale. Hence, simulating an actin filament in a liquid on the atomic level would take a tremendous amount of time even with the most powerful computers (2015). On the macroscopic level, one cannot distinguish between the solved polymer and the solvent. Investigations like they were done in this project would not be possible. The closing of the gap between microscopic and macroscopic scale which was done by simulation methods such as MPC was a crucial step for the research field of soft matter.

**How to read this thesis:** After this short introduction we will briefly explain the two used simulation methods, MPC and the coarsed grained Molecular Dynamics (MD), in the second chapter. First, we will explain the algorithm of MPC and its thermodynamic and hydrodynamic properties. Through this we will conclude why this method is capable of simulating fluid dynamics. Since boundary conditions are needed for this project, the implementation of no-slip boundary conditions is described as well as a used thermostat. After introducing the natural units of MPC which are useful for the measured quantities, we will show comparisons between analytic results from the Navier–Stokes equation and the numeric results from the simulation for different geometries. In the second section of this chapter the MD simulation for the polymer is outlined. Here we will explain the potentials and the corresponding force fields that describe the interaction between the single monomers in an unconfined polymer. We will give a brief physical interpretation of the used potential and explain why they are useful to model polymers. For the confinement of the polymer, an implementation to model energy conserving no-slip boundary conditions is proposed. These were first successfully tested on a simple two dimensional MD simulation before using them on the polymer.

The third chapter will depict the results accomplished by this master thesis. We will focus on the tangential correlation function of the polymer, first without and later in a rectangular confinement. The results of the tangential correlation will then be compared to established results of Monte Carlo simulations. There the polymer is simulated without taking HI into account.

The HI between two polymers is investigated for three different system. After introducing the later used correlation functions, HI is first studied at a well known two monomers system. The two monomers are fixed with optical traps of different trap strength and examined for correlations. The different results are compared to experiments and analytic calculations. The system is then extended to two polymers where every monomer is trapped. Lastly, the experiment from [38] with two polymers confined in a rectangular channel is reproduced. The given results will be reflected and discussed in the last chapter.

# 2 Simulation Models

## 2.1 The Fluid Model: Mesoscopic Hydrodynamics

### 2.1.1 MPCD: Multi Particle Collision Dynamics

For the fluid model the mesoscopic hydrodynamic simulation method MPC is used. As already mentioned in the introduction this particle-based method solves the Navier–Stokes equation for fluids within an acceptable accuracy. MPC can easily be implemented. No other software knowledge than that of a programming language like `C++` is needed. Also parallel programming with `OpenMP` [7] directives can be used, in order to parallelize all iterations over all $N$ particles since all operations on the particles are independent of each other. This, for example, is not the case in a DPD simulation where particles interact via forces, which are dependent on the position and velocity of all fluid particles. Here the calculation of the forces would take a crucial amount of run time because the calculation scales with $N^2$ and cannot be easily parallelized. This problem does not occur in MPC because the unmodified algorithm consists of only two individual steps, the streaming and collision step. While the streaming step moves each particle forward, for the collision step the space is divided into cubic cells with cell length $a$. Then, all particles in one cell interact via a stochastic, momentum conserving step. In both steps the chronological order of operation on the particles does not affect the dynamics of the fluid. Thus, parallelization can be used.

**The Streaming Step:** In the streaming step the position $\boldsymbol{r}_i$ of particle $i$ is updated according to

$$\boldsymbol{r}_i(t+h) = \boldsymbol{r}_i(t) + h\boldsymbol{v}_i(t) + h^2\frac{\boldsymbol{F}_{\text{ext}}}{m_i}\,, \tag{2.1}$$

where $\boldsymbol{v}_i$ is the velocity and $m_i$ the mass. The mass of the particle differs whether it is a solvent ($m_i = m$) or solute particle ($m_i = M$). In absence of an external force $\boldsymbol{F}_{\text{ext}}$, the particles are moved ballistically for the time $h$ which will be referred to as the collision time.

As the gentle reader can already recognize, the Galilei invariance [1] is broken if the collision time is not large enough. Then the majority of the particles does not move out of their cells and interact mostly with particles from the same cell. Thus, particles in the same cell become correlated and the collision step acts like a periodic pseudo-potential that keeps particles in one cell together. This is the case if the mean free path $\langle x\rangle$ of the particles is smaller than the grid constant $a$

$$\langle x\rangle = h\sqrt{\frac{k_{\text{B}}T}{m}} < a\,. \tag{2.2}$$

---

[1] The translational symmetry that particles move homogeneously through the system.

The mean free path that depends on the temperatur $T$, the collision time $h$ and the solvent particle mass $m$ describes how far all particles are moved forward on average in an equilibrium state. In order to restore Galilei invariance the grid is shifted by a random vector in the interval $[-a/2, a/2)^d$ with the spatial dimension $d$ before every collision step. Equivalent to shifting the grid, but simpler to implement, is shifting the particles by the random vector with respect to periodic boundary conditions and keeping the grid constant.

**The Collision Step: Stochastic Rotation Dynamics** For the collision step a method called Stochastic Rotation Dynamics (SRD) is used. In this coarse-grained algorithm the relative velocities $\delta \boldsymbol{v}_i$ with respect to the center of mass velocity $v_{c,\mathrm{cm}}$ in one cell $c$ are rotated around a stochastically orientated axis around a fixed angle $\alpha$. The rotation can be mathematically expressed by a matrix $\mathfrak{R}_c(\alpha)$. So the collision step with SRD states

$$\boldsymbol{v}_i(t+h) = \boldsymbol{v}_{c,\mathrm{cm}}(t) + \underbrace{(\mathcal{D}_c(\alpha) - \mathbb{1})}_{\mathfrak{R}_c} \underbrace{(\boldsymbol{v}_i(t) - \boldsymbol{v}_{c,\mathrm{cm}}(t))}_{\delta \boldsymbol{v}_i} . \tag{2.3}$$

The used $3 \times 3$ matrix $\mathcal{D}_c(\alpha)$ can be looked up in the Appendix. It depends on two random numbers which determine the rotation axis around which the velocities are rotated by the angle $\alpha$.

The center of mass velocity $\boldsymbol{v}_{c,\mathrm{cm}}$ can be calculated by averaging over all particle velocities in the cell. By taking into account couplings with embedded solute particles, the center of mass velocities read

$$\boldsymbol{v}_{c,\mathrm{cm}}(t) = \frac{\sum_{i=1}^{N_c^s} m\boldsymbol{v}_i(t) + \sum_{k=1}^{N_c^m} M\boldsymbol{v}_k(t)}{mN_c^s + MN_c^m} . \tag{2.4}$$

First, all momenta of the solvent particles $N_c^s$ and solute particles $N_c^m$ in the cell are added and then divided by the total mass of all particles.

A further noteworthy collision step is the Anderson Thermostat (AT) [1]. Instead of rotating relative velocities, random numbers drawn from a Gaussian distribution are assigned to the relative velocities. This collision step does also successfully model fluid dynamics and additionally thermalizes the fluid. But because of performance reasons, MPC-SRD is preferred.

For simulating fluids and therefore solving the Navier–Stokes equation it is crucial for a simulation method to conserve momentum locally. Since the Navier–Stokes equation is a balance equation where Newton's second law is applied to fluid dynamics, it can be indirectly solved by any stochastic method that conserves local momentum. In more detail, the Navier–Stokes equation can be rewritten as

$$\frac{\partial \rho v_l}{\partial t} = -\frac{\partial \Pi_{kl}}{\partial x_k} \tag{2.5}$$

where $\Pi_{kl}$ is the momentum flux density tensor and $\rho$ the density [27]. This form of the Navier–Stokes equation shows that the fluid is completely described by the momentum via the momentum flux density tensor. Thus momentum conservation ensures the convergence against the analytic solution. However, the order of convergence to the analytic solution may differ from method to method. Unfortunately there is no a-priori convergence estimation for

SRD. Good agreements with analytic solutions are therefore shown in the next section for simple geometries where comparisons with analytic solutions can be done.

In order to prove local momentum conservation one has to look at the total momentum $\boldsymbol{P}$ before and after the collision step:

$$\boldsymbol{P}(t+h) = \sum_{i=1}^{N} m_i \boldsymbol{v}_i(t+h) = \sum_c \sum_{j\in c}^{N_c} m_j \boldsymbol{v}_j(t+h) \tag{2.6}$$

$$= \sum_c \sum_{j\in c}^{N_c} \big( m_j \boldsymbol{v}_{c,\mathrm{cm}}(t) + \mathfrak{R}_c(\alpha) m_j \delta\boldsymbol{v}_j(t) \big) \tag{2.7}$$

$$= \sum_c M_c \boldsymbol{v}_{c,\mathrm{cm}}(t) + \sum_c \mathfrak{R}_c(\alpha) \underbrace{\sum_{j\in c}^{N_c} m_j \delta\boldsymbol{v}_j(t)}_{=0} \tag{2.8}$$

$$= \sum_c M_c \boldsymbol{v}_{c,\mathrm{cm}}(t) \tag{2.9}$$

$$= \boldsymbol{P}(t)\ . \tag{2.10}$$

After rewriting the summation over all particles into the summation over all cells $c$ and particles in each cell, the collision step is inserted. Since the average over the deviation from the mean $\delta\boldsymbol{v}_j(t)$ vanishes per definition, the last sum in (2.8) is zero. Therefore, the local momentum in cell $c$ is its center of mass momentum independently from the rotation matrix. The local momentum is conserved. Since local momentum conservation also implies total momentum conservation, the momentum $\boldsymbol{P}(t+h)$ does not change, either.

Furthermore the SRD algorithm also conserves energy locally. This can be shown analogously to the momentum conservation.

$$E(t+h) = \frac{1}{2}\sum_{i=1}^{N} m_i \boldsymbol{v}_i^2(t+h) = \frac{1}{2}\sum_c \sum_{j\in c}^{N_c} m_j \boldsymbol{v}_j^2(t+h) \tag{2.11}$$

$$= \frac{1}{2}\sum_c \sum_{j\in c}^{N_c} m_j \big( \boldsymbol{v}_{c,\mathrm{cm}}(t) + \mathfrak{R}_c(\alpha)\delta\boldsymbol{v}_j(t) \big)^2 \tag{2.12}$$

$$= \frac{1}{2}\sum_c \left( M_c \boldsymbol{v}_{c,\mathrm{cm}}^2(t) + \mathfrak{R}_c(\alpha)\boldsymbol{v}_{c,\mathrm{cm}} \underbrace{\sum_{j\in c}^{N_c} m_j \delta\boldsymbol{v}_j(t)}_{=0} + \underbrace{\sum_{j\in c}^{N_c} \delta\boldsymbol{v}_j^2(t)}_{=0} \right) \tag{2.13}$$

$$= \frac{1}{2}\sum_c M_c \boldsymbol{v}_{c,\mathrm{cm}}^2(t) \tag{2.14}$$

$$= E(t)\ . \tag{2.15}$$

Here in (2.13) the orthogonality of $\mathfrak{R}_c$ is used. The summation over the relative velocities $\delta\boldsymbol{v}_j(t)$ vanishes again and it can be shown that the squares are also zero in our simulation

$$\sum_{j\in c}^{N_c} \delta\boldsymbol{v}_j^2(t) = \sum_{j\in c}^{N_c} \big( \boldsymbol{v}_j(t) - \boldsymbol{v}_{c,\mathrm{cm}}(t) \big)^2 \tag{2.16}$$

$$= \sum_{j\in c}^{N_c} \boldsymbol{v}_j^2(t) + N_c \boldsymbol{v}_{c,\mathrm{cm}}^2(t) - 2N_c \boldsymbol{v}_{c,\mathrm{cm}}^2(t) \tag{2.17}$$

$$= \sum_{j\in c}^{N_c} \boldsymbol{v}_j^2(t) - \sum_{j\in c}^{N_c} \boldsymbol{v}_j^2(t) - 2\underbrace{\sum_{i<j}^{N_c} \boldsymbol{v}_i(t)\boldsymbol{v}_j(t)}_{=0} \tag{2.18}$$

$$= 0\,. \tag{2.19}$$

The last summation in (2.18) can be identified with a sum over an autocorrelation function without lag zero between the velocities of particles in one cell.[2] Since correlations are turned off by the grid shifting, this sum can be assumed to be zero and energy conservation is proven under the condition of uncorrelated velocities in one cell. This is in good agreement with the picture of the pseudo-potentials created by the cells. When not performing the grid shifting, pseudo-potentials that keep the particles in one cell can be seen and energy is not conserved.

### 2.1.2 No-Slip Boundary Conditions

Because confined geometries will be simulated, boundary conditions for the fluid and the polymer play an important role. These boundary conditions, explained in this section, are taken from [14, pp. 420]. They describe the interaction with the walls for fluid particles. The interaction of the polymer and the walls will be explained in 2.2.2.

In order to simulate no-slip boundaries, the tangential and perpendicular velocity components to the wall have to vanish, respectively. Generally, this can be achieved for the fluid particles by inverting the velocity of the penetrating particle. In the case of constant external fields such as gravity the force during the penetration time and the time it is put back into the box has to be undone. For the position the streaming step of the particle is performed with the time $-2\Delta h_i$. Hence, positions and velocities at the walls are updated according to

$$\tilde{\boldsymbol{v}}_i(t+h) = -\boldsymbol{v}_i(t+h) + 2\Delta h_i \frac{\boldsymbol{F}_{\text{ext}}}{m} \tag{2.20}$$

$$\tilde{\boldsymbol{r}}_i(t+h) = \boldsymbol{r}(t+h) - 2\boldsymbol{v}_i(t+h)\Delta h_i + 2\Delta h_i^2 \frac{\boldsymbol{F}_{\text{ext}}}{m}\,. \tag{2.21}$$

Here, $\Delta h_i = \left. r_{ik}(t+h) - L_k\theta(r_{ik}-L_k) \middle/ v_{ik}(t+h) \right.$, where $\theta(x)$ is the Heaviside function, describes the penetration time, if $\boldsymbol{F}_{\text{ext}}$ is parallel to the wall.

When doing the grid shifting, the walls do not coincide with the grid and these boundary conditions do not simulate the no-slip correctly due to underpopulation in the boundary cells. This can be corrected by implementing so-called ghost particles. These ghost particles fill up underpopulated boundary cells to the mean number of particles per cell $\langle N_c \rangle$ with non-existing particles that only participate with their velocity in the collision step. The velocities are drawn from a Maxwell–Boltzmann distribution. Since the sum over numbers from a Gaussian distribution is again such a number, the total momentum $\boldsymbol{p}$ of all ghost particles can be added during the calculation of the center of mass velocity. The total momentum $\boldsymbol{p}$ then has the mean zero and variance $\sigma^2$ and the center of mass calculation is changed to

$$\boldsymbol{v}_{c,\text{cm}} = \frac{\boldsymbol{p} + \sum_{i=1}^{N_c^s} m\boldsymbol{v}_i(t) + \sum_{k=1}^{N_c^m} M\boldsymbol{v}_k(t)}{m\langle N_c^s \rangle + M N_c^m}, \quad \sigma^2 = (m\langle N_c^s \rangle - N_c^s) k_{\text{B}} T\,. \tag{2.22}$$

### 2.1.3 Global Thermostat

In order to keep the temperature constant throughout the fluid, a thermostat is used. This way unpleasant local temperature gradients that can occur near solute particles due to vis-

---

[2] A detailed explanation to autocorrelation functions can be seen in 3.2.1.

cous heating are suppressed. There are many ways to implement a thermostat in an MPC simulation, for example the MPC-AT already comes with a particle-level thermostat. This, however, is slower than the SRD algorithm. Thus it is more efficient to implement a separate, cell-level thermostat that rescales all velocities in one cell with a factor $\kappa_c$ to the required temperature $T_0$. The SRD collision step is changed to

$$\boldsymbol{v}_i(t+h) = \boldsymbol{v}_{c,\mathrm{cm}}(t) + \kappa_c \mathfrak{R}_c\big(\boldsymbol{v}_i(t) - \boldsymbol{v}_{c,\mathrm{cm}}(t)\big)\,. \tag{2.23}$$

In [19] several cell-level thermostats are tested. Besides driving the system to the required temperature, a good thermostat should not destroy the Maxwell–Boltzmann velocity distribution and not change macroscopic properties, such as the viscosity or diffusion of the fluid. While a simple isokinetic thermostat [12] does not fulfill the first requirement, the following thermostat does not violate either requirement.

The following thermostat was first suggested by Heyes in a molecular dynamic simulation [2] and then transferred to MPC simulations [15, 17]. While Heyes' thermostat still violated detailed balance, the MPC thermostat was adjusted to that effect. The algorithm calculating $\kappa_c$ consists of four steps and is carried out independently in every collision cell:

a. Select a random number $\psi \in [1, 1+\varepsilon]$ where $\varepsilon$ is chosen to be in $[0.05, 0.3]$.

b. If another random number $\gamma \in \{-1, 1\}$ equals $-1$, then the scaling factor is set to $\kappa_c = \psi$, else $\kappa_c = {}^1\!/\!_\psi$.

c. A third random number $\xi \in [0,1]$ determines the acceptance rate of the scalar factor. If $\xi < p_A = \min(1, A)$, where

$$A = \kappa_c^{d(N_c-1)} \exp\left(-(\kappa_c^2 - 1)\frac{E_{\mathrm{kin}}}{k_{\mathrm{B}}T_0}\right) \quad \text{with} \tag{2.24}$$

$$E_{\mathrm{kin}} = \frac{1}{2}\sum_{i=1}^{N_c} m_i\big(\boldsymbol{v}_i - \boldsymbol{v}_{c,\mathrm{cm}}\big)^2\,, \tag{2.25}$$

then $\kappa_c$ is accepted as scaling factor. The prefactor $\kappa_c^{d(N_c-1)}$ with the spatial dimension $d$ takes the phase-space volume change during the rescaling into account.

d. If the attempt is accepted, then the collision step is changed to (2.23), else no velocity rescaling is done in the collision step.

The thermostat has one free parameter $\varepsilon$ that determines how fast the system relaxes to the temperature $T_0$. For all further simulations this parameter is set to $0.2$ where the thermostat seems to work best. It has already been successfully applied to simulations of sedimenting charged colloids [15].

### 2.1.4 Natural Units of MPCD

Since the dynamics of the fluid can be described within classical mechanics, three basic units are needed. All other physical quantities can be expressed by these three units. For reasons of simplicity we choose mass, length and energy scale as the basic physical quantities because within these scales, constants throughout all simulations can be found. So all masses will be expressed by the mass of one MPC particle $m = 1$, all length scales by the cell size $a = 1$ and all energies by $k_\mathrm{B}T = 1$.

A crucial quantity for investigating the dynamics of a system is the time scale $t$. It can be deduced by the equipartition theorem

$$\frac{1}{2}m\langle \boldsymbol{v}^2\rangle = \frac{3}{2}k_\mathrm{B}T\,, \tag{2.26}$$

which states that the averaged kinetic energy per particle equals $1/2k_\mathrm{B}T$ per degree of freedom. By introducing a dimensionless velocity $\boldsymbol{v} = a/t\tilde{\boldsymbol{v}}$ one gets

$$\frac{1}{2}\langle \tilde{\boldsymbol{v}}^2\rangle = \frac{3}{2}\underbrace{\frac{t^2k_\mathrm{B}T}{ma^2}}_{=1}\,. \tag{2.27}$$

In order to keep this equation dimensionless the last factor has to equal one. Thus, the time scales with $t = \sqrt{ma^2/k_\mathrm{B}T}$. An overview over relevant parameters that are used for all simulations and reflect a fluid-like behavior [36] can be seen in table 2.1.

| Parameter | in MPC | in experiment |
|---|---|---|
| $a$: Cell size | 1 | $1\,\mu\mathrm{m}$ |
| $\alpha$: Rotation angle | 130° | – |
| $m$: Mass of MPC particle | 1 | $m = \rho_\text{water}a^3/\langle N_c\rangle \approx 1\times 10^{-16}\,\mathrm{kg}$ |
| $\langle N_c\rangle$: Mean particles per cell | 10 | – |
| $h$: Collision time | $0.01\,\sqrt{ma^2/k_\mathrm{B}T}$ | $0.01\,\mathrm{ms}$ |
| $T$: Temperature | $1/k_\mathrm{B}$ | $300\,\mathrm{K}$ |

**Table 2.1:** Overview of all relevant parameters that are used for MPC simulations. The value for the cell size in the experiments is approximated by the length scale of a typical fluidic device. The density of water is approximated by $\rho_\text{water} \approx 1000\,\mathrm{kg/m^3}$ and room temperature is assumed.

### 2.1.5 MPCD without Hydrodynamics

In order to investigate the influence of HI a comparison between the systems with and without HI can be beneficial. However, the system without HI has to differ as little as possible from the system with HI. A simple implementation for achieving this has been proposed by Yeomans et al. in [23].

The main idea is to break the conservation of momentum and energy locally, but not globally. As explained earlier, HI are then destroyed. But the solute particles are still undergoing random Brownian motion, since they still collide with the solvent particles. Thus the solute particles behave like non-coupled particles in a fluid.

In detail, this is implemented by interchanging velocities of all particles after each collision step. Therefore a modified version of the collision step is used. After the collision step, the velocities of all solvent particles are changed to

$$\boldsymbol{v}_i'(t+h) = \boldsymbol{v}_\text{cm}(t+h) + \mathfrak{R}(\alpha)(\boldsymbol{v}_i(t+h) - \boldsymbol{v}_\text{cm}(t+h)) \tag{2.28}$$

$$= \mathfrak{R}(\alpha)\boldsymbol{v}_i(t+h)\,. \tag{2.29}$$

Due to global momentum conservation the center of mass velocity of the whole system $\boldsymbol{v}_{\text{cm}}(t+h)$ vanishes and the velocities are interchanged by rotating each velocity with the stochastic rotation matrix $\mathfrak{R}$ by an angle $\alpha$. Rotating velocities does not change the sum over all velocities and thus the global momentum is still conserved, whereas the local momentum is destroyed. The coupling between the solute particles only vanishes completely, if the rotation angle is $\alpha = \pi$. Otherwise a small coupling remains. Fluid properties that do not depend on the Velocity Autocorrelation Function (VACF) like the friction coefficient stay unchanged. But a change in the diffusion coefficient by a factor two can be measured, since the diffusion coefficient is connected to the VACF by its integral. [3]

### 2.1.6 Driven Flow under Confinement

**Hagen–Poiseuille flow** A simple geometry for which the Navier–Stokes equation can be solved analytically is the Hagen–Poiseuille flow. Here a fluid is dragged by a constant pressure gradient between two plates at rest at position $y = 0$ and $y = h$. The results of the simulation with this geometry can then be compared with the analytic solution in order to verify the correctness of the simulation. We will briefly outline here the solution for the Hagen–Poiseuille flow and calculate the viscosity $\eta$.

A detailed solution can be found in [6, chap. 3.4] and [27, chap. 2.17]. The general Navier–Stokes equation without external forces reads

$$\frac{\partial v}{\partial t} + (\boldsymbol{v}\nabla)\boldsymbol{v} = -\frac{1}{\rho}\nabla p + \frac{\eta}{\rho}\nabla^2\boldsymbol{v}\,. \tag{2.30}$$

The velocity field is given by the variable $\boldsymbol{v}$ and the pressure by $p$, while $\eta$ is the the viscosity and $\rho$ is the density of the fluid. Since we have a stationary flow in $x$ direction, the components $v_y$ and $v_z$ of $\boldsymbol{v}$ can be assumed to be zero. Due to translation invariance in $t$, $x$ and $z$, the velocity $v_x \equiv v_x(y)$ is only dependent on $y$ and all partial derivatives of $\boldsymbol{v}$ with respect to $t$, $x$ and $z$ vanish.

Thus, the Navier–Stokes equation can be reduced to two independent Ordinary Differential Equations (ODE) for the velocity component $v_x$ and the pressure $p$

$$\frac{\partial^2 v_x(y)}{\partial y^2} = \frac{1}{\eta}\frac{\partial p}{\partial x}, \quad \frac{\partial p}{\partial y} = 0\,. \tag{2.31}$$

The second equation in (2.31) states that the pressure between the two fixed plates is constant. For the left equation in (2.31) one can see that the left side is only dependent on $y$ while the right side is dependent on $x$. Thus both sides are constants and can be integrated independently. The parabolic profile can be obtained by a double integration

$$v_x(y) = \frac{1}{2\eta}\frac{\partial p}{\partial x}y^2 + ay + b\,. \tag{2.32}$$

---

[3] The VACF is often a crucial observable in the investigation of HI when looking at propelled systems. It will play a minor role in further investigations. Nevertheless, a detailed description about it and its connection to the diffusion is provided in the Appendix.

In order to solve the ODE for the velocity field, boundary conditions at the plates are needed. No-slip boundary conditions for this problem are

$$v_x(y=0)=0 \quad \text{and} \quad v_x(y=h)=0\,. \tag{2.33}$$

With these conditions the integration constants $a$ and $b$ can be determined and the solution for the Hagen–Poiseuille flow is

$$v_x(y)=-\frac{1}{2\eta}\frac{\partial p}{\partial x}y(y-h)\,. \tag{2.34}$$

A comparison between the analytic solution and the numerical results by MPC can be seen in 2.1. There, the Hagen–Poiseuille flow is simulated with a cubic box with length size $L=20\,a$ and a constant force in $x$ direction $\boldsymbol{F}=0.1\,{}^{k_\mathrm{B}T}\!/_{a}\hat{\boldsymbol{e}}_x$. The aforementioned no-slip boundary conditions are used at $y=0$ and $y=h$, while for the other directions periodic boundary conditions are applied. All other MPC parameters are set to the values from table 2.1.

The results are then fitted to equation (2.34) with $\eta$ as fit parameter. The needed relation between the pressure gradient and the force is

$$\frac{\partial p}{\partial x}=\frac{F}{L^2}\cdot\frac{N}{L}\,. \tag{2.35}$$

The fraction ${}^{F}\!/_{L^2}$ can be seen as the pressure, which, if devided by $L$, gives the pressure gradient along the $x$ direction that acts on one particle. Multiplied by the number of MPC particles $N$ we get the total pressure gradient $\frac{\partial p}{\partial x}$.

In 2.1(b) one can clearly see that the fitted analytic solution matches very well to the MPC results. Thus for the viscosity, the fit yields

$$\eta_\text{sim}=(86.4\pm0.5)\,\frac{\sqrt{k_\mathrm{B}Tm}}{a^2} \tag{2.36}$$

which is in good agreement with the analytic value which consists of a kinetic and a collisional term [17]

$$\eta_\text{theo}=\eta_\text{col}+\eta_\text{kin}=82.2\,\frac{\sqrt{k_\mathrm{B}Tm}}{a^2} \tag{2.37}$$

$$\eta_\text{col}=\frac{Nma^2}{18L^3h}(1-\cos(\alpha))\left(1-\frac{1}{\langle N_c\rangle}\right) \tag{2.38}$$

$$\eta_\text{kin}=\frac{Nk_\mathrm{B}Th}{L^3}\left[\frac{5\langle N_c\rangle}{(\langle N_c\rangle-1)(4-2\cos(\alpha)-2\cos(2\alpha))}-\frac{1}{2}\right]. \tag{2.39}$$

The analytic value for $\eta$ can be calculated with the mentioned values in table 2.1 and the length of the box $L=20\,a$.

**Rectangular Cross Section** Another important geometry for further investigations is the rectangular cross section because investigations of polymers in such a geometry will be made throughout this thesis. In this geometry the liquid flows in a rectangular shaped pipe in $x$ direction. But before solving the Navier–Stokes equation for this geometry, one can

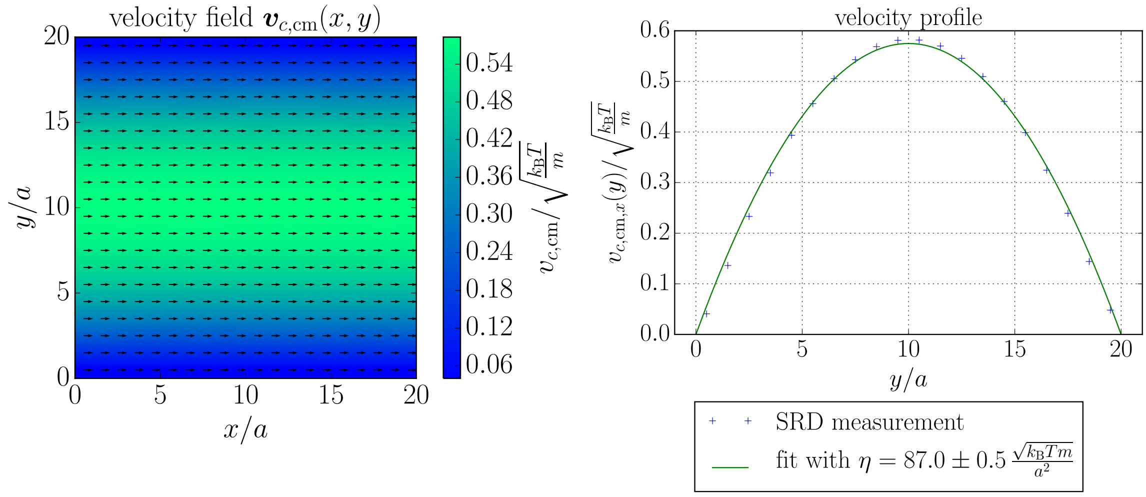

**(a)** Top view of the velocity field. The normalized vectors show the direction of the flow, while the heat map describes the speed at the positions $(x, y)$.

**(b)** Velocity profile of the flow field. The green line represents a fit to equation (2.34) of the blue points from the simulation. The fit parameter is the viscosity $\eta$.

**Figure 2.1:** Velocity field and profile for the Hagen–Poiseuille flow. The external force on the fluid is $\boldsymbol{F} = 0.1\,{}^{k_\mathrm{B}T}\!/_{a}\hat{\boldsymbol{e}}_z$, while there are no-slip boundary conditions at $y = 0$ and $y = 10\,a$. Periodic boundary conditions are used in $x$ and $z$ direction.

reduce (2.30) by applying it to an arbitrarily shaped cross section. This can also be looked up in [6, chap. 3.4] for full detail.

For an arbitrarily shaped cross section, one can assume for the velocity field $\boldsymbol{v}(\boldsymbol{r}) = v_x(y, z)\hat{\boldsymbol{e}}_x$.[4] Due to translational invariance in $x$ direction and in time $t$, $v_x$ is independent of $x$ and $t$. The vanishing forces in the $yz$-plane cause the other velocity components to be zero. Consequently the terms $(\boldsymbol{v}\nabla)\boldsymbol{v}$ and $\frac{\partial \boldsymbol{v}}{\partial t}$ vanish and the Navier–Stokes equation for an arbitrary cross section with a laminar flow in $x$ direction reads

$$\eta\nabla^2(v_x(y,z)\hat{\boldsymbol{e}}_x) - \nabla p = 0 \tag{2.40}$$

$$\Leftrightarrow \eta\left(\frac{\partial^2}{\partial y^2} + \frac{\partial^2}{\partial z^2}\right)v_x(y,z) = \frac{\partial p}{\partial x}\,. \tag{2.41}$$

Since all forces in $yz$-plane vanish the pressure $p \equiv p(x)$ only depends on $x$ and can be assumed as constant.

The no-slip boundary conditions for a rectangular cross section are

$$v_x\left(y = \frac{1}{2}w, z\right) = 0\,, \quad v_x\left(y = -\frac{1}{2}w, z\right) = 0 \tag{2.42}$$

$$v_x(y, z = 0) = 0\,, \quad v_x(y, z = h) = 0 \tag{2.43}$$

---

[4] This holds only true for low velocities since at higher velocities the laminar flow becomes unstable. At a certain speed the translation-invariance symmetry is spontaneously broken and a turbulent flow occurs [6, chap. 3.4.1].

with the height $h$ and width $w$. The closest we can get to an analytic solution for this problem is a Fourier series. We can do an ansatz for $v_x(y,z)$ as

$$v_x(y,z) = \sum_{n=1}^{\infty} f_n(y) \sin\Big(n\pi \frac{z}{h}\Big) \tag{2.44}$$

where the Fourier coefficients are constant in $z$, but vary with $y$. By inserting this into the left side of equation (2.41) and doing a Fourier expansion for the constant right side, we get

$$\sum_{n=1}^{\infty} \Big(f_n''(y) - \frac{n^2\pi^2}{h^2} f_n(y)\Big) \sin\Big(n\pi \frac{z}{h}\Big) = \frac{1}{\eta}\frac{\partial p}{\partial x}\frac{4}{\pi}\sum_{n=1}^{\infty}\frac{1}{2n+1}\sin\Big((2n+1)\pi\frac{z}{h}\Big) \tag{2.45}$$

For the right side, we expanded the constant function as a square wave function under consideration of the boundaries. Comparing the Fourier coefficients on both sides leads to

$$f_{2n}(y) = 0\,, \tag{2.46}$$

$$f_{2n+1}''(y) - \frac{(2n+1)^2\pi^2}{h^2} f_{2n+1}(y) = -\frac{1}{\eta}\frac{\partial p}{\partial x}\frac{4}{\pi}\frac{1}{2n+1}\,. \tag{2.47}$$

So the odd Fourier coefficients can be determined by solving an inhomogeneous second-order differential equation, while the even Fourier coefficients vanish. For the solution that satisfies the no-slip boundary conditions at $y = \pm{}^1\!/_2 w$, we get

$$f_{2n+1}(y) = \frac{4h^2}{\pi^3\eta}\frac{\partial p}{\partial x}\frac{1}{(2n+1)^3}\left[1 - \frac{\cosh\big((2n+1)\pi\frac{y}{h}\big)}{\cosh\big((2n+1)\pi\frac{w}{2h}\big)}\right] \tag{2.48}$$

and the final solution for the flow in the rectangular channel then becomes

$$v_x(y,z) = \frac{4h^2}{\pi^3\eta}\frac{\partial p}{\partial x}\sum_{n=0}^{\infty}\frac{1}{(2n+1)^3}\left[1 - \frac{\cosh\big((2n+1)\pi\frac{y}{h}\big)}{\cosh\big((2n+1)\pi\frac{w}{2h}\big)}\right]\sin\Big((2n+1)\pi\frac{z}{h}\Big) \tag{2.49}$$

For the comparison with the simulation, the analytic solution has to be shifted by a constant offset of ${}^w\!/_2$ because the origin of the used coordinate systems in simulation and theory differ by this offset. The Fourier expansion is done to the 10th order and the calculated viscosity $\eta_{\text{sim}}$ is used. For the simulation the same parameters as before in the Hagen–Poiseuille flow are used; the external force is again $\boldsymbol{F} = 0.1\,{}^{k_\text{B}T}\!/_a \hat{\boldsymbol{e}}_x$ and the box size is set to $L = 20\,a$. No-slip boundary conditions are set to (2.42) and (2.43). The simulation results can be seen in 2.2. In figure 2.2(a) the velocity profile in the $yz$-plane is shown, while figure 2.2(b) shows good agreement between the simulation and Fourier series.

## 2.2 The Polymer Model: Coarse-Grained Molecular Dynamics

### 2.2.1 The Polymer: Worm-Like Chain

For the polymer the model of the Worm-Like Chain (WLC) [9, 31] is used. In this model the polymer consists of $N^m$ point particles, called monomers, with mass $M$ that are bonded

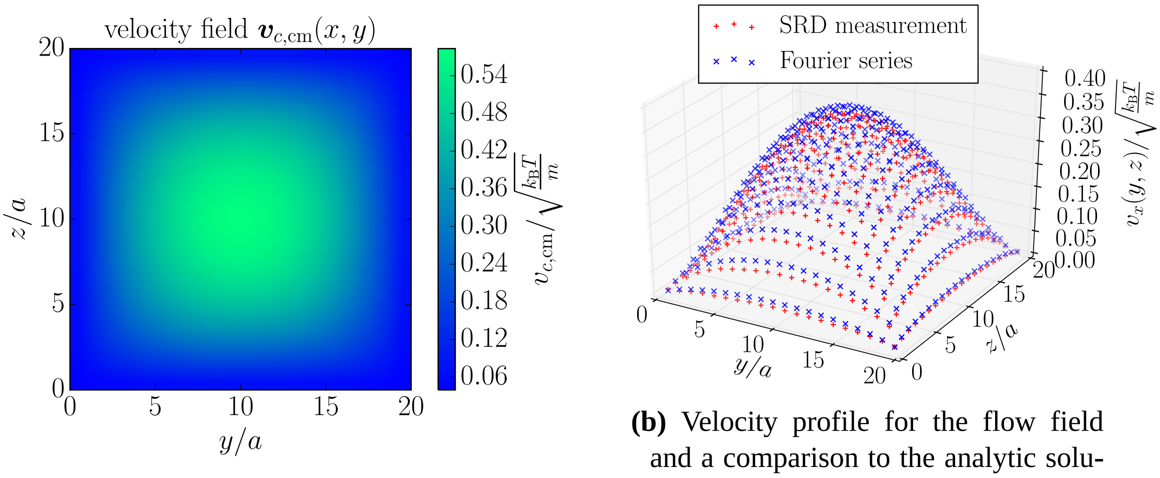

**(a)** Top view of the velocity field in the $yz$-plane. The external force points toward the viewer.

**(b)** Velocity profile for the flow field and a comparison to the analytic solution. The blue points corresponds to the analytic solution, which consists of a Fourier series. The red dots are the numeric results from the simulation.

**Figure 2.2:** Velocity field and profile for the rectangular cross section. The external force on the fluid is $\boldsymbol{F} = 0.1\,{}^{k_\mathrm{B}T}/_{a}\hat{\boldsymbol{e}}_x$, while there are no-slip boundary conditions at $(y,z) = (0,z)$, $(y,z) = (10\,a, z)$, $(y,z) = (y,0)$ and $(y,z) = (y, 10\,a)$. Periodic boundary conditions are used in $x$ direction.

via stiff springs. A certain rigidity prohibits coiling of the polymer. The combination of a monomer and a connecting spring will be called a bond and the corresponding vector $\boldsymbol{b}_n$ the bond vector. An illustration of the polymer can be seen in figure 2.3. Just like in the fluid model, one bond does not represent one carbon compound or amino acid, but a group of them that form a stiff rod where the center of mass motion is described by the dynamics of one monomer. The polymer is a connection of several stiff rods. The dynamics of the monomers are governed by Newton's equations of motion which are solved with a velocity-Verlet algorithm. This MD simulation requires force fields in order to describe their dynamic behavior. Here three different conservative forces are used whose potentials will be described in the following.

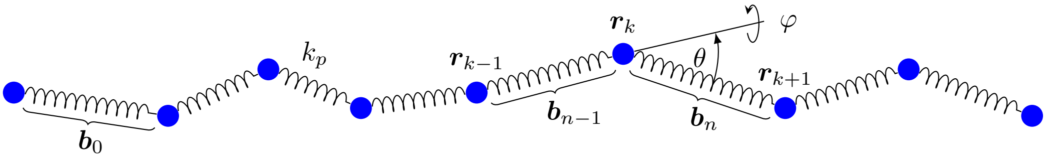

**Figure 2.3:** Representation of the polymer model with springs that have a common spring constant $\kappa$. The polymer consists of $N^m$ monomers at position $\boldsymbol{r}_k$ and $N^{m-1}$ bonds $\boldsymbol{b}_n$. $\theta$ is the polar angle and $\varphi$ the azimuthal angle between two bonds.

Since the monomers are connected via stiff springs, neighboring monomers interact via a bond potential

$$U_\mathrm{b} = \frac{k_p}{2} \sum_{k=1}^{N^m-1} \left( |\boldsymbol{r}_{k+1} - \boldsymbol{r}_k| - l \right)^2 . \tag{2.50}$$

Here, $k_p$ is the spring constant of a very stiff spring and $l$ is the rest length of this spring. This way, the two monomers fluctuate around a certain constant distance $l$.

The flexibility of the polymer can be controlled by a bending potential that takes interaction between three monomers into account. The energy needed to bend a stiff rod by a certain angle $\theta$ is described by a harmonic potential $E_\mathrm{B}$. By using an approximation for $\cos(\theta)$, this energy can be expressed by two consecutive bond vectors $\boldsymbol{b}_n, \boldsymbol{b}_{n+1}$

$$\begin{aligned} E_\mathrm{B} &= \frac{1}{2}\frac{\kappa}{l}\theta^2 \approx \frac{\kappa}{l}(1 - \cos(\theta)) \qquad &(2.51)\\ &= \frac{\kappa}{l}\left(1 - \frac{\boldsymbol{b}_n \boldsymbol{b}_{n-1}}{l^2}\right) \qquad &(2.52)\\ &= \frac{\kappa}{2l}\left(\frac{\boldsymbol{b}_n}{l} - \frac{\boldsymbol{b}_{n-1}}{l}\right)^2 . \qquad &(2.53) \end{aligned}$$

The length of the bond vectors is assumed to be the rest length of the spring potential $|\boldsymbol{b}| = l$ since $k_p \gg \kappa$ and thus $U_\mathrm{b} \gg E_\mathrm{B}$. The deviation of $|\boldsymbol{b}|$ from $l$ in every time step is considered to be small.

With the definition of the bond vectors $\boldsymbol{b}_n = \boldsymbol{r}_{n+1} - \boldsymbol{r}_n$ and $\boldsymbol{b}_{n-1} = \boldsymbol{r}_n - \boldsymbol{r}_{n-1}$ we get

$$E_\mathrm{B} = \frac{\kappa}{2l^3}\left(\boldsymbol{r}_{n+1} - 2\boldsymbol{r}_n + \boldsymbol{r}_{n-1}\right)^2 \tag{2.54}$$

and the total bending potential for the polymer can be calculated by summing over $N^m - 1$ of such stiff rods

$$U_\mathrm{B} = \frac{\kappa}{2l^3} \sum_{k=2}^{N^m-1} \left(\boldsymbol{r}_{k+1} - 2\boldsymbol{r}_k + \boldsymbol{r}_{k-1}\right)^2 . \tag{2.55}$$

A comparison with the Hamiltonian of the continuous version of the worm-like chain with contour length $L_\mathrm{C}$

$$\mathcal{H} = \int_0^{L_\mathrm{C}} \mathrm{d}s\, \frac{\kappa}{2}\left(\frac{\partial \boldsymbol{t}}{\partial s}\right)^2 , \quad \boldsymbol{t}(s) = \frac{\partial \boldsymbol{r}}{\partial s} \tag{2.56}$$

shows that the bending stiffness corresponds to a discrete version of the worm-like chain. The tangential vector $\boldsymbol{t}(s)$ in the discrete version is then the bond vector $\boldsymbol{b}_n$. The continuous variable $s$ can be seen as the contour parameter of the polymer.

A repulsive Lennard–Jones (LJ) potential is used to simulate a sphere-like exclusion volume in order to avoid entangling of polymers in between two monomers

$$U_\mathrm{LJ}(r) = 4\varepsilon\left[\left(\frac{\sigma}{r}\right)^{12} - \left(\frac{\sigma}{r}\right)^{6} + \varepsilon\right]\theta(r_c - r) . \tag{2.57}$$

Since no attraction in form of van-der-Waals forces is wanted, the LJ potential is truncated in the minimum. Therefore the cut-off radius is $r_c = 2^{1/6}\sigma$. The parameter $\sigma$ corresponds to the

| Parameter | | MD Simulation |
|---|---|---|
| $M$ | Mass of monomer | $\langle N_c \rangle \cdot m = 10\,m$ |
| $h_{\text{MD}}$ | Collision time | $0.0005\,\sqrt{ma^2/k_{\text{B}}T}$ |
| $k_p$ | Spring constant | $500\,k_{\text{B}}T/a^2$ |
| $l$ | Spring rest length | $1\,a$ |
| $\kappa$ | Rigidity | $20\,k_{\text{B}}T\,a$ |
| $\varepsilon$ | LJ energy | $1\,k_{\text{B}}T$ |
| $\sigma$ | LJ length | $1\,a$ |

**Table 2.2:** Overview of all relevant parameters that are used for the MD simulations.

radius of the excluded sphere, while $\varepsilon$ describes the strength of the repulsion. Additionally the potential is shifted by $\varepsilon$, so that $U_{\text{LJ}}$ is continuous and differentiable.

With these potentials one can derive the equations of motion for every single bead. These are first order differential equations in position and velocity and can be numerically solved by the velocity-Verlet algorithm

$$\boldsymbol{r}_i(t+h_{\text{MD}}) = \boldsymbol{r}_i(t) + h\boldsymbol{v}_i(t) + \frac{h_{\text{MD}}^2}{2M}\boldsymbol{F}_i(t) + \mathcal{O}(h_{\text{MD}}^4) \tag{2.58}$$

$$\boldsymbol{F}_i(t+h_{\text{MD}}) = \boldsymbol{F}_i(\{\boldsymbol{r}_i(t+h_{\text{MD}})\}) \tag{2.59}$$

$$\boldsymbol{v}_i(t+h_{\text{MD}}) = \boldsymbol{v}_i(t) + \frac{h}{2M}(\boldsymbol{F}_i(t) + \boldsymbol{F}_i(t+h_{\text{MD}})) + \mathcal{O}(h_{\text{MD}}^2)\,. \tag{2.60}$$

First the positions of all monomers are updated with respect to the velocity and force acting on the monomers in the current time step. With these new positions all forces are calculated for the next time step. The velocities are then updated with the mean force of the last and the next time step.

Besides a good performance due to just one force calculation per time step, the advantages of the velocity-Verlet algorithm lie in the conservation of phase space volume and the time-reversal invariance. This way the algorithm describes not only ensemble expectation values, but also dynamic variables in a physically correct way since for the dynamic variables in a classical system the Liouville theorem holds true. Both properties, phase-space volume conservation and time-reversal invariance can be proven by introducing an unitary time evolution operator or propagator $\hat{U}_{\text{V}}(t)$ for the algorithm which was done in [40]. From the determinant $\left|\det(\hat{U}_{\text{V}}(t))\right| = 1$ one can conclude the phase space volume conservation and the time-reversal invariance is given by $\hat{U}_{\text{V}}(-t) = \hat{U}_{\text{V}}(t)^{-1}$. The velocity-Verlet algorithm also provides energy conservation to the second order $\mathcal{O}(h_{\text{MD}}^2)$.

When simulating the polymers in the fluid, the streaming step (2.1) for all monomers is replaced by the velocity-Verlet algorithm. Since the time scale of a MD simulation is below that of an MPC simulation, the velocity-Verlet algorithm has to be executed $\lceil h_{\text{MD}}/h \rceil$ times per MPC step. Thus the MD simulation can stably process the hydrodynamic fluctuations due to the coupling with the fluid. The coupling is done by simply taking part in the collision step where the monomers are handled like solute particles. While the monomers are point particles and do not have an expansion, one can introduce a hydrodynamic radius $R_H$. The monomers are surrounded by fluid particles which diffuse at the same rate due to viscous forces between monomers and fluid. Thus the fluid particles create a shell around the monomers with no-slip boundary conditions on the surface of the shell. This shell can be approximated by a sphere with the hydrodynamic radius $R_H$ that can be calculated by the Stokes–Einstein–Sutherland equation

$$R_H = \frac{k_\mathrm{B}T}{6\pi\eta D} = 0.28\,a \tag{2.61}$$

where $D = 0.0023\,\sqrt{k_\mathrm{B}T/m}$ is the diffusion constant of a single unbonded monomer [39] and $\eta = 82.2\,\sqrt{k_\mathrm{B}Tm}/a^2$ the viscosity of the fluid, calculated with (2.37). So this simple coupling between polymer and fluid is sufficient for simulating physically accurate properties of the polymer.

The diffusion coefficient $D$ that depends on fluid and polymer parameters can be simulated with the parameters in table 2.2. A similar simulation with equal parameters was done in [39] where the same diffusion constant, viscosity and therefore $R_H$ was determined. The parameters in table 2.2 are also used for all further simulations of the polymer.

For simulations without HI simulated by the algorithm from 2.1.5 the diffusion coefficient drops to $D = 0.0014\,\sqrt{k_\mathrm{B}T/m}$. Therefore the hydrodynamic radius is increased to

$$R_H = 0.46\,a\,, \tag{2.62}$$

since the friction constant does not change.

### 2.2.2 Invariant Energy No-Slip Boundary Conditions

Since the streaming step for the monomers is different to the one for the fluid particles because of non-external forces, different no-slip boundary conditions at the walls have to be used. Here, such no-slip boundary conditions are proposed that preserve the advantages of the velocity-Verlet algorithm, such as energy conservation. Therefore, they are called Invariant Energy No-Slip (IENS) boundary conditions.

The IENS boundary conditions can be divided into four steps, illustrated in figure 2.4. In a) the $i$th monomer that will hit the wall during the next time step on the dashed trajectory is at the initial position $\boldsymbol{r}_i(t)$ with the velocity $\boldsymbol{v}_i(t)$. At time $t_0 = t + \Delta h_\mathrm{MD} - \Delta h_{\mathrm{MD},i}$ the monomer intersects the wall (fig. 2.4 b)), so that the monomer travels from the wall to $\boldsymbol{r}_i\big(t + \Delta h_{\mathrm{MD},i}\big)$ (fig. 2.4 c)) in the penetration time $\Delta h_{\mathrm{MD},i}$.

To calculate this time, an imaginary time step is introduced that propagates the monomer from figure 2.4 b) to 2.4 c)

$$\boldsymbol{r}_i\big(t + \Delta h_{\mathrm{MD},i}\big) = \boldsymbol{r}_i(t_0) + \boldsymbol{v}_i(t_0)\Delta h_{\mathrm{MD},i} + \frac{1}{2}\frac{\boldsymbol{F}_i(t_0)}{M}\Delta h_{\mathrm{MD},i}^2\,. \tag{2.63}$$

For reasons of simplicity the assumptions $\boldsymbol{v}_i(t_0) \approx \boldsymbol{v}_i(t)$ and $\boldsymbol{F}_i(t_0) \approx \boldsymbol{F}_i(t)$ are made. These are accurate assumptions because the configuration changes slowly for small time steps.

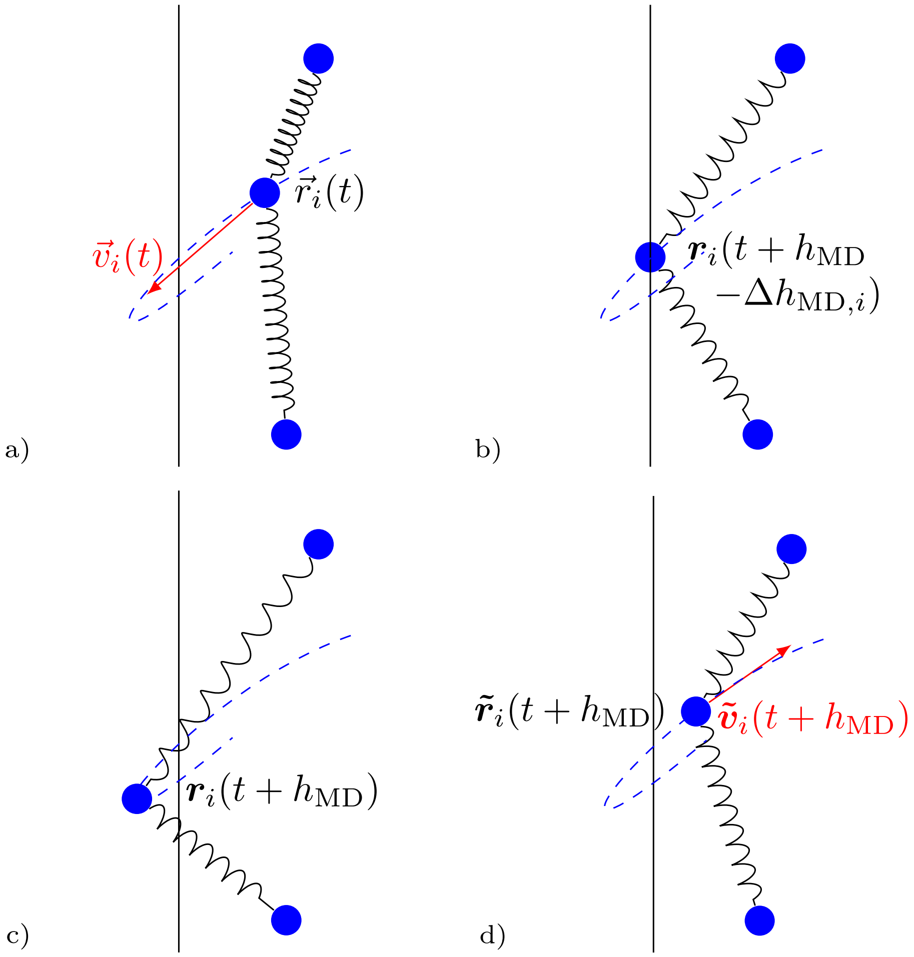

**Figure 2.4:** The invariant energy no-slip boundary conditions in four steps.

a) Configuration of the polymer at time $t$ before the $i$th monomer penetrates the wall. The blue, dashed line shows the particle's trajectory formed by the velocity $\boldsymbol{v}_i(t)$ and the force field $\boldsymbol{F}_i(t)$.

b) Imaginary configuration between two time steps at time $t_0 = t + h_{\mathrm{MD}} - \Delta h_{\mathrm{MD},i}$ where the particle hits the wall. Therefore the time $\Delta h_{\mathrm{MD},i}$ determines the travel time in the wall.

c) Configuration of the polymer at time $t + h_{\mathrm{MD}}$ where the $i$th monomer penetrates the wall for the penetration time $\Delta h_{\mathrm{MD},i}$.

d) The $i$th monomer is moved back on the trajectory by the time $-2\Delta h_{\mathrm{MD},i}$ and the velocity is inversed.

One can split up equation (2.63) in a parallel ($\|$) and orthogonal ($\perp$) component to the wall. While the parallel component can be neglected, the perpendicular component is rearranged to

$$\Delta h_{\mathrm{MD},i}^2 + \frac{2Mv_{i,\perp}(t)}{F_{i,\perp}(t)}\Delta h_{\mathrm{MD},i} + 2\frac{\Delta r_{i,\perp}M}{F_{i,\perp}(t)} = 0 \tag{2.64}$$

with $\Delta r_{i,\perp} = r_{i,\perp}(t_0) - r_{i,\perp}\big(t + \Delta h_{\mathrm{MD},i}\big)$. Here, $r_{i,\perp}(t_0)$ is the position of the wall, which is set to zero without loss of generality. Thus $\Delta r_{i,\perp} < 0$.

This quadratic equation has three different solutions

$$\Delta h_{\mathrm{MD},i} = \begin{cases} -\dfrac{v_{i,\perp}(t)M}{F_i(t)} - \sqrt{\dfrac{v_{i,\perp}^2(t)M^2}{F_{i,\perp}^2(t)} + 2\dfrac{\Delta r_{i,\perp}M}{F_{i,\perp}(t)}} & \text{if } F_{i,\perp}(t) > 0 \\ \dfrac{\Delta r_{i,\perp}}{v_{i,\perp}(t)} & \text{if } F_{i,\perp}(t) = 0 \\ -\dfrac{v_{i,\perp}(t)M}{F_i(t)} + \sqrt{\dfrac{v_{i,\perp}^2(t)M^2}{F_{i,\perp}^2(t)} + 2\dfrac{\Delta r_{i,\perp}M}{F_{i,\perp}(t)}} & \text{if } F_{i,\perp}(t) < 0 \end{cases} . \tag{2.65}$$

In the case of a force free motion the monomer is handles like a solvent particle. If the force is positive, the parabola of equation (2.64) is convex and the solution smaller than the minimum is taken. For negative forces the parabola is concave and the solution with a greater time position than the maximum is taken. This way the solution of the past and not the future is always taken. The cases may vary if $\Delta r_{i,\perp} > 0$.

The monomer can be set back into the simulation box with the velocity-Verlet algorithm by $-2\Delta h_{\mathrm{MD},i}$ to its final position, while the velocity is reversed to simulate no-slip boundary conditions

$$\tilde{\boldsymbol{r}}_i(t + h_{\mathrm{MD}}) = \boldsymbol{r}_i(t + h_{\mathrm{MD}}) - 2\Delta h_{\mathrm{MD},i}\boldsymbol{v}_i(t) + \frac{\big(-2\Delta h_{\mathrm{MD},i}\big)^2}{2M}\boldsymbol{F}_i(t) \tag{2.66}$$

$$\tilde{\boldsymbol{v}}_i(t + h_{\mathrm{MD}}) = -\boldsymbol{v}_i(t) + \frac{2\Delta h_{\mathrm{MD},i} - h_{\mathrm{MD}}}{2M}\left(\boldsymbol{F}_i(t) + \boldsymbol{F}_i(t + h_{\mathrm{MD}})\right). \tag{2.67}$$

The monomer moves back on the same trajectory, but the position does not generally coincide with the position before the wall is hit, as illustrated in figure 2.4 d). It moves towards the wall in the time $\Delta h'_{\mathrm{MD},i} = h_{\mathrm{MD}} - \Delta h_{\mathrm{MD},i}$ until the trajectory intersects the wall. From this point it propagates back by $-\Delta h_{\mathrm{MD},i}$. This is equivalent to a propagation by $-2\Delta h_{\mathrm{MD},i}$ from the position $\boldsymbol{r}_i(t + h_{\mathrm{MD}})$, since $\boldsymbol{r}_i(t_0) = \boldsymbol{r}_i\big(t - h_{\mathrm{MD}} + \Delta h_{\mathrm{MD},i}\big)$ is the position of the wall.

Thus the propagator of the boundary conditions can be written as a product of the velocity-Verlet propagator

$$\begin{aligned} \hat{U}_{\mathrm{BC}}(h_{\mathrm{MD}}) &= \hat{U}_{\mathrm{V}}\big(\Delta h'_{\mathrm{MD},i}\big) \cdot \hat{U}_{\mathrm{V}}\big(-\Delta h_{\mathrm{MD},i}\big) \\ &= \hat{U}_{\mathrm{V}}\big(\Delta h'_{\mathrm{MD},i} - \Delta h_{\mathrm{MD},i}\big) \\ &= \hat{U}_{\mathrm{V}}\big(h_{\mathrm{MD}} - 2\Delta h_{\mathrm{MD},i}\big) . \end{aligned} \tag{2.68}$$

In the second line the automorphism of propagators is used. One can see that applying the IENS boundary conditions is the same as applying the velocity-Verlet algorithm with the time step $h_{\text{MD}} - 2\Delta h_{\text{MD},i}$. Thus the propagator of the boundary conditions $\hat{U}_{\text{BC}}(h_{\text{MD}})$ is again a unitary operator and one can conclude that the propagator of the IENS boundary condition is again phase space volume conserving and time-reversal invariant. But an explicit proof for the time reversal-invariance done in the Appendix shows that the time-reversal only holds at the first order. The position shows deviations in $\mathcal{O}(h_{\text{MD}})$, while the velocity is exact.

Numerically, one can also show the energy conservation for these boundary conditions (fig. 2.5). Here a comparison between two different boundary conditions, that are applied to a simple MD simulation of a LJ fluid, is done. In (a) the kinetic, potential and total energy of the system with the IENS boundary conditions are shown, while in (b) a simple bounce back rule with

$$\tilde{\boldsymbol{r}}_i(t + h_{\text{MD}}) = \boldsymbol{r}_i(t) \tag{2.69}$$

$$\tilde{\boldsymbol{v}}_i(t + h_{\text{MD}}) = -\boldsymbol{v}_i(t + h_{\text{MD}}) \tag{2.70}$$

is used. Here, the monomers are set back to the position before the wall hit and the velocity of the current time step is reversed. For both simulations the same time step of $h_{\text{MD}} = 0.001\sqrt{m\sigma^2/48\varepsilon}$ is used. One can clearly see the energy conservation of the total energy $E_{\text{tot}}$ in (a), while the total energy is increasing for (b). Since the boundary conditions have the same propagator as the velocity-Verlet algorithm the error of the energy is of the same order $\mathcal{O}(h_{\text{MD}}^2)$.

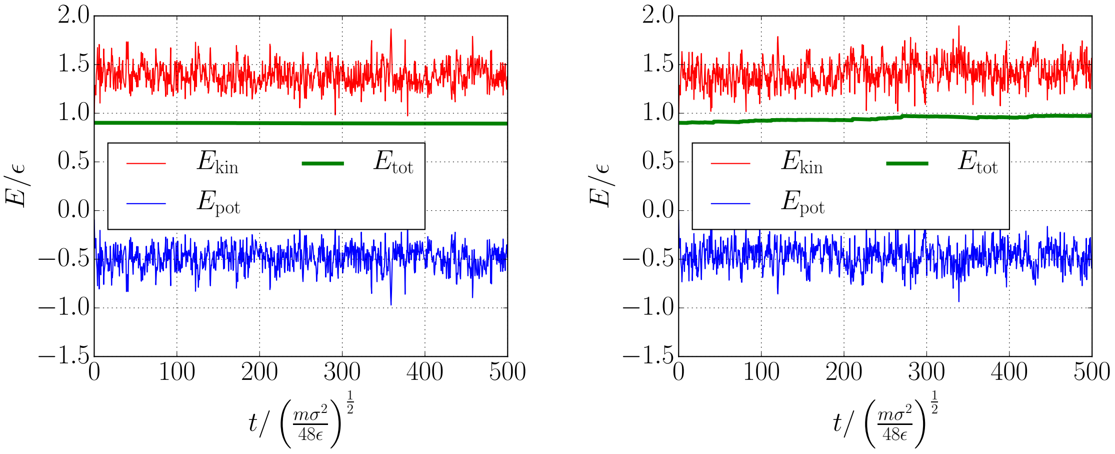

**(a)** Energies for the invariant energy no-slip (IENS) boundary conditions. The total energy $E_{\text{tot}}$ is well conserved.

**(b)** Energies for a simple bounce back boundary condition, where the position and velocity are set to (2.69) and (2.70), respectively. The total energy $E_{\text{tot}}$ is not conserved.

**Figure 2.5:** Comparison for the energies with the energy conserving no-slip boundary condition (a) and a simple bounce back boundary condition (b). Both simulations are performed under the same conditions with a two dimensional Lennard-Jones fluid and a time step of $h_{\text{MD}} = 0.001\sqrt{m\sigma^2/48\varepsilon}$.

## 2.3 The Speedup of the Simulation due to Parallelization

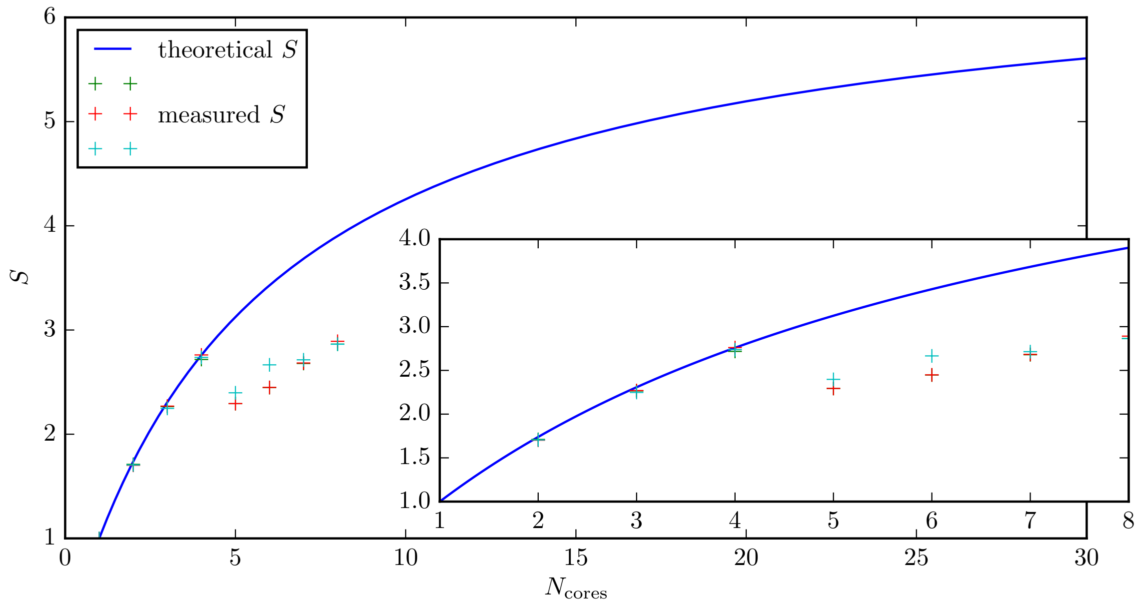

**Figure 2.6:** The speedup $S = {}^{T(1)}/_{T(N_{\text{cores}})}$ as a depedency of the number of used cores $N_{\text{cores}}$ of the workstation in comparison with the theoretical prediction made by Amdahl's law with $B \approx 0.85$. The effect of hyperthreading can be seen for the 5th to 8th cores.

In this section a closer look at the parallelization, especially the speedup $S$, of the MPC code is done. As mentioned in the beginning of this chapter, the fluid model can easily be parallelized with `openMP`. Unfortunately parallelization of the polymer simulation is too inefficient since the parallel overhead would dominate over the gain of time. Thus, only a fraction $B$ of the complete code is parallel. The main parallel code consists of the streaming step, the collision step and the calculation of the center of mass velocities $\boldsymbol{v}_{c,\text{cm}}$. Caution has to be exercised by the calculation of $\boldsymbol{v}_{c,\text{cm}}$ because two particles in one cell handled by two different threads would contribute to the same center of mass velocity. This would lead to multiple writing of threads and an incorrect result of the simulation. Gracefully the `openMP` library provides a simple statement

```
#pragma omp atomic update
```

that updates the center of mass velocities atomically [7].

A theoretical prediction of the speedup $S$ of a program can be made with Amdahl's law [3]

$$S = \frac{T(1)}{T(N_{\text{cores}})} = \frac{1}{(1-B) + \frac{1}{N_{\text{cores}}} B} \tag{2.71}$$

where $B$ is the fraction of parallel code. The speedup is a factor that describes how much faster a program runs when $N_{\text{cores}}$ physical and logical cores are used compared to single threading. It is useful for deciding how many cores to use, or whether parallelization is appropriate in the first place. Hence, $T(1)$ is the run time of single threading and $T(N_{\text{cores}})$ that of multithreading. In the best case $S \propto N_{\text{cores}}$. Now Amdahl's law predicts this factor under the assumption that the amount of parallelized code is the bottleneck. It states that the multithreaded run time consists of the non-parallel code and the parallel code that runs $N_{\text{core}}$ times faster.

The measured speedup $S$ on the workstation and the theoretical prediction can be seen in figure 2.6. While the figure displays a theoretical prediction for a high number of cores, the figure in figure shows a comparison between measured values and theory. The amount of parallel code is approximately $B \approx 0.85$.

The measured speedup follows the theoretical predicted for the first four cores quiet well. Then the speedup drops and hardly increases for $N_{\text{cores}} > 5$. This is due to hyperthreading of the workstation. The workstation consists of four physical and four logical cores. Physical cores are real existing cores in the computer, while logical cores are abstract entities that share physical resources with the physical cores. So logical cores do not contribute to the performance of the code as seen in 2.6. Thus the optimal number of threads for this simulation is only determined by the number of available physical cores.

For the high numbers of physical cores however one can clearly see, that in theory the speedup stagnates after approximately $N_{\text{cores}} > 25$. At this limit a higher number of cores does not lead to a significant change in the speedup and more parallelization is not efficient. But the number of cores in the workstation is far away from this limit and parallelization on more cores could still lead to a higher speedup in theory. However, for more parallelization an implementation of the algorithm on a GPU architecture should be considered. These are more practical for the use of parallel code.

# 3 Results

## 3.1 The Tangential Correlation Function

### 3.1.1 Definition and General Properties

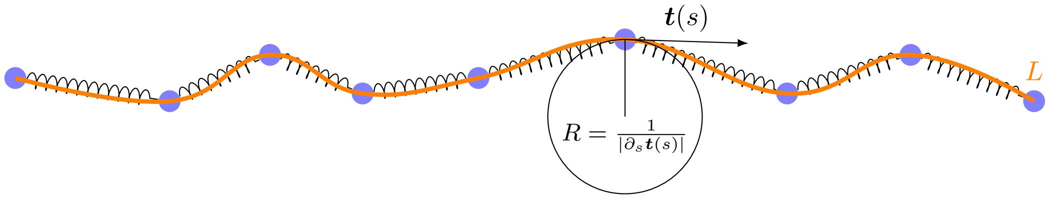

**Figure 3.1:** A pictorial description of the tangential vector $\boldsymbol{t}(s)$. It is perpendicular to the curvature of the polymer and the derivative is the inverse curvature radius. Thus it describes the spacial orientation for the contour parameter $s$.

The first step in verifying the correct dynamics of the polymer can be done by investigating the behavior of the Tangential Correlation Function (TCF). The TCF can be seen as the autocorrelation function [1] of the tangential vectors. In figure 3.1 a pictorial description of the tangential vector in the continuous version of the WLC is given. It can be seen that it gives the spacial orientation for the contour parameter $s$. Thus, correlating this quantity will give the autocorrelation of the orientation throughout the polymer. So the TCF is the orientation correlation of the polymer.

For measuring correlation functions, an average $\langle ... \rangle$ has to be taken. Here the ensemble average is implied which can be calculated by the time average due to validity of the ergodic hypothesis in the simulation.

In the continuous version of the WLC the tangential correlation function can be calculated by the path integral over all possible tangent vector configurations

$$\langle \boldsymbol{t}(0)\boldsymbol{t}(s)\rangle = \frac{1}{Z}\int_{|\boldsymbol{t}(s')|=1} \mathcal{D}\boldsymbol{t}(s')\,\boldsymbol{t}(0)\boldsymbol{t}(s)\exp\left(-\frac{\mathcal{H}[\boldsymbol{t}(s')]}{k_{\mathrm{B}}T}\right) \tag{3.1}$$

under the constraint of normalized tangent vectors. Every path is weighted by its probability given by the Boltzmann factor $\exp(-\mathcal{H}[\boldsymbol{t}(s')]/k_{\mathrm{B}}T)$. Normalization occurs via the partition function $Z$ which is obtained as the summation over all possible configurations. The Hamiltonian $\mathcal{H}$ is a functional of the tangential vector $\boldsymbol{t}(s)$. It contains all the information

---

[1] A definiton is given in 3.2.1.

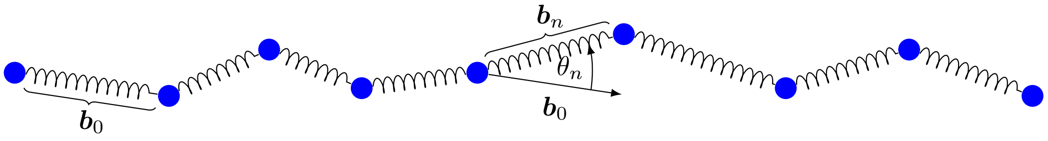

**Figure 3.2:** A schematic illustration of the polymer with its bond vectors $\boldsymbol{b}_n$. In the simulation the tangential correlation function (TCF) is calculated by the autocorrelation of their unit vectors. The angle between the bond vectors $\boldsymbol{b}_0$ and $\boldsymbol{b}_n$ is denoted by $\theta_n$.

about the system that is needed to calculate the TCF. Because of the constraint the actual calculation of the path integral is rather difficult and will not be executed in detail in the next sections. It only shows a formal way to calculate the TCF.

In the discrete version the tangential vectors are replaced by the bond vectors $\boldsymbol{b}$. [2] Then the TCF reads

$$\left\langle \frac{\boldsymbol{b}_0}{|\boldsymbol{b}_0|} \cdot \frac{\boldsymbol{b}_n}{|\boldsymbol{b}_n|} \right\rangle = \langle \cos(\theta_n) \rangle \, . \tag{3.2}$$

The angle $\theta_n$, as illustrated in figure 3.2, is the angle between the $n$th and the zeroth bond. In the simulation the correlation function is calculated by iterating over every bond $\boldsymbol{b}_m$ twice. Every $\boldsymbol{b}_m$ is multiplied by the bond $\boldsymbol{b}_n$ with $n \geq m$. Therefore, $\boldsymbol{b}_0$ in 3.2 does not denote to a fixed bond, but to the bond $n$ before $\boldsymbol{b}_n$. In order to avoid finite-size effects, bonds near the free ends are not taken into account. Additionally the TCF is averaged over roughly $10^7$ MPC time steps.

### 3.1.2 The Free Worm-Like Chain

The WLC in the continuous version can be described by the Hamiltonian, already mentioned in chapter 2.2.1

$$\mathcal{H}[\boldsymbol{t}(s)] = \int_0^{L_\mathrm{C}} \mathrm{d}s \, \frac{\kappa}{2} \left( \frac{\partial \boldsymbol{t}}{\partial s} \right)^2 . \tag{3.3}$$

For this Hamiltonian the path integral for the TCF yields an exponential decay

$$\langle \boldsymbol{t}(0)\boldsymbol{t}(s) \rangle = \exp\left( -\frac{k_\mathrm{B}T}{\kappa} s \right) \tag{3.4}$$

$$= \exp\left( -\frac{s}{L_\mathrm{P}} \right) \tag{3.5}$$

with the persistence length $L_\mathrm{P} = \frac{\kappa}{k_\mathrm{B}T}$ in three dimensions.

---

[2] This approximation can be made for semiflexible polymers where the orientation does not change significantly over bond length $b$. More precisely the persistence length $L_\mathrm{P}$ has to be larger than $b$.

Hence, the persistence length is the correlation length of a free polymer. The correlations between two bonds decay to $^1\!/\mathrm{e}$ after the persistence length. As already described in the introduction, it also corresponds the stiffness of the polymer. This can be seen in its definition by the connection to the rigidity. The higher the persistence length, the longer the correlation and thus the stiffer the polymer.

In figure 3.3 a consistency check with the TCF of a free WLC is done. Its correct behavior verifies that the simulated polymer has the same properties as the free WLC. Thus, the correctness of the fluid and polymer simulation without confinement is insured.

Figure 3.3(a) shows exemplary results for different rigidities $\kappa$. The solid lines correspond to a fit function (3.5) with $L_\mathrm{P}$ as a fit parameter. The polymer consists of $N^m = 33$ monomers and is simulated in a cubic box with length $L = 35\,a$. Periodic boundary conditions are applied to every side of the box. Since one can see finite-size effects in form of undulations at the ends, the zeroth bond for measuring the TCF starts at the eighth bond. Therefore, $n = 0$ denotes the eighth bond. These undulations also occur at the other end at the $n > 10$, so that only the first ten values are considered for the fit.

The fitted $L_\mathrm{P}$ are then plotted against the associated rigidity (fig. 3.3(b)). As expected the relation is linear with a slope of approximately $m \approx 1$, since the temperature is set to $k_\mathrm{B}T = 1$. The exact slope from the linear regression is

$$m = 1.07 \pm 0.09\,. \tag{3.6}$$

Deviations in the persistence length occur because finite-size effects are not completely prevented. They vanish with longer polymers, but simulating longer polymers leads to longer $L$ that is connected to the run time by $\mathcal{O}(L^3)$.

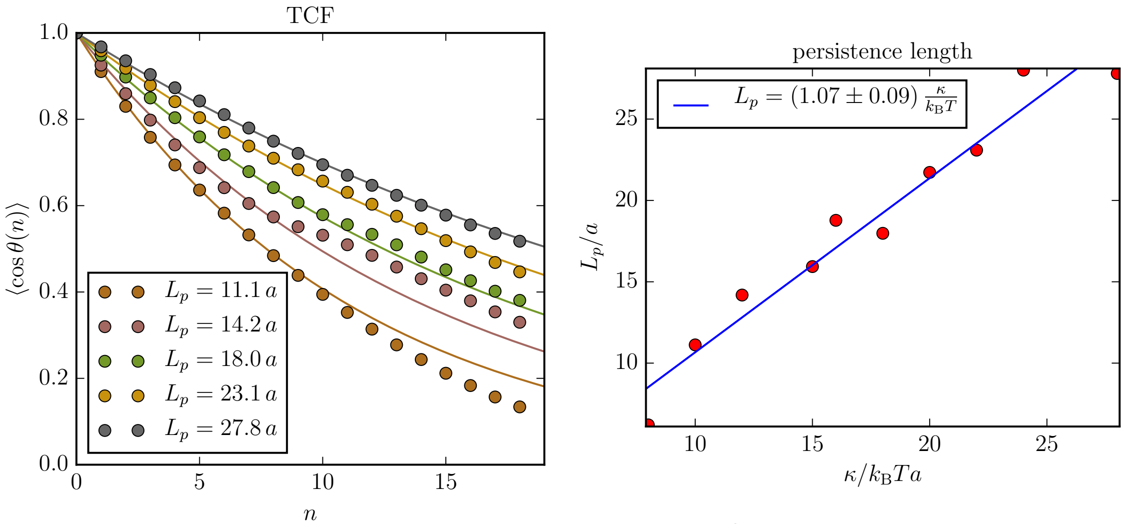

**(a)** The TCF for the free WLC polymer for different rigidities $\kappa = L_\mathrm{P}k_\mathrm{B}T$. $n$ denotes the bond number in the correlation function. The fits are done for the first ten values.

**(b)** The fitted persistence lengths $L_\mathrm{P}$ from figure 3.3a are plotted versus the rigidities $\kappa$. As expected these show a linear relationship with a slope of approximately $m \approx 1$.

**Figure 3.3:** The tangential correlation function (TCF) for the free worm-like chain for different rigidities $\kappa$ and its association to the persistence length $L_\mathrm{P}$.

### 3.1.3 The Worm-Like Chain in a Rectangular Confinement

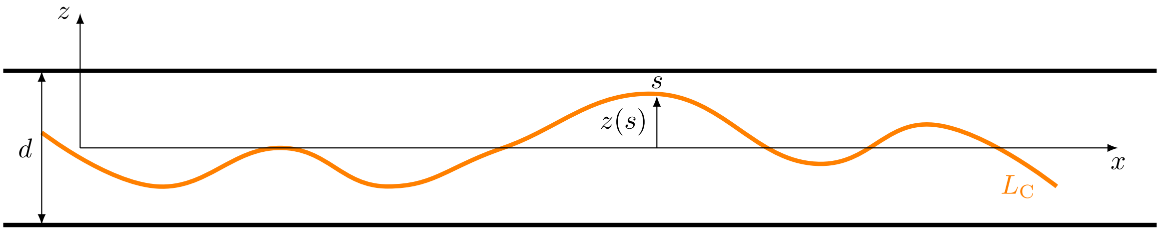

**Figure 3.4:** Top view of a polymer confined in a rectangular channel. The $y$-axis points perpendicularly to the $z$- and $x$-axis into the image plane. $z(s)$ describes the displacement in the $z$ direction at $s$. $d$ corresponds to the width of the channel, whereas $h$ is the height. For reasons of simplicity, both are set equal $d = h$.

A confined polymer in a rectangular channel can theoretically be described by a parabolic potential in the direction of the confinement. Therefore the Hamiltonian in (3.3) is expanded by quadratic terms in $y$ and $z$

$$\mathcal{H}[\boldsymbol{r}(s)] = \int_0^{L_\mathrm{C}} \mathrm{d}s \left[ \frac{\kappa}{2} \left( \frac{\partial^2 \boldsymbol{r}}{\partial s^2} \right)^2 + \frac{1}{2} \left( K_y y^2(s) + K_z z^2(s) \right) \right] . \tag{3.7}$$

Here $z(s)$ and $y(s)$ are the displacements perpendicular to the channel and $z = y = 0$ correspond to the center as one can see from figure 3.4. There the displacement in $z$ direction is labeled, while the displacement in $y$ direction is perpendicular to the image plane. $K_y$ and $K_z$ determine the strength of the confinement and are connected to the width $d$ and height $h$ of the channel. For weakly bent polymers or small displacement gradients, this approximation becomes exact [25].

Theoretical predictions for the TCF of confined polymers were done for this Hamiltonian in [25]. Since they were falsified in experiments and Monte-Carlo simulations, polymers confined in such a rectangular channel with hard walls can sufficiently be described by (3.7). Thus, a comparison with simulation results will show, whether the dynamics of a confined polymer is correctly reproduced by this mesoscopic simulation.

The TCF using this Hamiltonian was calculated in [13, 25] in the limit of large $L_\mathrm{C}$. The correlations change significantly in comparison with the free polymer, since the confinement leads to a distinguished direction of the tangential vectors. The calculation yields a function $G(\zeta)$ for every confined direction [13] and the TCF reads

$$\langle \cos(\theta(s)) \rangle \approx 1 - sG\left(\frac{s}{\lambda_y}\right) - sG\left(\frac{s}{\lambda_z}\right) \quad \text{with} \tag{3.8}$$

$$G(\zeta) = \frac{1}{2\sqrt{2} L_\mathrm{P} \zeta} \left( \cos\left(\frac{\pi}{4}\right) - \cos\left(\frac{\pi}{4} + \zeta\right) \exp(-\zeta) \right) . \tag{3.9}$$

Here, a second set of parameters besides the persistence length is needed to describe the polymer. These are the deflection lengths $\lambda_y$ and $\lambda_z$. They are connected to the strength of the confinement

$$\lambda_i = \left(\frac{4\kappa}{K_i}\right)^{\frac{1}{4}}, \quad i = y, z\,. \tag{3.10}$$

While the persistence length is the correlation length for the free polymer, the deflection length is the correlation length of a confined polymer. When choosing a channel with equal width than height $d = h$, then one has $K \equiv K_y = K_z$ and therefore $\lambda \equiv \lambda_y = \lambda_z$. So both functions $G(\zeta)$ are equal in equation (3.8). The TCF in the case of a channel with a rectangular cross section can then be written as

$$\begin{aligned} \langle\cos(\theta(s))\rangle &\approx 1 - 2sG\Big(\frac{s}{\lambda}\Big) && (3.11)\\ &\approx 1 - \frac{\lambda}{\sqrt{2}L_{\mathrm{P}}}\Big(\cos\Big(\frac{\pi}{4}\Big) - \cos\Big(\frac{\pi}{4} - \frac{s}{\lambda}\Big)\exp\Big(-\frac{s}{\lambda}\Big)\Big)\,. && (3.12)\end{aligned}$$

The impact of the confinement on the TCF can be seen for high values of $s$

$$\lim_{s\to\infty}\langle\cos(\theta(s))\rangle = 1 - \frac{\lambda}{2L_{\mathrm{P}}}\,. \tag{3.13}$$

The correlation function first decays like a free polymer until collisions with the channel walls occur and turn the polymer contour. The point of re-correlation is given by the deflection length $\lambda$ because the minimum of the function is only dependent on $\lambda$ [25].

Now we want to have a closer look at the displacement $z(s)$. [3] From elasticity theory [26, chap. 2.20] it is well known that small displacements $z(s)$ for a constant force $F$ acting perpendicularly to the tangential vector on semiflexible polymer can be described by the ODE

$$\kappa\frac{\partial^4 z(s)}{\partial s^4} - \frac{\partial F}{\partial s} = 0 \quad \Rightarrow z^2(s) \propto \frac{F}{\kappa}s^4 \propto \frac{W}{\kappa}s^3\,. \tag{3.14}$$

A qualitative behavior of the square displacement $z^2(s)$ can be deduced by inserting the typical scales. Here the definition of the mechanical work $W = Fs$ is used. When looking at thermalized polymers, the source for this mechanical work that bends the polymer is thermal fluctuation. Thus, the connected energy is the thermal energy $1\,k_{\mathrm{B}}T$ and the mean square displacement of $z(s)$ becomes

$$\langle z^2(s)\rangle \propto \frac{s^3}{L_{\mathrm{P}}}\,. \tag{3.15}$$

Since the polymer experiences the confinement after the deflection length $\lambda$, one can state that the mean square displacement has to be of the order of the squared channel width $d^2$ that matches the confining potential

$$\begin{aligned} \langle z^2(\lambda)\rangle &\propto d^2 && (3.16)\\ \frac{\lambda^3}{L_{\mathrm{P}}} &\propto d^2\,. && (3.17)\end{aligned}$$

---

[3] Since $d = h$, the displacement $y(s)$ will show the same behavior and the following calculation can be made analogically.

This finally leads to a term for the deflection length

$$\lambda = cL_{\mathrm{P}}^{\frac{1}{3}}d^{\frac{2}{3}} \tag{3.18}$$

with a geometry-dependent numerical prefactor $c$. With this expression for the deflection length, one can see that the correlation function can be described without detailed confinement information. An arbitrarily shaped confinement therefore will yield the same correlation function as a parabolic potential with the according confinement strength $K$. The numerical prefactor $c$ however cannot be determined analytically. These were numerically calculated with Monte-Carlo simulations of fluctuating polymers which show good agreement of the parabolic potential approximation with hard channel walls.

Besides a linear relationship for equation (3.18), the numerical prefactor can also be determined with the master curve. When multiplying the shifted TCF with $d^{-\frac{2}{3}}L_{\mathrm{P}}^{\frac{2}{3}}$, all correlation functions for different widths $d$ collapse onto one master curve

$$\begin{aligned} \mathcal{C}_c(x = sd^{-\frac{2}{3}}L_{\mathrm{P}}^{\frac{2}{3}}) &\approx d^{-\frac{2}{3}}L_{\mathrm{P}}^{\frac{2}{3}}(1 - \langle\cos(\theta(s))\rangle) && (3.19)\\ &= \frac{c}{2\sqrt{2}}\left[\cos\Big(\frac{\pi}{4}\Big) - \cos\Big(\frac{\pi}{4} + \frac{x}{c}\Big)\exp\Big(-\frac{x}{c}\Big)\right]. && (3.20) \end{aligned}$$

The master curve is then only dependent on the rescaled variable $x$ and the numerical prefactor $c$. Two-dimensional Monte Carlo simulations could determine the prefactor to $c = 0.76$ for hard channel walls. But since this factor is geometry-dependent, it may differ for three-dimensional simulations and different boundary implementations.

In order to determine this factor, the TCF is measured for a polymer in a rectangular confinement for different width $d$ and constant length $L = 85\,a$. For simplicity, the height and width are set to the same value. The length of the polymer is $N^m = 83$. Figure 3.5 shows the different TCF and the associated fits. The fit parameter is the deflection length $\lambda$, while the persistence length is constantly $L_{\mathrm{P}} = 20\,a$ for all TCFs. To avoid the finite-size effects, the zeroth bond for the measurement starts at the 18th bond. The fit is done for $n < 40$.

The master curve is calculated according to (3.20). Then, the average over all master curves is fitted with $\tilde{c}$ as fit parameter. The same parameter $\hat{c}$ is gained by a linear regression according to (3.18). The numerical prefactor therefore is

$$\tilde{c} = 0.68 \qquad \hat{c} = 0.70 \pm 0.05\,. \tag{3.21}$$

The fit error of the master curve is neglectably small. Thus, the prefactor in our simulations is slightly smaller than the one in Monte Carlo simulations.

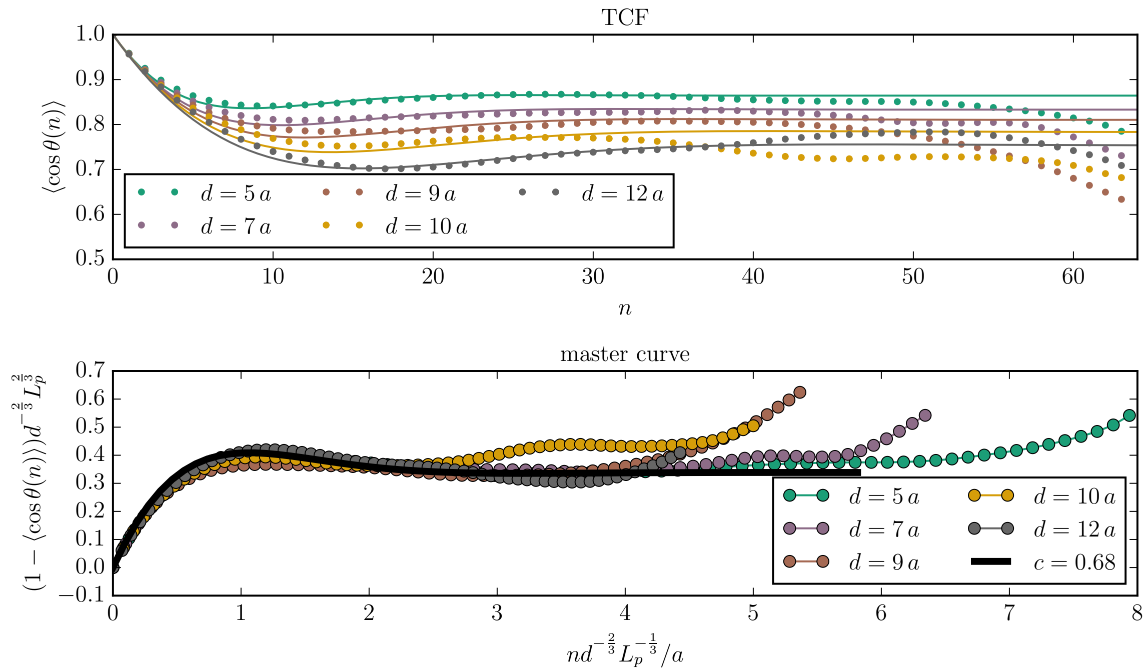

**Figure 3.5:** The upper plot shows the tangential correlation function (TCF) for different channel widths and heights $d$. The solid lines represent the fit with equation (3.12) where the deflection length $\lambda$ is fitted. Due to finite-size effects the fit is done until the 40th value. The lower plot shows the master curve (3.20). All TCFs collapse onto this master curve and the numerical factor $\tilde{c}$ can be fitted.

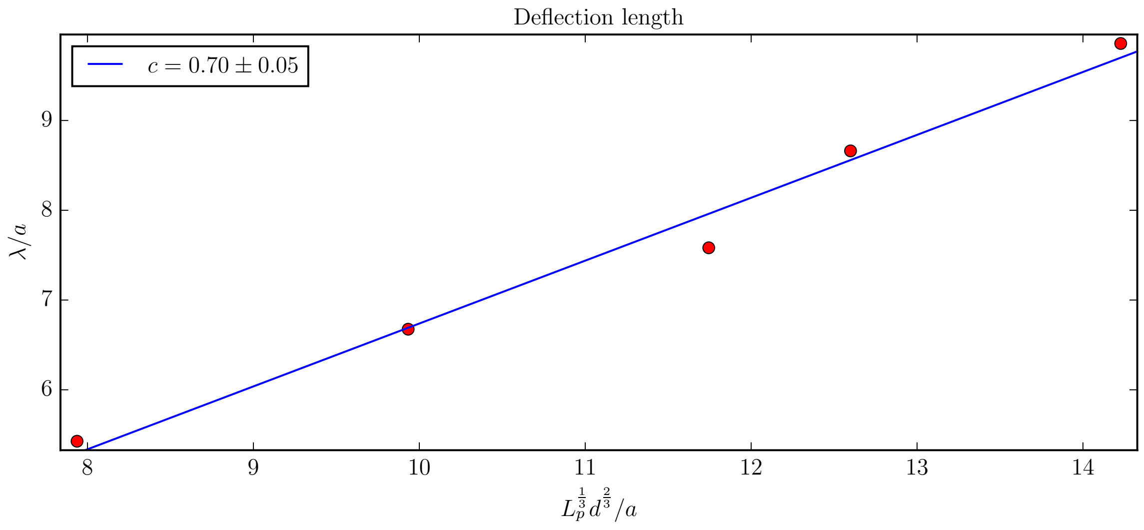

**Figure 3.6:** The fitted deflection length from 3.5 are plotted against a product of persistence length $L_\mathrm{P}$ and channel width $d$. With a linear relationship the numerical factor $\hat{c}$ is determined again.

## 3.2 Hydrodynamic Interactions

### 3.2.1 The Cross- and Autocorrelation Function

In order to investigate HI different observables can be used to examine the dynamics of the different simulation setups. Depending on the observable, one can reveal different information about the investigated system, other might remain unknown. Here, we are interested in ensemble correlations between different monomers that interact with each other by hydrodynamics. In general, an ensemble correlation function between two observables $A$ and $B$ is defined as

$$C_{AB}(t) = \langle A(t')B(t'+t)\rangle_{\text{eq}} \tag{3.22}$$

where the average is taken as the equilibrium ensemble average. Due to ergodicity in all the considered systems, the ensemble correlation equals the time correlation.

Thus, the Cross-Correlation Function (CCF) and Autocorrelation Function (ACF) are chosen to investigate the measured trajectories $\boldsymbol{r}_n$ of two distinct monomers in the simulation. General mathematical properties of the CCF and ACF will be described in this subsection.

The CCF for two infinite, time-dependent signals $f(t)$ and $g(t)$ is defined as

$$C_{fg}(t) \equiv \langle f(t')g(t'+t)\rangle = \int_{-\infty}^{\infty} \mathrm{d}t'\, f(t')g(t'+t) \tag{3.23}$$

$$\approx \sum_{m=0}^{N-n} \frac{f(t_m)g(t_m+t_n)}{N-n}\,. \tag{3.24}$$

For a better comparison, the two functions are calibrated by their mean first, so that $f$ and $g$ are defined as

$$f(t) = \bar{f}(t) - \langle \bar{f} \rangle \tag{3.25}$$

$$g(t) = \bar{g}(t) - \langle \bar{g} \rangle\,. \tag{3.26}$$

If any of the functions $\bar{f}$ or $\bar{g}$ is a constant function, the ACF becomes zero, since either $f(t)$ or $g(t)$ is zero $\forall t$.

The ACF can be interpreted as the average of $g$ at a certain time $t'+t$, weighted by $f$. The time difference between the two functions will be denoted as time lag $t$. More general, the ACF detects similar curve shapes for two non-constant signals $f$ and $g$. If two periodic functions $f(t+\tau) = g(t)\,\forall t$ with the phase shift $\tau$, the CCF has an extremum at the phase shift $t = \tau$. The type of extremum depends on the sign of $\tau$: If $\tau > 0$, it is a maximum, whereas for $\tau < 0$ it is a minimum. A vanishing phase shift reveals that the two signals are synchronized. Therefore, this tool helps to detect synchronized motion between two randomly moving monomers or polymers.

A special case of the CCF is the ACF. The ACF is defined for a single infinite, time-dependent signal $f(t)$ as

$$C_{ff}(t) \equiv \langle f(t')f(t'+t)\rangle = \int_{-\infty}^{\infty} \mathrm{d}t'\, f(t')f(t'+t) \tag{3.27}$$

$$\approx \sum_{m=0}^{N-n} \frac{f(t_m)f(t_m+t_n)}{N-n}\,. \tag{3.28}$$

While the CCF detects similarities between two different signals, the ACF finds self-similarities in the investigated signal. So the ACF of a periodic function is always a periodic function with a certain phase shift. Furthermore, at $t = 0$ the ACF becomes the variance of the signal.

For further investigations, its properties about handling signals with noise will be of special interest. When correlating white noise, the ACF becomes a δ-peak at $t = 0$. This reflects the missing content of information in white noise, since no value in such a signal is correlated with another. Hence, a signal covered by white noise can be uncovered with the ACF.

Since the signals gained from simulations are neither infinite nor continuous, a finite and discrete approximation for the ACF and CCF has to be used. They can be approximated by a sum that is normalized by the difference of the length $N$ of the signal and the current time index $n$ as displayed in (3.24) and (3.28). When correlating two finite signals by this method, for every $t_n$ a sum has to be calculated. Thus, the run time turns out to be $\mathcal{O}(N^2)$. With $N \sim 2 \times 10^7$ this implementation is rather slow. An alternative Fast Fourier Transform algorithm from [21] is used. This takes advantage of the fact that the convolution in fourier space equals the product and a correlation function can be turned into a convolution if $f$ is an Hermitian function by inverting the time. The two signals are first transformed into Fourier space, multiplied, and then retransformed into real space. The run time $\mathcal{O}(N \log(N))$ is determined by the run time of a Fast Fourier Transformation.

The difference $\mathit{\Delta}(t) = f(t) - g(t)$ also plays a crucial role in investigating hydrodynamic correlations. In the simulations this difference will correspond to the projected difference between the two measured trajectories. The ACF for this function can be calculated to

$$\begin{aligned} \langle \mathit{\Delta}(t')\mathit{\Delta}(t'+t)\rangle &\equiv \langle (f(t') - g(t'+t))(f(t'+t) - g(t'+t))\rangle && (3.29)\\ &= \langle f(t')f(t+t')\rangle - \langle f(t')g(t'+t)\rangle \\ &\quad - \langle g(t')f(t+t')\rangle + \langle g(t')g(t'+t)\rangle && (3.30)\\ &= 2(\langle f(t')f(t'+t)\rangle - \langle g(t')f(t'+t)\rangle)\,. && (3.31) \end{aligned}$$

From (3.30) to (3.31) the assumption of

$$\langle f(t')f(t'+t)\rangle = \langle g(t')g(t'+t)\rangle \quad \text{and} \quad \langle g(t')f(t'+t)\rangle = \langle f(t')g(t'+t)\rangle \tag{3.32}$$

are used. The first assumption is valid if both signals contain the same information due to symmetry of the investigated system. The second one assumes commutativity which is in general not the case for correlation functions. However, for even functions $f$ and $g$ the correlation equals the convolution which is a commutative operation.

In the context of correlation functions, it should not go unmentioned that correlation does not imply causality. One cannot conclude interactions between the two investigated monomers only from correlations. But either an analytic calculation or a comparison with the same simulated system with one different parameter, can ensure the causality for the correlations.

### 3.2.2 Correlations of Two Trapped Monomers

Before studying HI for different polymer systems, a simple and well-known system of two trapped monomers is investigated. The simulation setup is illustrated in figure 3.7. Experimental and theoretical results about the behavior of such a system are well-known [4, 16,

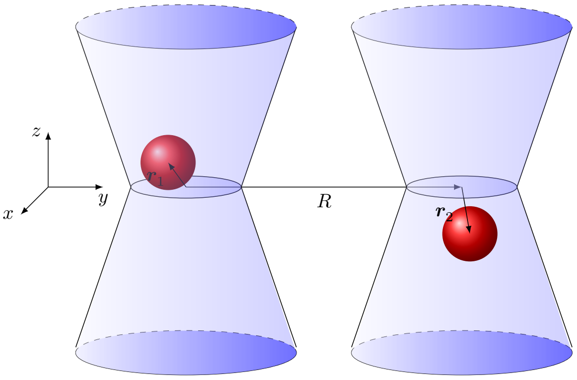

**Figure 3.7:** Simulation setup for two monomers in two optical traps with distance $R$. The optical traps keep the monomers fixed to the origin of their relative coordinate with $\boldsymbol{F}_{\text{trap}} = -K\boldsymbol{r}_n$. With this setup, the autocorrelation function (ACF) and cross correlation function (CCF) in the positions $r_{ny}$ and the difference $(\boldsymbol{r}_2 - \boldsymbol{r}_1)|_y$ are measured. Experimental results with the same setup were gained in [16, 30].

30]. In previous publications, the above described CCF and ACF on the trajectories $r_{ny}$ were measured and calculated analytically. Thus, from a comparison between the established results and the analyzed data from the simulation, one can verify the existence of HI in the simulation and ensure the correct correlations due to HI.

As mentioned in the introduction, the velocity of one particle is coupled to the force field of the other particle by the Oseen tensor $\boldsymbol{H}$ (see (1.1)). So the equations of motion for the two particles in two optical traps are

$$\frac{\mathrm{d}\boldsymbol{r}_n}{\mathrm{d}t} = \sum_{m=1}^{2} \boldsymbol{H}(\boldsymbol{r}_n - \boldsymbol{r}_m)[-K\boldsymbol{r}_m + \boldsymbol{f}_m(t)] \tag{3.33}$$

with the Oseen tensor

$$\boldsymbol{H}(\boldsymbol{r}_n - \boldsymbol{r}_m) = \frac{\delta_{nm}}{6\pi\eta R_H}\mathbb{1} + \frac{1-\delta_{nm}}{8\pi\eta|\boldsymbol{r}_n - \boldsymbol{r}_m|}\left(\mathbb{1} + \frac{(\boldsymbol{r}_n - \boldsymbol{r}_m)\otimes(\boldsymbol{r}_n - \boldsymbol{r}_m)}{|\boldsymbol{r}_n - \boldsymbol{r}_m|^2}\right). \tag{3.34}$$

The first term corresponds to the self-interaction that consists of the particle's mobility $\mu$. The mobility is the inverse friction coefficient $\xi = 6\pi\eta R_H$ from Stokes flow. Here, it is assumed that the extension of the particle is described by the hydrodynamic radius $R_H$. However, in calculations from [30] the actual radii from the experimental beads were used. The second term is already mentioned in the introduction and describes the interaction between the two monomers.

The force field consists of the restoring force by the optical trap and a fluctuating force $\boldsymbol{f}_m(t)$ with the moments

$$\langle \boldsymbol{f}(t)\rangle = 0 \tag{3.35}$$
$$\langle \boldsymbol{f}_n(t)\boldsymbol{f}_m(t')\rangle = 2\boldsymbol{H}^{-1}(\boldsymbol{r}_n - \boldsymbol{r}_m)k_{\mathrm{B}}T\,\delta(t-t')\,. \tag{3.36}$$

Due to the second law of thermodynamics the mean of the fluctuating force has to vanish. Deviations would lead to a temperature gradient between the bath and the monomers and therefore a propulsion. The second moment is connected to the temperature of the system and the inverse Oseen tensor.

The equations (3.33) can be solved for strong trap constants, since the distance between monomers and therefore the Oseen tensor is constant. For $K \sim 1000\,k_{\mathrm{B}}T/a^2$, the mean square deviation is then $\langle r_{ny}^2\rangle = {}^{k_{\mathrm{B}}T}/_{K} = 0.001\,a^2$ (equipartition theorem for the harmonic oscillator). Then, the equations of motion become coupled, linear ODEs that can be decoupled by introducing the relative coordinates

$$r_{+i} = \frac{1}{\sqrt{2}}(r_{1i} + r_{2i}) \tag{3.37}$$

$$r_{-i} = \frac{1}{\sqrt{2}}(r_{1i} - r_{2i})\,. \tag{3.38}$$

The mode $r_{+i}$ describes the center of mass and $r_{-i}$ the relative motion in the coordinate $i$ between the two monomers.

With a straightforward calculation one gets the ACF and CCF of the trajectories

$$\big\langle r_{1i}(t')r_{1j}(t'+t)\big\rangle = \big\langle r_{2i}(t')r_{2j}(t'+t)\big\rangle \tag{3.39}$$

$$= \delta_{ij}\frac{k_\mathrm{B}T}{2K}\big(\mathrm{e}^{-\xi_+ t} + \mathrm{e}^{-\xi_- t}\big) \tag{3.40}$$

$$\big\langle r_{1i}(t')r_{2j}(t'+t)\big\rangle = \big\langle r_{2i}(t')r_{1j}(t'+t)\big\rangle \tag{3.41}$$

$$= \delta_{ij}\frac{k_\mathrm{B}T}{2K}\big(\mathrm{e}^{-\xi_+ t} - \mathrm{e}^{-\xi_- t}\big) \quad \text{with} \quad \xi_\pm = \frac{1 \pm \gamma}{\tau}\,. \tag{3.42}$$

They can be interpreted as the superposition of the relaxations of the two modes $r_{+i}$ and $r_{-i}$ with the relaxation constants $\xi_+$ and $\xi_-$, respectively. These constants depend on the fundamental relaxation time $\tau = {}^{\xi}\!/\!_{K}$ and the dimensionless parameter $\gamma$. The relaxation time is determined by the friction coefficent $\xi = 6\pi\eta R_H$ and the trap strength $K$, whereas $\gamma$ is the ratio of the mobility of the monomers and the strength of their hydrodynamic coupling. For the $y$ component that is parallel to their distance, one gets $\gamma = {}^{3R_H}\!/\!_{4R}$.

In the special case of only one monomer in the optical trap, equation (3.33) is turned into the Langevin equation

$$\xi\frac{\mathrm{d}\boldsymbol{r}}{\mathrm{d}t} = -K\boldsymbol{r} + \boldsymbol{f}(t) \quad \text{with} \tag{3.43}$$

$$\langle \boldsymbol{f}(t)\rangle = 0 \tag{3.44}$$

$$\langle \boldsymbol{f}(t)\boldsymbol{f}(t')\rangle = k_\mathrm{B}T\xi\,\delta(t-t')\,. \tag{3.45}$$

The ACF for this equation of motion is then an exponential decay

$$\langle r_i(t')r_i(t'+t)\rangle = \frac{k_\mathrm{B}T}{K}\mathrm{e}^{-\frac{t}{\tau}} \tag{3.46}$$

with the same relaxation time as before [9, chap. 3.5].

Without hydrodynamics the ACF for the two monomer system becomes the mean over the ACFs of the two one monomer systems. But since the hydrodynamic coupling is weak, the curve shapes hardly differ. The CCF, however, is very sensitive to changes in the relaxation constants. For equal relaxation constants, the CCF vanishes, while for $\xi_+ < \xi_-$, it has positive values and for $\xi_+ > \xi_-$ it is negative. Correlations due to HI are most likely to occur in the CCF.

In figure 3.8 the CCF (upper plot) and ACF (lower plot) for the $y$ component of the trajectory $\boldsymbol{r}_n$ are plotted for different distances $R$ for a high trap constant $K = 1000\,k_\mathrm{B}T/a^2$. The simulations are carried out according to the setup described by figure 3.7 in a cubic box with $L = 10\,a$ and the two monomers positioned in the middle of the optical traps. The parameters used for the fluid are displayed in table 2.1, while table 2.2 contains all parameters about the monomers.

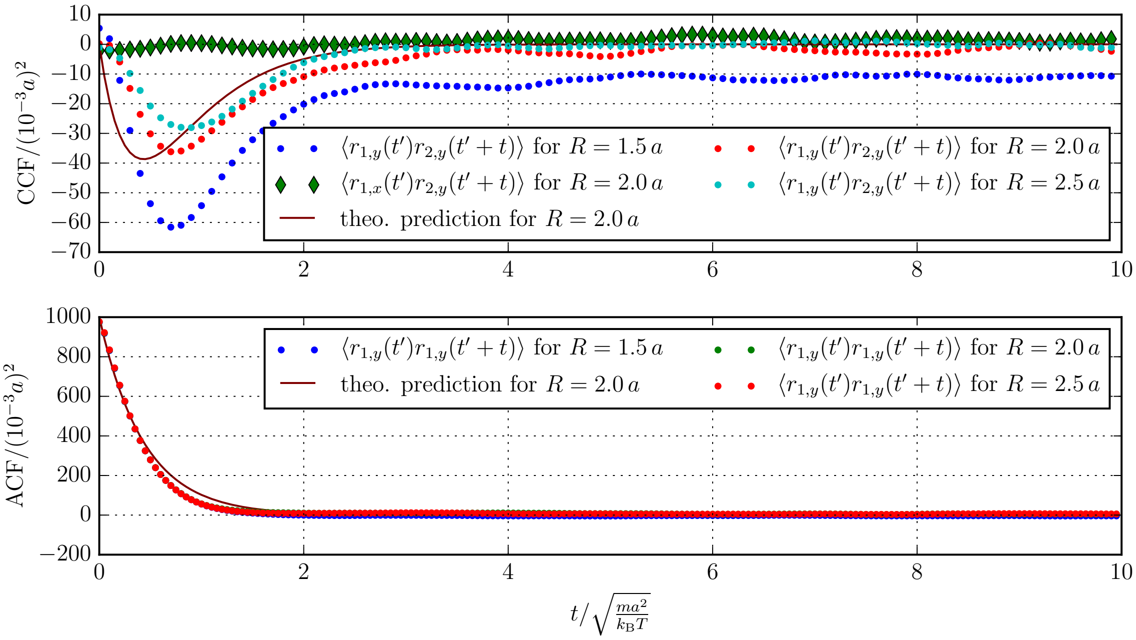

**Figure 3.8:** The autocorrelation (ACF) and cross correlation functions (CCF) for different distances $R$ with a high trap constant $K = 1000\,k_\mathrm{B}T/a^2$. Additionally, the theoretical predictions from equations (3.40) and (3.42) are plotted with solid lines. The diamonds show the vanishing correlation between perpendicular components of $\boldsymbol{r}$.

In the upper plot the green diamonds represent the vanishing CCF of two perpendicular components such as $x$ and $y$. For the distance of $R = 2\,\mathrm{a}$ the CCF without hydrodynamics is plotted with purple stars. The algorithm which destroys HI as described in 2.1.5 is used. As expected this function vanishes which shows that the method successfully destroys the hydrodynamic coupling between the two monomers. Additionally the theoretical predictions by (3.40) and (3.42) are plotted for the distance of $R = 2\,a$. The relaxation constants $\xi_\pm$ can be calculated by the fluid and monomer properties.

One can see that the theoretical predictions fit well to the results gained from the simulation. From the negative values one can conclude that $\xi_- < \xi_+$. Therefore, the relative mode is relaxating slower than the center of mass mode. One can interpret that the monomers are moving in sync since their difference stays correlated longer than the center of mass. The simulation results and calculations show that the cause for this effect is HI. In a pictorial explanation one monomer is first being pushed out of the resting position of the trap. Due to local momentum conservation the momentum change is transferred to the other monomer. Thus, the other monomer experiences the movement and is dragged in the same direction. From the position $t_\mathrm{min}$ of the minima one can conclude that the HI is not instantaneous and the correlations do not depend on the distance $R$.

Next, we want to investigate the limits of the approximation for a constant distance between the monomers. Then the ODEs (3.33) become non-linear, since the Oseen tensor is not constant and depends on $\boldsymbol{r}_n$. Finding an analytic solution for these non-linear ODEs is a difficult task and the ACF and CCF are therefore unknown. In the approach taken here, the trap constant $K$ is lowered by two orders of magnitude, but the distance between the traps is kept constant at $R = 2\,a$. For $K \sim 10\,k_\mathrm{B}T/a^2$ the mean square deviation becomes

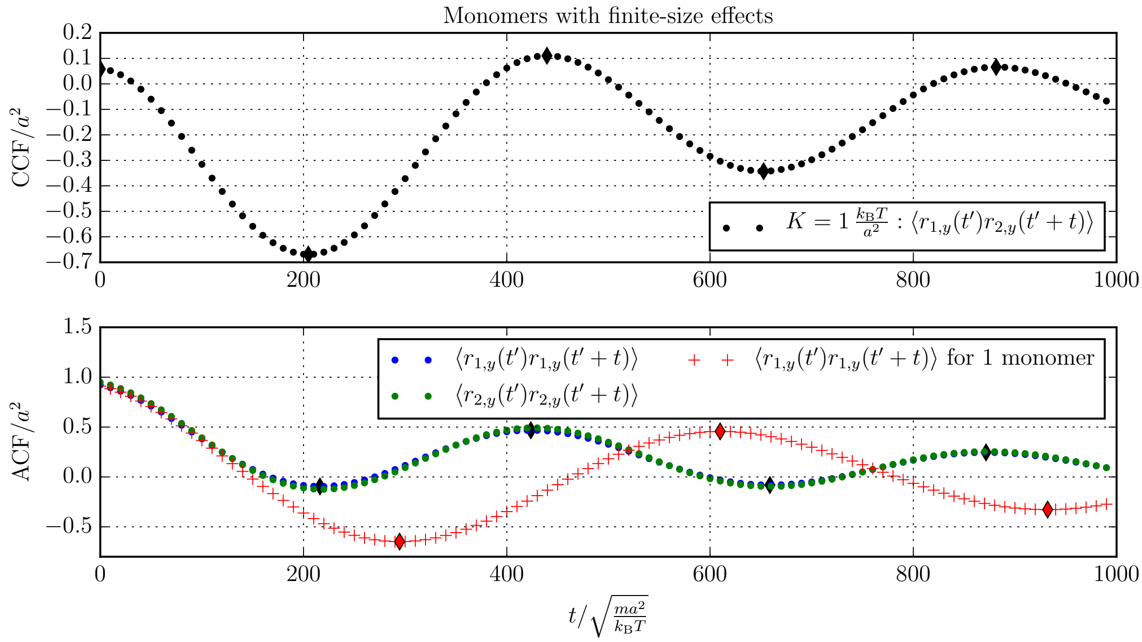

**Figure 3.9:** Finite-size effects on the auto (ACF) and cross correlation function (CCF) for one and two monomers in optical traps at distance $R = 2\,a$ and a low trap constant $K = 1\,k_\mathrm{B}T/a^2$. The simulations are carried out for a cubic box with $L = 10\,a$ and periodic boundary condition. Because of the periodic boundaries, the monomers can interact with their mirror images via hydrodynamics. The diamonds point out the extrema of the according function.

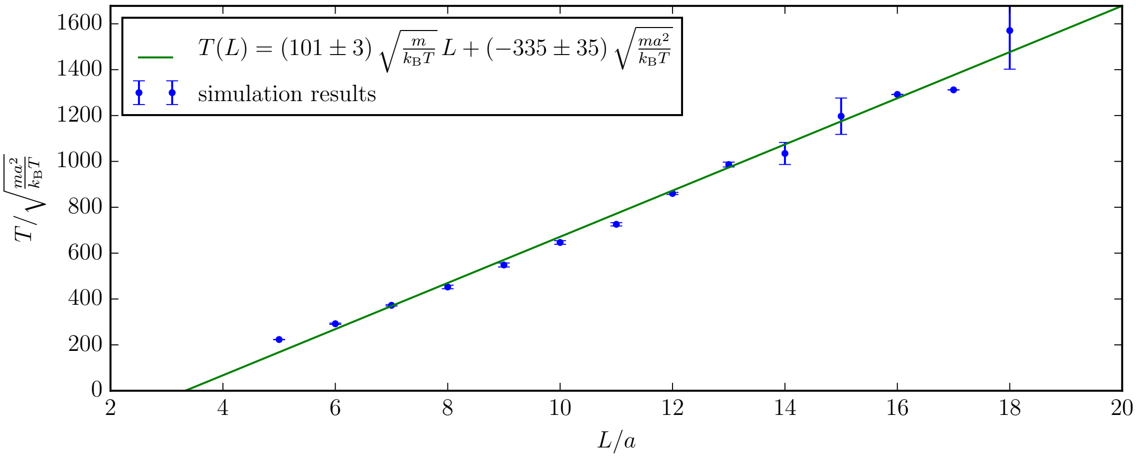

**Figure 3.10:** The periodic time $T$ versus the box length $L$ for one monomer. The simulations are done with periodic boundary conditions. Therefore finite-size effects occur. The periodic time is calculated by the mean on the differences in the maxima of the ACF with the standard deviation as its error.

$\langle r_{ny}^2\rangle = 0.1\,a^2$. The distance between the monomers can no longer be considered constant.

For these simulations one can easily encounter finite-size effects. With periodic boundary conditions on a cubic box, the monomers start to interact with their mirror images via HI. As pictured in figure 3.9 one monomer in an optical trap with a trap constant of $K = 1\,k_\mathrm{B}T/a^2$ starts to oscillate. This can be seen by the oscillating ACF of the one monomer curve. The movement of two monomers is then synchronized which can be seen by the CCF. The CCF is also oscillating with the same frequency and encounters its first maxima at zero. Thus, their phase shift vanishes.

This phenomenon occurs, since the HI is a long range interaction that decays with $\propto {}^{1}\!/_{|\boldsymbol{r}_n - \boldsymbol{r}_m|}$. The movement of the monomer creates a back flow behind the monomer, that drags the mirror images and therefore the monomer itself, in the direction of the movement. Contrary to this movement, the trap force pushes it back to the resting position. Thus, the monomer in the trap can be considered to be a driven harmonic oscillator due to self-interactions.

The periodic time $T$ of such an oscillation can be approximated by two times the mean of the differences between the extrema. Its error is the standard deviation. The extrema are evaluated with a peak-detection algorithm. So for one and two monomers at a box length $L = 10\,a$ one gets

$$T_1 = (640 \pm 20)\sqrt{\frac{ma^2}{k_\mathrm{B}T}} \tag{3.47}$$

$$T_2 = (440 \pm 10)\sqrt{\frac{ma^2}{k_\mathrm{B}T}}\,. \tag{3.48}$$

The scaling of the periodic time versus the length $L$ for one monomer can be seen in figure 3.10. As expected the periodic time is linear in the length and the dependency for the frequency is therefore $\omega \propto {}^{1}\!/_{L}$. The effect is decaying very slowly with longer box lengths and does not vanish for simulable box sizes. This especially illustrates the long range of HI.

This effect cannot be avoided when simulating an infinite system by periodic boundary conditions. But since the investigated correlations also occur in finite, closed systems, no-slip boundary conditions on every box side are used. So the two monomers in the two optical traps are simulated in a closed cubic box with same length $L = 10\,a$ as before. The optical traps are placed in the center of the box with a distance of $R = 2\,a$ to avoid interactions with the walls.

Exemplary results for different $K$ can be seen in 3.11. Even for lower $K$ one can still see the typical minima, pointed out by the diamonds in the plots. The ACF shows the expected exponential behavior with a different relaxation constant. Surprisingly, the theoretical predictions for the CCF are still in good agreement for the plotted simulation results. However their calculations are done for a constant distance between the monomers. Here, deviations in the distance are one order of magnitude below $R$.

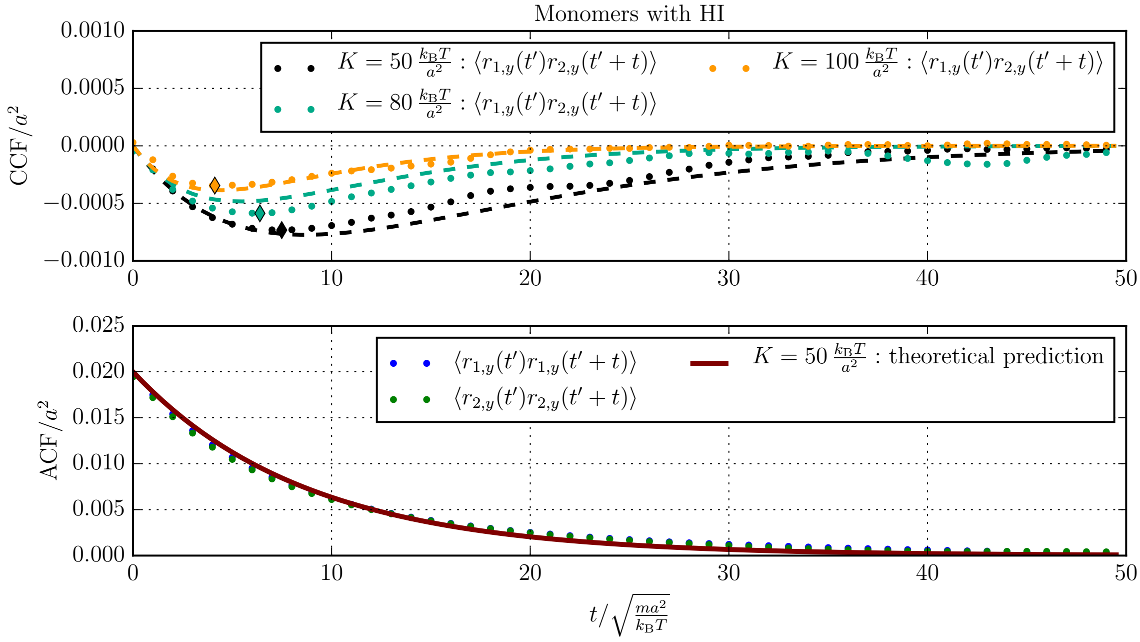

**Figure 3.11:** The autocorrelation (ACF) and cross correlation function (CCF) for two monomers at distance $R = 2\,a$ with low trap constants $K = 50, 80, 100\,k_BT/a^2$ and no finite-size effects. The dashed lines are the associated theoretical predictions. The ACF is only plotted for $K = 50\,k_BT/a^2$ with the associated theoretical prediction.

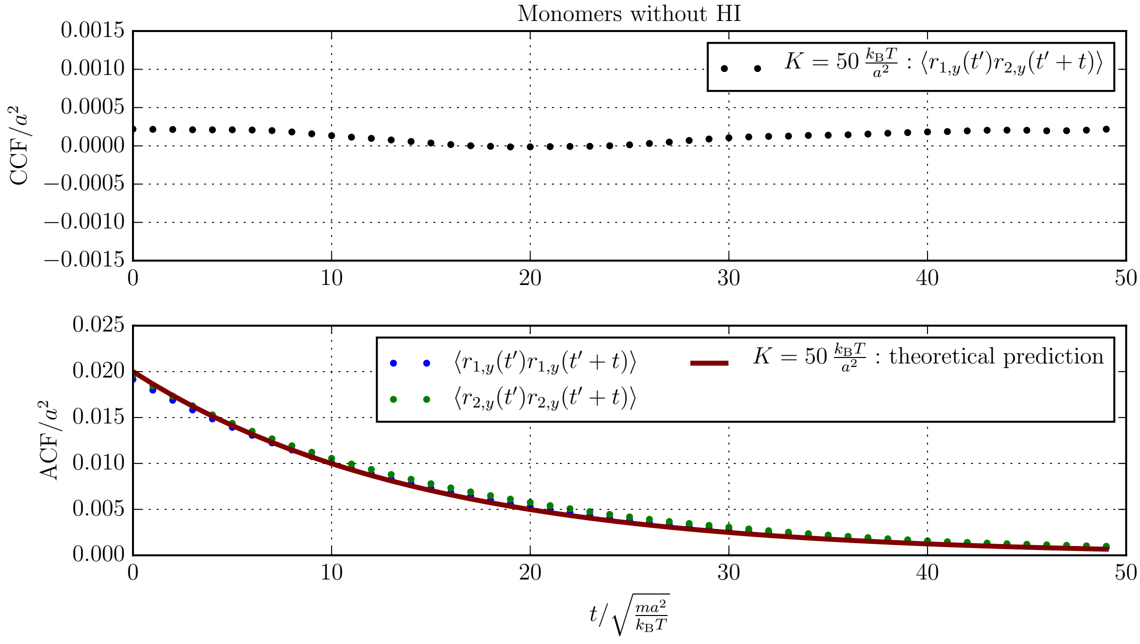

**Figure 3.12:** The autocorrelation (ACF) and cross correlation function (CCF) for two monomers at distance $R = 2\,a$ with a low trap constant $K = 50\,k_BT/a^2$. Hydrodynamics is turned off. Additionally, the theoretical prediction for the ACF with the reduced diffusion $D = 0.0014\,\sqrt{k_BT/m}$ is plotted.

For comparison the same simulations are carried out without hydrodynamics with the algorithm from 2.1.5 in figure 3.12. The minima in the CCF clearly vanish, while the ACF shows an exponential decay predicted by the ACF (3.46) from the Langevin equation. Note that the ACF from figure 3.11 differs from the one in 3.12. Its only cause is the side effect on the diffusion constant which changes the relaxation time $\tau$, too. For the CCF, $\gamma$ becomes zero without hydrodynamic coupling and both modes decay the same. Thus, all correlations between the two monomers are zero.

Nevertheless, the agreement between the theoretical prediction and the simulation results decays for lower trap constants and greater deviations. Since the minimum is a characteristic property of the CCF, its progress with $K$ can reveal information about the deviation to the theoretical prediction. Hence, a closer look at the minimum is taken.

According to [30], the position $t_{\text{min}}$ and value at the minimum of the theoretical CCF is

$$t_{\text{min}} = \frac{\tau}{2\gamma}\log\left(\frac{1+\gamma}{1-\gamma}\right) \approx \tau \approx \frac{\xi}{K} \tag{3.49}$$

$$\langle r_{1i}(t')r_{2j}(t'+t_{\text{min}})\rangle \approx -\frac{\sinh(\gamma)k_{\text{B}}T}{\text{e}}\frac{1}{K}\,. \tag{3.50}$$

The minima from the simulation results are again evaluated by the peak-detection algorithm. Both, the theoretical approximation and the simulation results are then plotted for different $K$ in figure 3.13. For $K \gtrsim 20\,k_{\text{B}}T/a^2$, the white area in 3.13, the simulation results fit very well to the theoretical predictions. But deviation can be seen for $K \lesssim 20\,k_{\text{B}}T/a^2$. Hence, it is assumed that the theoretical CCF from (3.42) is valid down to $K \approx 20\,k_{\text{B}}T/a^2$.

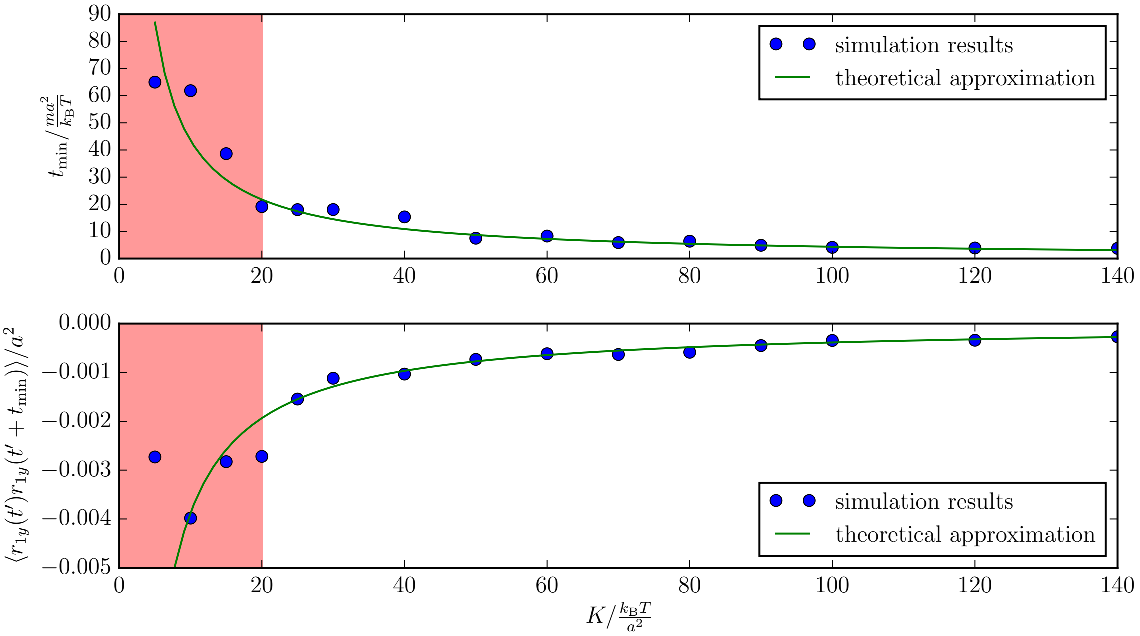

**Figure 3.13:** The time position $t_{\text{min}}$ (upper plot) and the value of the minima of the cross correlation function (CCF). The solid line shows the minima by theoretical prediction of the CCF. The prediction is valid for the white area, while deviations can be seen for the red area.

### 3.2.3 Correlations of Two Trapped Polymers

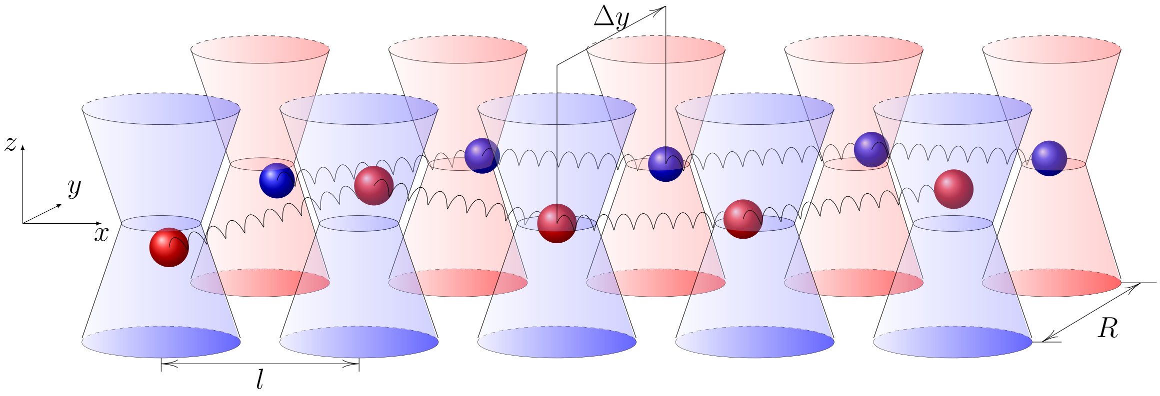

**Figure 3.14:** Simulation setup for two polymers in optical traps. The optical traps keep all monomers fixed to their origin with a common trap constant $K$, while they are still connected by springs and a rigidity. The autocorrelation function (ACF) and cross-correlation function (CCF) in the positions $\boldsymbol{r}_n$ and the difference $\Delta y$ are measured for the center monomer in the respective chain.

Now we want to focus on a system of two confined polymers in order to come closer to the experimental setup from [38]. But before reproducing the experiment, an interim step is introduced where every monomer of the two polymers is confined by optical traps. A pictorial description of this setup is given in figure 3.14. The optical traps with a mutual trap constant $K$ are placed on two straight lines with a distance of $R = 2\,a$. The distance between two optical traps on one line is the resting length of the used polymer spring $l = 1\,a$.

Hence, the ACF and CCF are measured for the middle monomers numbered by $\lfloor {}^{N^m}\!/_2 \rfloor$. Their relative position to the resting position will be denoted $\boldsymbol{r}_p$ with $p \in \{1, 2\}$ for the number of the polymer. Additionally, the ACF for the projected difference $\Delta y = r_{2y} - r_{1y}$ is calculated for a comparison with the experimental results. A consistency check can be done with formula (3.31) which reveals conformity with the measured ACF and CCF in the relative positions.

Those functions are surveyed for different numbers of monomers $N^m$ in each polymer. We want to analyze the influence of other monomers on the three functions. Each monomer can interact with any other monomer by HI and monomers in the same polymer are still coupled by rigidity and springs. In order to avoid finite-size effects, the two polymers are centered in a cubic channel with length $L = 15\,a$ and a rectangular cross section in the $yz$-plane. With an odd number of monomers, the two middle monomers are in the center of the cubic channel and interactions with the walls are avoided.

Simulations are done for two different trap constants $K = 50, 1000\,k_\mathrm{B}T/a^2$. Exemplary results for the high trap constant $1000\,k_\mathrm{B}T/a^2$ can be seen in figure 3.15. Due to the high trap constant, the positions of the monomers can again be considered to be fixed. Thus, rigidity and spring constants do not play a significant role. For the CCF one can see that the minimum is shifted significantly to lower times and higher values for $N^m = 3$. But the minimum does not change for higher polymer length. One can conclude that monomers further away play a minor role on the CCF. The correlations as well as the time of correlations between the middle monomers are mostly reduced by their next neighbors.

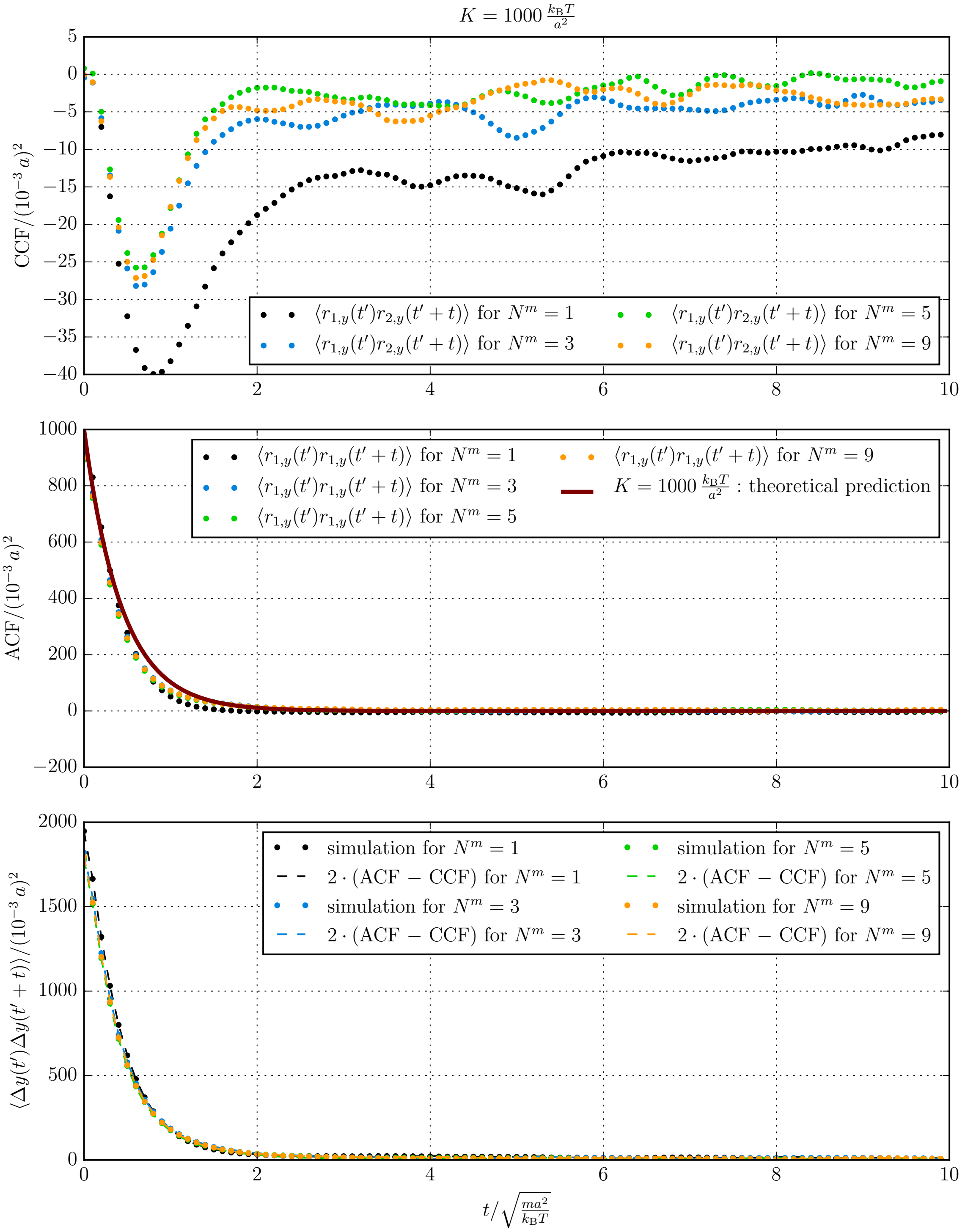

**Figure 3.15:** The influence of different polymer length $N^m$ on the autocorrelation (ACF) and cross correlation function (CCF) on the center monomers. For the simulation measurement the two polymers are confined by optical traps with high trap constants $K = 1000\,k_BT/a^2$ as described in figure 3.14. The distance between the optical traps of the two polymers is $R = 2\,a$. Additionally the ACF for the difference $\Delta y$ is calculated and plotted.

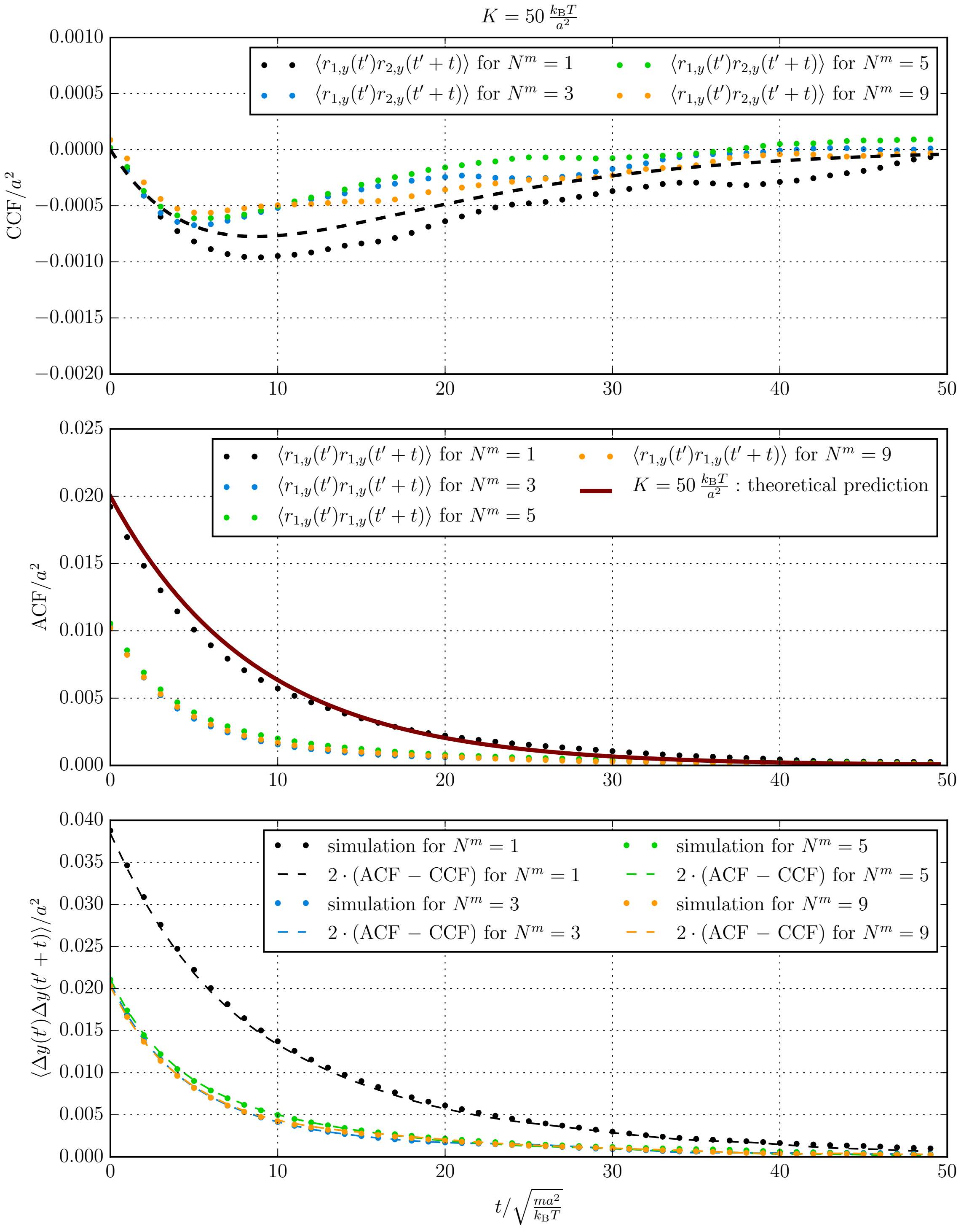

**Figure 3.16:** The influence of different polymer length $N^m$ on the autocorrelation (ACF) and cross correlation function (CCF) on the monomers in the middle. For the simulation measurement the two polymers are confined by optical traps with high trap constants $K = 50\,k_\mathrm{B}T/a^2$ as described in figure 3.14. The distance between the optical traps of the two polymers is $R = 2\,a$. Additionally the ACF for the difference $\Delta y$ is calculated and plotted.

The ACF does not change at all for longer polymers. Due to symmetry the ACFs of both monomers are equal and only one of them is plotted for simplicity. It still agrees very well with the theoretical prediction that is used before.

The additionally plotted $\langle \Delta y(t')\Delta y(t'+t)\rangle$ is the ACF of the projected difference $\Delta y$. Since it is dominated by the ACF as one can see from (3.31), it shows a similar curve as the ACF above it. But no oscillations like the ones observed in the experiment can be seen. Hence, a valid objection is the fact, that the high trap constant does not allow much movement for the polymers. Therefore oscillating motion are suppressed.

To investigate this superpostion further, the same measurements are repeated with a lower trap constant of $50\,k_{\mathrm{B}}T/a^2$. These results can be seen in figure 3.16. Again, no oscillations occur in the quantity $\langle \Delta y(t')\Delta y(t'+t)\rangle$.

But it is noticeable that the amplitude of this function drops to approximately half of its value for polymer length $N^m \geq 3$. This, however, is not an HI effect, but a confinement effect from the rigidity. A strong indicator for this is the fact that it does not appear for $N^m < 3$. While the trap confinement is rather low, the monomer's movement in the center is highly affected by the interaction with its neighboring monomers. With the used persistency length of $L_{\mathrm{P}} = 20\,k_{\mathrm{B}}T/a^2$ the polymer acts like a stiff rod and every monomer can move as freely as the total polymer. Since this is less than the movement of one monomer, the mean square deviation and therefore the ACF is reduced. However, no further investigations are done in this regard due to its missing connection to HI.

In the CCF one can see again the shifting in the minima, just on a different scale and correlations between the polymers are reduced. Therefore, one can state that adding monomers does not increase the correlations in the ACF. The middle monomers are disturbed and correlations between them reduced.

### 3.2.4 Synchronized Motion of Two Polymers in a Rectangular Confinement

At last, we want to compare the simulation results of two polymers confined in a rectangular channel with the experimental results from [38]. In figure 3.17 the top view of the rectangular channel with the two polymers is displayed. Therefore the parameters for the polymer are set as close as possible to the parameters from the experiment. The natural units of MPC can be converted to SI units by table 2.1. So every length scale in the simulation is given in $\mu\mathrm{m}$ and every time scale in $\mathrm{ms}$.

The used polymers in the experiment were actin filaments which have a persistence length of $L_{\mathrm{P}} = 17\,\mu\mathrm{m}$ [22]. Thus, the rigidity is set to $\kappa = 17\,k_{\mathrm{B}}T\,a$. The exact length of the polymers in the experiment was not recorded in the master thesis. They varied between 10-50 $\mu\mathrm{m}$. In order to reduce the run time without changing the result significantly, we used a length of $L = 10\,a$. The height and width of the rectangular confinement is set to $d = 4\,a$, while the experiment was done with a height of $0.5\,\mu\mathrm{m}$ and a width of $2\,\mu\mathrm{m}$. Contrary to the experimenter's claim, that the height is negligible, the polymer with a diameter of $8\,\mathrm{nm}$ has a lot of space in the $z$ direction. Since the simulation also revealed technical difficulties for smaller confinements, deviation in height and width are accepted. Nevertheless, results should still be comparable.

Before looking at the ACF for two polymers, a comparison between the ACF for one polymer from experiment and simulation is done. For the simulation, the polymer is placed

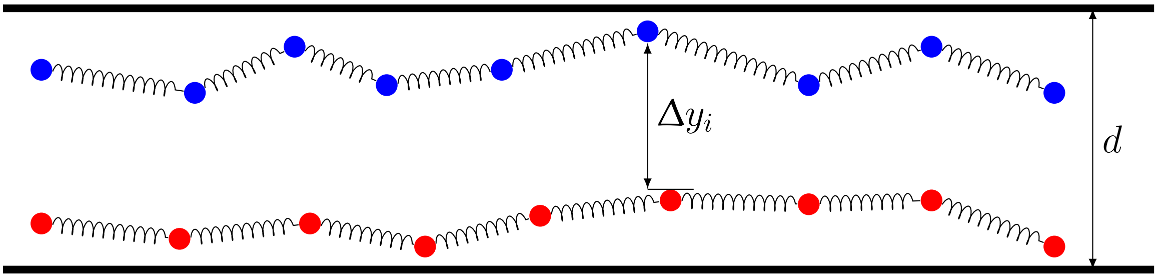

**Figure 3.17:** Top view of two polymers in a rectangular confinement with height and width $d$. autocorrelation in the projected differences $\Delta y_i$ are measured for the center monomers of the polymers.

in the center of the rectangular confinement. In both, experiment and simulation, the ACF of $\boldsymbol{r}_{1y} \equiv y$ is measured for a monomer in the center of the polymer. The primary data from the experiment and both ACF are shown in figure 3.18.

For the experimental results the correlation function from section 3.2.1 without normalization is used. Instead, the function is divided by its zeroth value which is the mean square deviation or variance of the monomer. Even though comparison with the ACF from the simulation is now prohibited, this allows us to later compare this function with the experimental results from the two-polymer experiment. For the ACF from the simulation, the data is evaluated with the priorly used correlation function. Since the data from the experiment was extracted from high speed camera images, one can assume that the time scale is in frames. The exact frame rate ($< 200\,\mathrm{Hz}$), however, is unknown. The time scale in the simulations can be considered seconds because of the transformation by table 2.1.

Significant differences between the two functions can be seen. While the experimental data shows rudimentary oscillation, the ACF in the simulation is an exponential decay. A possible reason might be the difference in the size of the primary data. From the experiment $436$ data points were auto correlated, while $3 \times 10^7$ data points over $3 \times 10^8$ time steps are used in the simulation. So we claim that not enough data points were auto correlated in the experiment in order to gain a significant statement from it.

The comparison for the two confined polymers display a difference, similar as before, in figure 3.19. Here, the ACF for the projected difference $\Delta y$ between the center monomers is evaluated. The experimental ACF shows again rudimentary oscillation, while the simulated ACF is decaying exponentially. Additionally, the ACF for the same simulation without hydrodynamics (algorithm from 2.1.5) is plotted. Figure 3.19(b) shows a small deviation between the results with and without hydrodynamics. The decay without HI is slightly slower than the one with HI. Therefore, one can say that the projected difference is longer correlated without any long ranged interactions.

Again, the cause for the differences are probably the differences in the size of the primary data. In the simulation, the amount of correlated values is again $3 \times 10^7$ values over $3 \times 10^8$ time steps. The exact frame rate from the experiment is unknown. But with the lower estimate of $20\,\mathrm{Hz}$ and the upper estimate of $200\,\mathrm{Hz}$ over $10\,\mathrm{s}$, one can assume that primary data is between $200$ to $2000$ values. Empirically, this amount of primary data is too small to gain a significant statement. Other references, such as [16, 30], also used $1 \times 10^7$ and $2^{20}$ data points for investigating correlation with HI.

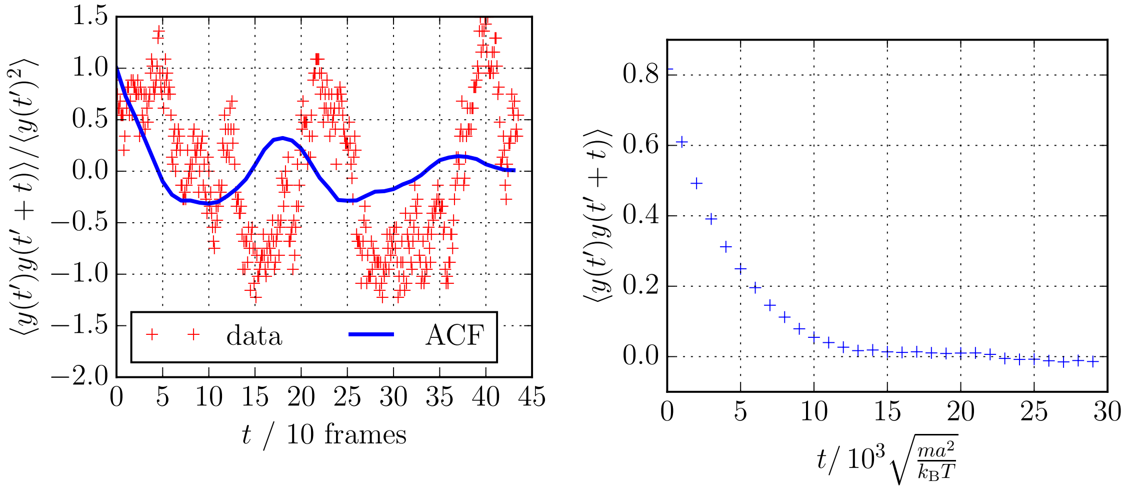

**(a)** Experimental results and its autocorrelation function for one polymer in a channel. The used autocorrelation function is not normalized, but divided by the variance. The transformation from frames to seconds is unknown [38].

**(b)** The autocorrelation function for $y$ measured in the simulation for one polymer in a channel. Since $\sqrt{ma^2/k_\mathrm{B}T} \approx 1\,\mathrm{ms}$, the time scale can be considered to be in seconds.

**Figure 3.18:** Comparison between the autocorrelation function for a the position $r_{1y} = y$ of a single polymer in a channel from experiment and simulation.

Due to a lack of access to primary experimental data, it is not possible to reproduce the experimental ACF with the ACF defined in section 3.2.1. It remains unclear, how the author of [38] defined their ACF. Dividing the ACF by its zeroth value (the axis label has been corrected) also leads to a lack of information. Hence, the mean square deviation remains unknown. From the similarity with the ACF for one polymer, one can conjecture that a non-normalized ACF was used. However, a consistent interpretation of an oscillating, decaying ACF in an equilibrated system is unknown. It cannot be interpreted as the signal from a damped harmonic oscillator, since the system is equilibrated, while a damped harmonic oscillator is a system relaxating to equilibrium.

We conjecture that a noisy signal was mistaken for oscillation. It is supported by the histogram in figure 3.20. Here the occurrences of the observed undulation frequencies are plotted for three different confinement widths. Contrary to usual normalization the author of [38] decided to normalize the histogram by the maximum. One can see that the maximum of occurrences ranges from $0\,\mathrm{Hz}$ to $2\,\mathrm{Hz}$. This is a wide spread considering the frequency from the example plot 3.19(a). There the frequency can be measured to $f \approx {}^{1}/_{4\,\mathrm{s}} = 0.25\,\mathrm{Hz}$. The range is at least over one order of magnitude. Unfortunately, a statement about the significance cannot be done, since the total number of samples was not recorded.

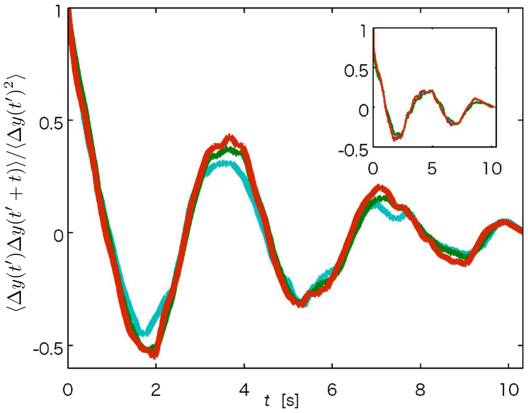

**(a)** Experimental results for the autocorrelation function of $\Delta y$ for two polymers in a channel. The different curves correspond to different monomers in the polymer. The primary data was captured at a frame rate of $20\,\mathrm{Hz}$ for the plot in the front. The inlaid plot was evaluated by a frame rate of $200\,\mathrm{Hz}$. The different curves were measured for different monomers at the same polymer. [38, corrected]

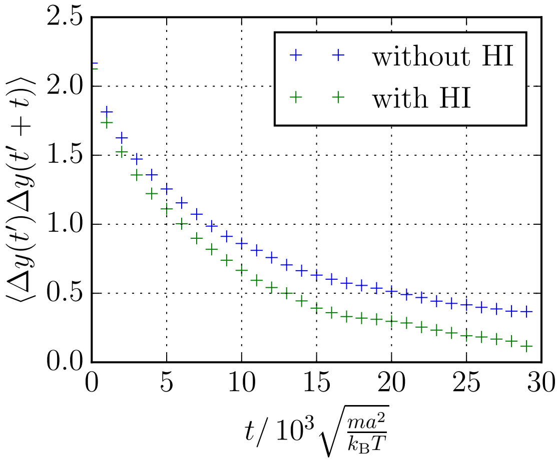

**(b)** The autocorrelation function of $\Delta y$ measured in the simulation for two polymers in a channel with and witout hydrodynamics, respectively. The time scale can again be considered to be in seconds.

**Figure 3.19:** Comparison of the autocorrelation function for the projected difference $\Delta y$ for two parallel polymers in a channel from experiment and simulation.

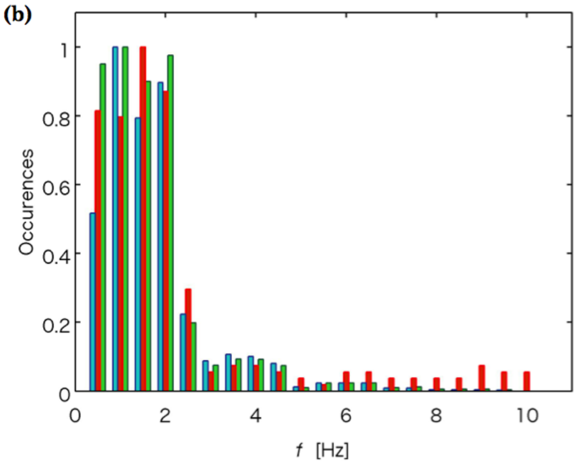

**Figure 3.20:** Histogram of undulation frequencies from the experimental autocorrelation. The values are normalized unconventionally by the maximum. The author failed to record the total amount of samples. The different colors are associated with different confinement widths: $d = 2\,\mu\mathrm{m}$ (orange), $d = 3\,\mu\mathrm{m}$ (green), $d = 3\,\mu\mathrm{m}$ (blue) [38].

# 4 Discussion

We showed that the polymer's TCF in the three dimensional simulation behaves as predicted with and without confinement. Additionally, for the confinement the numerical prefactor $c$ in the master curve was determined and compared to the one from a two dimensional Monte Carlo simulation

$$c_{\mathrm{MPC}} = 0.70 \pm 0.05 \quad \text{and} \quad c_{\mathrm{MC}} = 0.76\,. \tag{4.1}$$

It is therefore slightly smaller than in the Monte Carlo simulation. A reason for this might be the additional dimension, since this prefactor depends on the geometry of the channel. But the used boundary conditions could also have an effect on $c$.

Further, we discovered in the two trapped monomer system that the simulation correctly reflects the correlations in the ACF and CCF caused by HI. Even though, theoretical predictions were done for fixed monomers, these correlations fit to the prediction down to trap strength of $20\,k_{\mathrm{B}}T/a^2$. While simulating an infinite system with finite size, correlations due to self-interaction were seen. A single trapped monomer was able to interact with its mirror images and therefore with itself. This lead to oscillations in the ACF with a periodic time that is linear in the box length.

When extending the trapped monomers to two trapped polymers, the same correlations are visible for the center monomers. The correlation time is just shifted too shorter times and correlations appear to be weaker. This holds true for strong ($K = 1000\,k_{\mathrm{B}}T/a^2$) and weak ($K = 50\,k_{\mathrm{B}}T/a^2$) trap strength. However, oscillation as seen in [38] do not appear in such a system.

For the two polymers confined in a rectangular channel, no oscillations were seen, either. Instead, the ACF in the projected difference showed an exponential decay. The ACF did not significantly change when hydrodynamics were turned on or off. Deviations between experiment and simulation were already visible for the ACF of one polymer.

Now, there are many plausible causes for the mismatch between the experiment and simulation. The simulation might not catch the same dynamics than in the experiment because of an unknown parameter mismatch. Therefore, differences in diffusion or viscosity might lead to different correlation times. Measured phenomena in the experience might appear on a different time scale than in the simulation and a comparison between wrong time scales was done.

It is also questionable if the experimenters were able to turn of attractive forces such as van-der-Waals forces. Such forces were not considered in the simulation and might change the polymer's behavior, significantly. Additionally, videos from the experiment [1] showed that adsorption to the horizontal glass plate can occur. A polymer that is sticked to the glass plate at some parts, also shows different dynamics than a freely moving, but confined polymer.

---

[1] The video is provided in the supplementary material.

As already claimed in 3.2.4, the significance of the experimental results is highly doubtable. Not only were the number of total occurrences not recorded for the histogram in 3.20, but also the number of data evaluated for the ACF differs extremely from those in earlier experiments [4, 16, 30].

In the text book [2, chap. 6.4] an error on the ACF was estimated

$$\frac{\sigma(\langle A(t'+t)A(t')\rangle)}{\langle A^2(t')\rangle} = 2\left(\frac{t_{\text{corr}}}{t_{\text{run}}}\right)^{\frac{1}{2}} . \tag{4.2}$$

As an example, for $t_{\text{corr}}$ of the order of ten time steps, it would be necessary to conduct a run of $10^5$ steps in order to obtain a relative precision of $1\,\%$ in the ACF [2]. With the run time of up to $2000$ data points and a lower estimate for the correlation time of $100$ data points, we can estimate benevolently the error to $32\,\%$. However, higher correlation times seem to be more realistic. Therefore the error probably is much higher. This supports the argument for not-significant, experimental results.

Even though this model already correctly reflects the correlation between two monomers due to HI, a possible, fundamental improvement could be by using extended, hard spheres instead of point particles for the monomers. Then, the monomers do not couple to the fluid by taking part in the collision step anymore, since one monomer can be greater than one cell. Instead a coupling similar to the no-slip boundary conditions in 2.1.2 can be applied.

Such a mesoscopic simulation with hard spheres was used in [32]. There, colloidal particles in a microfluidic channel were simulated. While the boundary conditions reflect the solvent particles from a plane wall, their boundary conditions reflected the solvent particles from a spherical surface without slip. Addtionally, the solvent particles exchange a momentum to the hard spheres.

In this way, a more accurate model of the monomers can be achieved. For the hydrodynamic interaction, the monomers' interaction is not longer approximated by the Oseen tensor. Instead the Navier–Stokes equation is solved with boundary conditions of spherical surfaces. Also, the hydrodynamic radius can directly be affected by the radius of the spheres.

However, a disadvantage will be the quite expensive computational power. The boundary conditions have to be carried out for every solvent and every solute particle. So for further investigations, one has to weigh the odds, if a more precise model will be necessary.

# Bibliography

[1] E. Allahyarov and G. Gompper, “Mesoscopic solvent simulations: multiparticle-collision dynamics of three-dimensional flows”, en, Phys. Rev. E **66** (2002).

[2] M. P. Allen and D. J. Tildesley, *Computer simulation of liquids* (Clarendon Press ; Oxford University Press, Oxford [England] : New York, 1987).

[3] G. M. Amdahl, “Validity of the single processor approach to achieving large scale computing capabilities”, en, in (1967), p. 483.

[4] J. Bammert, L. Holzer, and W. Zimmermann, “Dynamics of two trapped brownian particles: shear-induced cross-correlations”, en, Eur. Phys. J. E **33**, 313–325 (2010).

[5] J.-P. Boon and S. Yip, *Molecular hydrodynamics* (Dover Publications, New York, 1991).

[6] H. Bruus, *Theoretical microfluidics*, Oxford master series in physics 18 (Oxford University Press, Oxford ; New York, 2008).

[7] L. Dagum and R. Menon, “OpenMP: an industry standard API for shared-memory programming”, IEEE Comput. Sci. Eng. **5**, 46–55 (1998).

[8] J. K. G. Dhont and Kernforschungsanlage Jülich, eds., *Macromolecular systems in soft and living matter: lecture notes of the 42nd IFF spring school 2011*, eng, Schriften des Forschungszentrums Jülich Reihe Schlüsseltechnologien 20 (Forschungszentrum, Zentralbibliothek, Jülich, 2011).

[9] M. Doi and S. F. Edwards, *The theory of polymer dynamics*, eng, International series of monographs on physics 73 (Clarendon Press, Oxford, 2009).

[10] E. H. Egelman, “The structure of f-actin”, eng, J. Muscle Res. Cell. Motil. **6**, 129–151 (1985).

[11] J. Elgeti and G. Gompper, “Emergence of metachronal waves in cilia arrays”, en, Proc. Natl. Acad. Sci. **110**, 4470–4475 (2013).

[12] Forschungszentrum Jülich GmbH and Z. Verlag, *Functional soft matter this spring school was organized by the institute for advanced simulation, the institute of complex systems, the jülich centre for neutron science and the peter grünberg institute of the forschungszentrum jülich on 23 february - 6 march 2015*, German (Forschungszentrum Jülich, Jülich, 2015).

[13] L. B. Gravert, *Monte-carlo-simulation semiflexibler polymere in zwei und drei raumdimensionen*, Vol. Bachelor thesis (Dortmund, 2011).

[14] J. Grotendorst and Institute for Advanced Simulation, eds., *Hierarchical methods for dynamics in complex molecular systems: IAS winter school, 5 - 9 march 2012, forschungszentrum jülich GmbH ; lecture notes*, eng, Schriften des Forschungszentrums Jülich IAS Series 10 (Forschungszentrum Jülich, Jülich, 2012).

[15] M. Hecht, J. Harting, T. Ihle, and H. J. Herrmann, “Simulation of claylike colloids”, en, Phys. Rev. E **72** (2005).

[16] S. Henderson, S. Mitchell, and P. Bartlett, “Direct measurements of colloidal friction coefficients”, en, Phys. Rev. E **64** (2001).

[17] C. Holm and K. Kremer, eds., *Advanced computer simulation approaches for soft matter sciences III*, en (Springer Berlin Heidelberg, Berlin, Heidelberg, 2009).

[18] K. C. Holmes, D. Popp, W. Gebhard, and W. Kabsch, “Atomic model of the actin filament”, Nature **347**, 44–49 (1990).

[19] C. Huang, A. Chatterji, G. Sutmann, G. Gompper, and R. Winkler, “Cell-level canonical sampling by velocity scaling for multiparticle collision dynamics simulations”, en, J. Comput. Phys. **229**, 168–177 (2010).

[20] J. D. Hunter, “Matplotlib: a 2D graphics environment”, Comput. Sci. Eng. **9**, 90–95 (2007).

[21] E. Jones, T. Oliphant, P. Peterson, et al., *SciPy: open source scientific tools for python* (2001).

[22] T. Kampmann, *Adsorption semiflexibler polymere*, Vol. Diploma thesis (Dortmund, 2012).

[23] N. Kikuchi, A. Gent, and J. M. Yeomans, “Polymer collapse in the presence of hydrodynamic interactions”, Eur. Phys. J. E, 63–66 (2002).

[24] M. Kim and T. R. Powers, “Hydrodynamic interactions between rotating helices”, en, Phys. Rev. E **69** (2004).

[25] S. Köster, H. Stark, T. Pfohl, and J. Kierfeld, “Fluctuations of single confined actin filaments”, en, Biophys Rev Lett **02**, 155–166 (2007).

[26] L. D. Landau, E. M. Lifšic, H.-G. Schöpf, G. Heber, and L. D. Landau, *Elastizitätstheorie*, ger, Unveränd. Nachdr. der 7. Aufl, Lehrbuch der theoretischen Physik von L. D. Landau; E. M. Lifschitz. In dt. Sprache hrsg. von Gerhard Heber ; Bd. 7 (Deutsch, Frankfurt am Main, 2010).

[27] L. D. Landau, E. M. Lifšic, P. Ziesche, and L. D. Landau, *Hydrodynamik*, ger, 5., überarb. Aufl., korr. Nachdr, Lehrbuch der theoretischen Physik in 10 Bänden / L. D. Landau; E. M. Lifschitz. In dt. Sprache hrsg. von Paul Ziesche ; Bd. 6 (Deutsch, Frankfurt am Main, 2007).

[28] E. Lauga, “Life around the scallop theorem”, en, Soft Matter **7**, 3060–3065 (2011).

[29] A. Malevanets and R. Kapral, “Mesoscopic model for solvent dynamics”, en, J. Chem. Phys. **110**, 8605 (1999).

[30] J.-C. Meiners and S. R. Quake, “Direct measurement of hydrodynamic cross correlations between two particles in an external potential”, en, Phys. Rev. Lett. **82**, 2211–2214 (1999).

[31] J. S. Myung, F. Taslimi, R. G. Winkler, and G. Gompper, “Self-organized structures of attractive end-functionalized semiflexible polymer suspensions”, en, Macromolecules **47**, 4118–4125 (2014).

[32] A. Nikoubashman, C. N. Likos, and G. Kahl, “Computer simulations of colloidal particles under flow in microfluidic channels”, en, Soft Matter **9**, 2603 (2013).

[33] T. E. Oliphant, “Python for scientific computing”, Comput. Sci. Eng. **9**, 10–20 (2007).

[34] E. M. Purcell, “Life at low reynolds number”, en, Am. J. Phys. **45**, 3 (1977).

[35] S. Y. Reigh, R. G. Winkler, and G. Gompper, “Synchronization and bundling of anchored bacterial flagella”, en, Soft Matter **8**, 4363 (2012).

[36] M. Ripoll, K. Mussawisade, R. Winkler, and G. Gompper, “Dynamic regimes of fluids simulated by multiparticle-collision dynamics”, en, Phys. Rev. E **72** (2005).

[37] M. Smoluchowski, Bull. Acad. Pol. Sci., 28 (1911).

[38] Z. Swank, *The physical evolution of entangled actin polymers in pseudopodia-like microconfinements*, Vol. Master thesis (Basel, 2014).

[39] M. Theers and R. G. Winkler, “Effects of thermal fluctuations and fluid compressibility on hydrodynamic synchronization of microrotors at finite oscillatory reynolds number: a multiparticle collision dynamics simulation study”, en, Soft Matter **10**, 5894–5904 (2014).

[40] M. Tuckerman, B. J. Berne, and G. J. Martyna, “Reversible multiple time scale molecular dynamics”, en, J. Chem. Phys. **97**, 1990 (1992).

# Danksagung

Zunächst gilt mein Dank Herrn Prof. Dr. Kierfeld für die Betreuung meiner Masterarbeit sowie der Begutachtung. Er hat mir stets, bei Fragen und Problemen geholfen.

Auch ganz herzlich bedanken will ich mich bei Frau Dr. Löw, die sich freundlicherweise bereiterklärt hat, diese Masterarbeit als Zweitgutachterin zu begutachten.

Natürlich geht mein Dank auch an meine Eltern und meine Schwester für die Jahrelange finanzielle und ideelle Unterstützung während meines bisherigen Schul- und Studienlaufbahn.

Mal wieder, bedanken möchte ich mich bei unserer Mammutgruppe Maik Malki, Ismo Toijala, Igor Babuschkin, Peter Lorenz und Christian-Roman Gerhorst für die gegenseitige Unterstützung im bisherigen Studium und Hilfe bei der ein oder anderen Schwierigkeit mit den Programmiersprachen C++ und Python sowie dem Textsatzsystems TeX während der Masterarbeit. Insbesondre bedanke ich mich bei Christian-Roman Gerhorst, Peter Lorenz und Ismo Toijala für das sehr genaue Korrekturlesen meiner Arbeit vor der Abgabe.

Zusätzlich geht mein Dank auch an Matthias Schmidt für ein zusätzliches Kommentieren meiner Arbeit.

Nicht unerwähnt bleiben, sollen natürlich auch meine Bürokollegen, Frederik Keim, Heiko Müller und Sebastian Sohn. Sie konnten meine Arbeit mit lebendigen und überzeugenden Diskussionen bereichern. Mit einer besonderen Freundlichkeit haben einige von ihnen mich auf meine Fehler hingewiesen. Besonders bei der Erarbeitung der IENS boundary conditions haben sie viel beigetragen.

Zuletzt geht mein Dank an den Kleinkünstler Marc-Uwe Kling, seinem Mitbewohner dem kommunistischen Känguru, der Lesebühne “Die Lesedühne” und den Autoren von “The Simpsons” für eine erfolgreiche Ablenkung und Prokrastination, während der Erstellung dieser Masterarbeit.

„Ay, caramba!!“

# 5 Appendix

## 5.1 Rotation Matrix for SRD

The matrix $\mathcal{D}$ for the stochastic rotation matrix $\mathfrak{R} = \mathcal{D}(\alpha) - \mathbb{1}$ is

$$\mathcal{D}_c(\alpha) = \begin{pmatrix} \mathcal{R}_x^2 + (1-\mathcal{R}_x^2)\mathrm{c} & \mathcal{R}_x\mathcal{R}_y(1-\mathrm{c}) - \mathcal{R}_z\mathrm{s} & \mathcal{R}_x\mathcal{R}_z(1-\mathrm{c}) + \mathcal{R}_y\mathrm{s} \\ \mathcal{R}_x\mathcal{R}_y(1-\mathrm{c}) + \mathcal{R}_z\mathrm{s} & \mathcal{R}_y^2 + (1-\mathcal{R}_y^2)\mathrm{s} & \mathcal{R}_y\mathcal{R}_z(1-\mathrm{s}) - \mathcal{R}_x\mathrm{s} \\ \mathcal{R}_x\mathcal{R}_z(1-\mathrm{c}) - \mathcal{R}_y\mathrm{s} & \mathcal{R}_y\mathcal{R}_z(1-\mathrm{c}) + \mathcal{R}_x\mathrm{s} & \mathcal{R}_z^2 + (1-\mathcal{R}_z^2)\mathrm{s} \end{pmatrix} \tag{5.1}$$

with the unit vector $\mathcal{R} = (\mathcal{R}_x, \mathcal{R}_y, \mathcal{R}_z)^\top, \mathrm{c} = \cos(\alpha), \mathrm{s} = \sin(\alpha)$. The Cartesian components of $\mathcal{R}$ are defined as

$$\mathcal{R}_x = \sqrt{1-\theta^2}\cos(\phi)\,, \quad \mathcal{R}_y = \sqrt{1-\theta^2}\sin(\phi)\,, \quad \mathcal{R}_z = \theta \tag{5.2}$$

where $\phi$ and $\theta$ are uncorrelated random numbers, which are taken from uniform distributions over $[0, 2\pi)$ and $[-1, 1)$, respectively.

## 5.2 Time-Reversal Invariance for IENS Boundary Conditions

It can be proven that the IENS boundary conditions are exactly time-reversal invariant in the first order. We first look at the velocity-Verlet algorithm where the particle penetrated the wall between the times $t$ and $t_2 = t + h_{\mathrm{MD}}$, so that the position $\boldsymbol{r}_i(t_2)$ has to be corrected to $\tilde{\boldsymbol{r}}_i(t_2)$.

$$\boldsymbol{r}_i(t_2) = \boldsymbol{r}_i(t) + h_{\mathrm{MD}}\boldsymbol{v}_i(t) + \frac{h_{\mathrm{MD}}^2}{2M}\boldsymbol{F}_i(t) \tag{5.3}$$

$$\boldsymbol{v}_i(t_2) = \boldsymbol{v}_i(t) + \frac{h_{\mathrm{MD}}}{2M}\left(\boldsymbol{F}_i(t) + \boldsymbol{F}_i(t_2)\right). \tag{5.4}$$

The initial position and velocity are therefore $\boldsymbol{r}_i(t)$ and $\boldsymbol{v}_i(t)$. The positions and velocities at time $t_2$ will then be corrected by

$$\begin{aligned} \tilde{\boldsymbol{r}}_i(t_2) &= \boldsymbol{r}_i(t + h_{\mathrm{MD}}) - 2\Delta h_{\mathrm{MD},i}\boldsymbol{v}_i(t) + \frac{\left(-2\Delta h_{\mathrm{MD},i}\right)^2}{2M}\boldsymbol{F}_i(t) && (5.5) \\ &= \boldsymbol{r}_i(t) + \boldsymbol{v}_i(t)\big(h_{\mathrm{MD}} - 2\Delta h_{\mathrm{MD},i}\big) + \frac{1}{2M}\boldsymbol{F}_i(t)\Big(h_{\mathrm{MD}}^2 + 4\Delta h_{\mathrm{MD},i}^2\Big) && (5.6) \\ \tilde{\boldsymbol{v}}_i(t_2) &= -\boldsymbol{v}_i(t) + \frac{2\Delta h_{\mathrm{MD},i} - h_{\mathrm{MD}}}{2M}\left(\boldsymbol{F}_i(t) + \boldsymbol{F}_i(t_2)\right). && (5.7) \end{aligned}$$

These are now the new position and velocity after the particle collided with the wall. For the proof we reverse the time at this point and apply the velocity-Verlet algorithm onto the position at time $t_2$ with a negative time step $-h_{\mathrm{MD}}$

$$\boldsymbol{r}_i(t_2 - h_{\mathrm{MD}}) = \tilde{\boldsymbol{r}}_i(t_2) - h_{\mathrm{MD}}\tilde{\boldsymbol{v}}_i(t_2) + \frac{h_{\mathrm{MD}}^2}{2M}\boldsymbol{F}_i(t_2) \tag{5.8}$$

$$\begin{align}
&= \boldsymbol{r}_i(t) + \boldsymbol{v}_i(t)\big(h_{\mathrm{MD}} - 2\Delta h_{\mathrm{MD},i}\big) + \frac{1}{2M}\boldsymbol{F}_i(t)\Big(h_{\mathrm{MD}}^2 + 4\Delta h_{\mathrm{MD},i}^2\Big) \tag{5.9}\\
&\quad - h_{\mathrm{MD}}\left(-\boldsymbol{v}_i(t) + \frac{2\Delta h_{\mathrm{MD},i} - h_{\mathrm{MD}}}{2M}\left(\boldsymbol{F}_i(t) + \boldsymbol{F}_i(t_2)\right)\right) + \frac{1}{2M}h_{\mathrm{MD}}^2\boldsymbol{F}_i(t_2) \tag{5.10}\\
&= \boldsymbol{r}_i(t) + \boldsymbol{v}_i(t)\big(2h_{\mathrm{MD}} - 2\Delta \mathrm{h}_{\mathrm{MD,i}}\big) \nonumber\\
&\quad + \frac{\boldsymbol{F}_i(t)}{M}\left[h_{\mathrm{MD}}^2 - \Delta h_{\mathrm{MD},i}h_{\mathrm{MD}} + 2\Delta h_{\mathrm{MD},i}^2\right] \nonumber\\
&\quad + \frac{\boldsymbol{F}_i(t_2)}{M}\left[-\Delta h_{\mathrm{MD},i}h_{\mathrm{MD}} + h_{\mathrm{MD}}^2\right]. \tag{5.11}
\end{align}$$

These positions are now corrected by equation (5.6). The penetration time is now $\Delta h'_{\mathrm{MD},i} = h_{\mathrm{MD}} - \Delta h_{\mathrm{MD},i}$, but since we reversed the time, the position has to be corrected by the time $-\Delta h'_{\mathrm{MD},i}$

$$\begin{align}
\tilde{\boldsymbol{r}}_i(t_2 - h_{\mathrm{MD}}) &= \boldsymbol{r}_i(t_2 + h_{\mathrm{MD}}) + 2\Delta h'_{\mathrm{MD},i}\tilde{\boldsymbol{v}}_i(t_2) + \frac{\left(-2\Delta h'_{\mathrm{MD},i}\right)^2}{2M}\boldsymbol{F}_i(t_2) \tag{5.12}\\
&= \boldsymbol{r}_i(t) + \boldsymbol{v}_i(t)\big(2h_{\mathrm{MD}} - 2\Delta \mathrm{h}_{\mathrm{MD,i}}\big) \nonumber\\
&\quad + \frac{\boldsymbol{F}_i(t)}{M}\left[h_{\mathrm{MD}}^2 - \Delta h_{\mathrm{MD},i}h_{\mathrm{MD}} + 2\Delta h_{\mathrm{MD},i}^2\right] + \frac{\boldsymbol{F}_i(t_2)}{M}\left[-\Delta h_{\mathrm{MD},i}h_{\mathrm{MD}} + h_{\mathrm{MD}}^2\right] \nonumber\\
&\quad + 2\Delta h'_{\mathrm{MD},i}\left(-\boldsymbol{v}_i(t) + \frac{2\Delta h_{\mathrm{MD},i} - h_{\mathrm{MD}}}{2M}\left(\boldsymbol{F}_i(t_2) + \boldsymbol{F}_i(t)\right)\right) \nonumber\\
&\quad + \frac{2\Delta h'^2_{\mathrm{MD},i}}{M}\boldsymbol{F}_i(t_2) \tag{5.13}\\
&= \boldsymbol{r}_i(t) + \boldsymbol{v}_i(t)\underbrace{\left(2h_{\mathrm{MD}} - 2\Delta h_{\mathrm{MD},i} - 2\Delta h'_{\mathrm{MD},i}\right)}_{=0} \nonumber\\
&+ \boldsymbol{F}_i(t)\Big[h_{\mathrm{MD}}^2 - \Delta h_{\mathrm{MD},i} + 2\Delta h_{\mathrm{MD},i}^2 + 2\Delta h\Delta h'_{\mathrm{MD},i}\Big] \nonumber\\
&+ \boldsymbol{F}_i(t_2)\Big[-\Delta h_{\mathrm{MD},i}h_{\mathrm{MD}} + h_{\mathrm{MD}}^2 + 2\Delta h_{\mathrm{MD},i}h'_{\mathrm{MD},i} - h_{\mathrm{MD}}h'_{\mathrm{MD},i} + 2h'^2_{\mathrm{MD},i}\Big] \tag{5.14}\\
&= \boldsymbol{r}_i(t) + 2h_{\mathrm{MD}}^2\boldsymbol{F}_i(t) + \boldsymbol{F}_i(t_2)\Big[2h_{\mathrm{MD}}^2 - 2\Delta h_{\mathrm{MD},i}h_{\mathrm{MD}} + \Delta 2h_{\mathrm{MD},i}^2\Big] \tag{5.15}\\
&= \boldsymbol{r}_i(t) + \mathcal{O}(h_{\mathrm{MD}}^2)\,. \tag{5.16}
\end{align}$$

For the corrected velocity we get

$$\begin{align}
\tilde{\boldsymbol{v}}_i(t_2 - h_{\mathrm{MD}}) &= -\tilde{\boldsymbol{v}}_i(t_2) + \frac{-2\Delta h'_{\mathrm{MD},i} + h_{\mathrm{MD}}}{2M}\left(\boldsymbol{F}_i(t_2) + \boldsymbol{F}_i(t_2 - h_{\mathrm{MD}})\right) \tag{5.17}\\
&= \boldsymbol{v}_i(t) + \left(-\frac{2\Delta h_{\mathrm{MD},i} - h_{\mathrm{MD}}}{2M} + \frac{-2\Delta h'_{\mathrm{MD},i} + h_{\mathrm{MD}}}{2M}\right)\left(\boldsymbol{F}_i(t_2) + \boldsymbol{F}_i(t)\right) \tag{5.18}\\
&= \boldsymbol{v}_i(t)\,. \tag{5.19}
\end{align}$$

The time-reversal invariance is exact in the velocity, while the error per wall hit on the position is of the order $\mathcal{O}(h_{\mathrm{MD}}^2)$.

## 5.3 The Velocity Auto Correlation Function in MPCD

A short outline for the influence of HI on the diffusion constant $D$ will be given here. Calculations from [5, chap. 2.5] and [36] were summarized.

Making use of the fundamental theorem of calculus

$$\boldsymbol{r}(t) - \boldsymbol{r}(0) = \int_0^t \mathrm{d}t' \, \boldsymbol{v}(t') \tag{5.20}$$

one can find

$$\begin{aligned}
\langle \boldsymbol{r}^2(t) \rangle &= \int_0^t \mathrm{d}t' \int_0^t \mathrm{d}t'' \, \langle \boldsymbol{v}(t')\boldsymbol{v}(t'') \rangle &(5.21)\\
&= \int_0^t \mathrm{d}t' \int_0^t \mathrm{d}t'' \, \langle \boldsymbol{v}(t'-t'')\boldsymbol{v}(0) \rangle &(5.22)\\
&= \int_0^t \mathrm{d}t' \int_{t'-t}^{t'} \mathrm{d}\tau \, \langle \boldsymbol{v}(\tau)\boldsymbol{v}(0) \rangle &(5.23)
\end{aligned}$$

for the mean square displacement for a solute in a fluid. In the second line the stationary property of correlation functions was used. Further, the integration variable was changed from $t' - t'' = \tau$. By changing the order by which the region is integrated, one can solve the integral. Instead of horizontal strips one can integrate over vertical strips and gets

$$\begin{aligned}
\langle \boldsymbol{r}^2(t) \rangle = \int_{-t}^0 \mathrm{d}\tau \, \langle \boldsymbol{v}(\tau)\boldsymbol{v}(0) \rangle \int_0^{t+\tau} \mathrm{d}t' + \int_0^t \mathrm{d}\tau \, \langle \boldsymbol{v}(\tau)\boldsymbol{v}(0) \rangle \int_\tau^t \mathrm{d}t' &\quad (5.24)\\
= 2 \int_0^t \mathrm{d}\tau \, (t-\tau) \langle \boldsymbol{v}(\tau)\boldsymbol{v}(0) \rangle &\quad (5.25)
\end{aligned}$$

From (5.25) we can see, that the mean square displacement highly depends on the VACF $\langle \boldsymbol{v}(\tau)\boldsymbol{v}(0) \rangle$. For small times the behavior of the mean square displacement is non-linear. Here the velocity correlation are not negligible, since the particle has not forgotten its initial velocity.

For long times $t$, however, the second term becomes constant, since the VACF decays with time. Then the mean square displacement is linear and can be compared to a diffusive motion in three dimensions

$$\langle \boldsymbol{r}^2(t) \rangle = 6Dt \, . \tag{5.26}$$

One gets the diffusion constant $D$

$$D = \frac{1}{3} \int_0^\infty \mathrm{d}\tau \, \langle \boldsymbol{v}(\tau)\boldsymbol{v}(0) \rangle \, . \tag{5.27}$$

Since the time in our simulation is discretized, the integral can be exchanged by a sum

$$D = \frac{1}{3} \left[ \frac{1}{2} \langle \boldsymbol{v}^2(0) \rangle h + \sum_{n=1}^{\infty} \langle \boldsymbol{v}(nh)\boldsymbol{v}(0) \rangle \right] . \tag{5.28}$$

The time is discretized in $n$ time steps with the collision time $h$.

In figure 5.1 the two regimes of the VACF are plotted. For small times (5.1(a)) it was calculated in [36]

$$C_v(nh) \equiv \frac{\langle \boldsymbol{v}(nh)\boldsymbol{v}(0) \rangle}{\langle \boldsymbol{v}^2(0) \rangle} = (1-\gamma)^n \, . \tag{5.29}$$

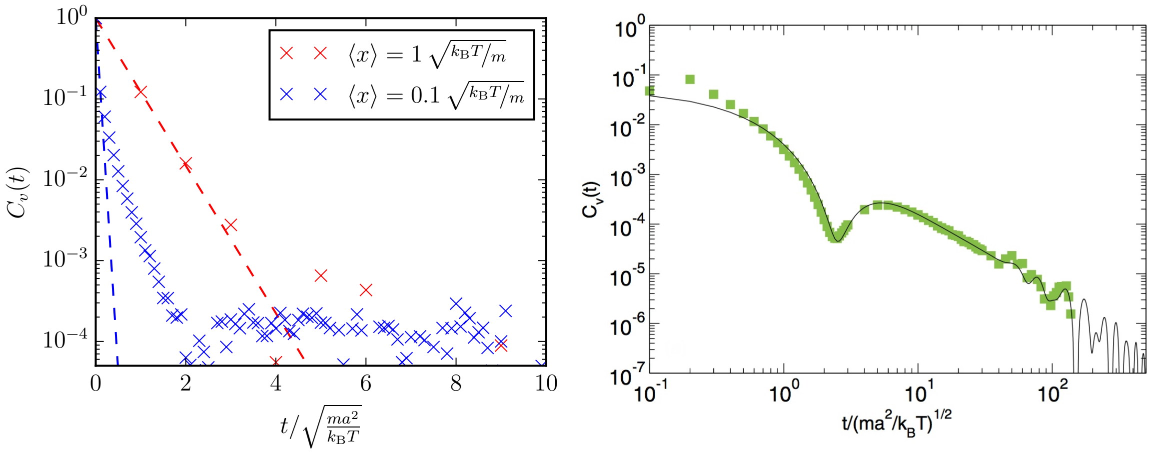

**(a)** Normalized velocity autocorrelation function for small $t$ for different mean free paths $\langle x \rangle$. The dashed lines represent the analytic solution $C_v \approx (1-\gamma)^n$ for small $t$ deduced for the SRD collision step.

**(b)** Normalized velocity autocorrelation for long time $t$. The solid line represents the typical long time tail correlation $\propto t^{-\frac{3}{2}}$ for hydrodynamic interactions. Finite-size effects can be seen for $t > 10^2 \sqrt{ma^2/k_BT}$ [12].

**Figure 5.1:** The normalized autocorrelation function $C_v \equiv \langle \boldsymbol{v}(t+t_0)\boldsymbol{v}(t_0)\rangle / \langle \boldsymbol{v}(t_0)^2\rangle$ as a function of short (a) and long (b) time. Due to finite-size effects and a lack of computational power, the long time correlation was not reproduced on the workstation.

The mean square velocity is given by the equipartition theorem $\langle \boldsymbol{v}^2(0)\rangle = 3k_BT/2m$. The decorrelation factor $\gamma$ is given by fluid properties such as the density and the rotation angle $\alpha$.

Given this information, the diffusion constant of the fluid can be calculated analytically to

$$D = \frac{k_BT}{m} h \left( \frac{1}{\gamma} - \frac{1}{2} \right) . \tag{5.30}$$

For long times (5.1(a)) the VACF shows a well-known universal behavior that corresponds to a power-law tail. It can explicitly calculated from a mode coupling theory about the Navier–Stokes equation [12]. So it shows a typical behavior that corresponds to HI, since the VACF reflects the correlations of hydrodynamic modes. In three dimensions it reads

$$C_v(t) = \frac{2}{3\rho} \frac{1}{[4\pi(D+\nu)t]^{\frac{3}{2}}} \tag{5.31}$$

where $\nu$ is the kinetic viscosity that is connected to $\eta$ by the density $\rho$ of the fluid. The power law $t^{-\frac{3}{2}}$ was reproduced in [36] for MPC.

However, this long-time tail is typical for HI. So when HI is turned off, the correlations in the velocity decay faster. Therefore, the integral as well as the diffusion constant is smaller than with HI. Thus a smaller difusion constant without HI is plausible.

# Eidesstattliche Versicherung

Ich versichere hiermit an Eides statt, dass ich die vorliegende Masterarbeit mit dem Titel “Hydrodynamic Interactions between Polymers in a Mesoscopic Simulation” selbständig und ohne unzulässige fremde Hilfe erbracht habe. Ich habe keine anderen als die angegebenen Quellen und Hilfsmittel benutzt sowie wörtliche und sinngemäße Zitate kenntlich gemacht. Die Arbeit hat in gleicher oder ähnlicher Form noch keiner Prüfungsbehörde vorgelegen.

| | |
|---|---|
| Ort, Datum | Unterschrift |

## Belehrung

Wer vorsätzlich gegen eine die Täuschung über Prüfungsleistungen betreffende Regelung einer Hochschulprüfungsordnung verstößt handelt ordnungswidrig. Die Ordnungswidrigkeit kann mit einer Geldbuße von bis zu 50 000,00 € geahndet werden. Zuständige Verwaltungsbehörde für die Verfolgung und Ahndung von Ordnungswidrigkeiten ist der Kanzler/die Kanzlerin der Technischen Universität Dortmund. Im Falle eines mehrfachen oder sonstigen schwerwiegenden Täuschungsversuches kann der Prüfling zudem exmatrikuliert werden (§ 63 Abs. 5 Hochschulgesetz).

Die Abgabe einer falschen Versicherung an Eides statt wird mit Freiheitsstrafe bis zu 3 Jahren oder mit Geldstrafe bestraft.

Die Technische Universität Dortmund wird ggf. elektronische Vergleichswerkzeuge (wie z.B. die Software “turnitin”) zur Überprüfung von Ordnungswidrigkeiten in Prüfungsverfahren nutzen.

Die oben stehende Belehrung habe ich zur Kenntnis genommen.

| | |
|---|---|
| Ort, Datum | Unterschrift |